Universidade de Aveiro Departamento de Física
2015

Américo Soares Ribeiro

Coupled Modelling of the Tagus and Sado estuaries and their Associated Mesoscale Patterns

Modelação Acoplada dos Estuários do Tejo e do Sado e Padrões de Mesoescala Associados

Universidade de Aveiro Departamento de Física
2015

Américo Soares Ribeiro

Coupled Modelling of the Tagus and Sado estuaries and their Associated Mesoscale Patterns

Modelação Acoplada dos Estuários do Tejo e do Sado e Padrões de Mesoescala Associados

Dissertação apresentada à Universidade de Aveiro para cumprimento dos requisitos necessários à obtenção do grau de Mestre em Ciências do Mar e das Zonas Costeiras, realizada sob a orientação científica do Doutor João Miguel Sequeira Silva Dias, Professor Auxiliar com Agregação do Departamento de Física da Universidade de Aveiro e co-orientação do Doutor João Daniel Alonso Antão Lencart e Silva, Bolseiro em gestão de Ciência e Tecnologia no Instituto Português do Mar e da Atmosfera (IPMA).

Este trabalho foi desenvolvido no âmbito do projeto BioChangeR (PTDC/AAC-AMB/121191/2010).

o júri

Presidente	Doutora Filomena Maria Cardoso Pedrosa Ferreira Martins Professora Associada do Departamento de Ambiente e Ordenamento da Universidade de Aveiro
Arguente	Doutora Magda Catarina Ferreira de Sousa Investigadora de Pós-Doutoramento do CESAM da Universidade de Aveiro
Orientador	Doutor João Miguel Sequeira Silva Dias Professor Auxiliar com Agregação do Departamento de Física da Universidade de Aveiro

acknowledgements

I could not have accomplished this MSc thesis without the support and friendship of a great number of people.

To Prof. João Miguel Dias, who has been my supervisor since the beginning of my academic path and has been a great contributor to my development, both as person and as a researcher. It would not have been possible to complete my MSc degree without his suggestions and comments, and above all the important advices and friendship during the course of this work.

To João Daniel Lencart e Silva for the help during the Delft3D introduction, to solve several problems, also for the valuable suggestions, especially in the numerical model setup.

No word is big enough to express my gratitude to Magda C. Sousa, for being always there as a friend and dedicated “mentor”, who has given me an enormous and valuable help during my academic path.

To the NMEC (Estuarine and Coastal Modeling Group) for providing me all the conditions to keep carrying my work, namely Nuno Vaz, Renato Mendes, Ana Picado, Carina Lopes and João Rodrigues for the help and when needed the availability for the doubts.

To HIDROMOD, specially to João Ribeiro for providing the PCOMS data.

A special thanks to my friends André Pinto, Rita Longo and Vanessa Andreso, for sharing my frustrations, as well as my victories.

To my parents, Henrique and Filomena for their unconditional support I could always count on.

To all of them I owe the achievement of my MSc degree and to them I dedicate this thesis.

palavras-chave

Dinâmica estuarina; Tejo; Sado; Delft3D; Traçador; Descarga; Pluma estuarina, Advecção.

resumo

Dada a proximidade entre os estuários do Tejo e do Sado, é reconhecido que as descargas destes estuários ocorrem na mesma região costeira. O conhecimento atual relativo à hidrodinâmica dos estuários do Tejo e do Sado resulta maioritariamente da exploração de resultados de modelos numéricos, que descrevem as propriedades físicas e padrões gerados pelas correntes de maré e descargas fluviais. Não obstante, verificou-se que a interação entre estes dois sistemas não é considerada, não havendo esforços no sentido de estudar os dois sistemas simultaneamente, bem como de descrever as relações que partilham e identificar as mútuas influências a nível dinâmico. Com este objetivo, foi implementado o modelo numérico tridimensional Delft3D-Flow, de forma a investigar a dinâmica do estuário do Tejo, do Sado e da região costeira adjacente. O modelo numérico foi calibrado e validado com a altura de maré, correntes, salinidade e temperatura da água, sendo aplicado para a investigação do efeito das descargas fluviais e do efeito do vento na interação das plumas destes estuários. O período escolhido para as simulações foi o Inverno de 2009-2010. Foram impostos dois tipos de forçamentos na fronteira aberta oceânica, um que comtempla as correntes de mesoescala e outro apenas a dinâmica costeira. Foram considerados cinco cenários para ventos moderados nos quatro principais quadrantes e para a ausência deste. Através do uso de dois traçadores distintos, foram escolhidos três cenários idealizados com descargas baixas, moderadas e altas dos rios Tejo e Sado.

Os resultados evidenciaram a presença de plumas estuarinas, filamentos e eddies causados pela interação entre os estuários e a região costeira. Os resultados obtidos revelam ainda uma intrusão da pluma estuarina do Sado no estuário do Tejo após descargas fluviais significativas durante dez dias, contudo, este padrão não foi observado na pluma estuarina do Tejo. Foi ainda observado que a água estuarina do Sado se propaga para o estuário do Tejo em apenas 36 horas com apenas a dinâmica costeira, ao passo que com as correntes de mesoescala só se observou a intrusão após 120 horas.

Sumariamente, o modelo desenvolvido para este estudo contribuiu para a caracterização e compreensão da interação entre os estuários do Tejo e Sado, e definição das condições em que esta ocorre.

keywords

Estuarine dynamics; Tagus; Sado; Delft3D; Tracer; freshwater flow; Estuarine plume; Advection.

abstract

Given the close proximity between the Tagus and Sado estuaries, it is understandable that these two hydrodynamic systems have their discharges on the same coastal region. Several studies focus on the investigation of the complex circulation at the mouth of Tagus or Sado estuaries, however, the interaction between these two systems is not taken into account and there are no studies which contemplate the interaction between the two estuaries. With this objective, the three-dimensional model Delft3D-Flow was implemented in order to investigate the complex flows in Tagus and Sado estuaries and adjacent shelf. The numerical model was calibrated and validated using sea surface height, currents, salinity and water temperature data, and then applied to research the role of river discharge and wind effects under mesoscale currents and coastal dynamics at open ocean boundaries on the plumes interaction. The chosen period was the winter of 2009-2010. To examine the response of the estuarine plumes to different wind directions, five scenarios of moderate winds were considered blowing from each of the main four compass points, and with the absence of wind. Through the use of two distinct tracers, three different idealized scenarios were chosen: low, moderate and high Tagus and Sado river discharges.

The results showed an evidence of estuarine plumes, filaments and mesoscale eddies caused by the interactions between the estuaries and the nearby coastal region. The obtained results also reveal a intrusion caused by the Sado plume in Tagus estuary after a 10-day simulation. This pattern was not observed for Tagus plume. It was also observed that the Sado estuarine water propagates to Tagus estuary in just 36 hours with coastal dynamics, when compared to the mesoscale currents forcing took around 120 hours.

In summary, the model application developed in this study contributed to the characterization and understanding of the interaction between Tagus and Sado estuary's, and in which conditions these occur.

Contents

List of Figures

List of Tables

1. Introduction

1.1. Background and motivation

For centuries, estuaries have been regions of extremely high importance to human kind. These regions are characterized by their high productivity due to river discharges, through their role as nurseries for several animal species and by providing sheltered anchorages and easy navigational access to the ocean.

Here, small and large-scale mixing processes act to produce high mixing rates and spatially inhomogeneous concentration distributions, namely the river plumes. The river plumes have higher concentration of nutrients than the ocean waters, affecting the biomass accumulation and productivity in the plume-influenced region, leading to a higher accumulation of larval fish in plume frontal zones (Govoni et al., 2000; Gray, 1996).

Despite the river plumes been receiving high interest in literature (Flather, 1976; García Berdeal, 2002; Garvine, 1984, 1982; Horner-Devine et al., 2009), insight into how the buoyancy, momentum, chemical constituents and sediment inputs provided by rivers affect the coastal ocean is vitally important for further understanding of regional productivity. The most distinguishing property of a river plume is its buoyancy. Additionally, plumes provide a mechanism for horizontal redistribution of nutrients and pollutants, because they spread and can advect material across long distances as coastal currents (Anderson et al., 2005) and are susceptible to wind and tidal forcing (Choi and Wilkin, 2007; Otero et al., 2008). These conditions determine the pattern of horizontal freshwater dispersal of estuarine plumes (McCabe et al., 2009; Walker, 1996).

All these particularities lead to the establishment of populations and industries in the vicinity of estuaries which, due to the associated anthropogenic pressure, turn the estuaries into vulnerable systems. Thus, the correct management and protection of this important natural and strategic resource require well supported decision making. Robinson (1987) stated “science is now a tripartite endeavour with simulation added to the two classic components, experiment and theory, simulation in scientific research – numerical experimentation, sensivity and process studies – is thought by many to represent the first major step forward in the basic scientific method since the seventeenth century”.

The results generated by numerical models are then highly useful but their reliability depends on the adequacy of the numerical model to the domains characteristics as well as to the physical processes not resolved by the models, to solve this, both space and time scales must be correctly parameterized. In addition, a correct knowledge of the estuarine physical processes such as

circulation and mixing is fundamental for a proper use of numerical models as a support for the better comprehension of the processes in the estuaries.

The western Iberian Peninsula coast has the presence of several estuaries, such as Tagus and Sado estuaries. Given the close relationship between the Tagus and Sado estuaries, it is understandable that these two hydrodynamic distinguished systems have their discharges on the same coastal region. The Sado estuary is located south of the Tagus estuary, which is the most important freshwater source flowing into this coastal region. Therefore, a deep understanding of the hydrodynamic circulation patterns in this region is important, especially when dealing with a complex local topography and the presence of multiple rivers.

In fact, the Tagus and Sado estuaries have different characteristics and dynamics, such as the topography, freshwater volume discharged and the shape of the estuary. For this reason, there are various studies using numerical models focusing on the investigation of the complex circulation of the Tagus or the Sado estuaries (Neves and Martins, 2004; Vaz et al., 2009). However, the interaction between these two systems was never taken into account and there were no previous studies dedicated to this topic.

Numerical models contemplating both Tagus and Sado estuaries as one system, it is a real scientific state-of-the-art challenge. This model implementation has the ability to show plume interaction patterns over shelf or even giving some insights about punctual water intrusions from the neighbor river.

1.2. Aims

The main objective of this work is to study the propagation patterns of the Tagus and Sado estuarine plumes on the coastal region, and its interaction on the circulation and hydrography on the Tagus and Sado estuaries. To achieve this objective, some specific objectives are established for this work:

- Characterize the hydrography and dynamics of the Tagus estuary and Sado estuary and adjacent coastal region;
- Develop a numerical model application to reproduce the joint propagation of the Tagus and Sado estuarine plumes;
- Evaluate different open ocean boundaries to test how mesoscale affect the transport of the estuarine plumes;
- Characterize the influence of different discharges of the Tagus and Sado rivers into the coastal zone;

- Characterize the influence of the wind direction in the propagation of the Tagus and Sado estuarine plumes;
- Investigate the necessary conditions to observe the intrusion of water from the neighbouring estuary in the Tagus estuary and Sado estuary;
- Analyse the propagation path of estuarine tracers in the coastal region.

1.3. State of the Art

In this chapter a brief literature survey on estuarine plumes, the characteristics of study region and numerical modelling of coastal regions is presented.

1.3.1. Estuarine plumes

Rivers often discharge in the coastal zone in the form of plumes and are essential for the exportation of fine sediments, nutrients and organic material from land to the coastal ocean. They can directly influence coastal budgets, ocean biogeochemistry and circulation in coastal waters (Garvine, 1984; Kourafalou, 1999).

Here the fate of the buoyant plumes are addressed to the topography and meteorological conditions in the boundaries between estuarine and Region of Freshwater Influence (ROFI) regimes. Simpson (1997) defined ROFI as a "region between the shelf sea regime and the estuary where the local input of freshwater buoyancy from the coastal source is comparable with, or exceeds, the seasonal input of buoyancy as heat which occurs all over the shelf". This author also state that a gulf type ROFI is characterized by the coastal topography, where the effect of freshwater buoyancy input together with rotational and tidal rectification aspects turns these basins into more complex systems.

Garcia et al. (2002) observed the dispersal of the Columbia river plume in response to an alongshore ambient flow and wind forcing using a three-dimensional model. The same methodology was applied by Choi and Wilkin (2007), to study the response of an idealized wind forcing and ambient flow in Hudson River plume. Through the model application, these authors provided an explanation for the observation that the plume rarely tends southward during winter season, in contrast to summer conditions when the rotational tendency of the plume and the ambient flow are in the same direction, so that wind stress must be significant to reverse the plume direction.

Sousa et al. (2014a) studied the propagation of Minho estuarine plume to the Rias Baixas, establishing the wind and river discharge conditions in which this plume affects the circulation and hydrography features of these coastal systems as well as the plume characteristics under most

probable forcing conditions, through the application of the numerical model MOHID. These authors simulated several scenarios with different river discharges and wind stress. In other study, Sousa et al. (2014b) observed that the intrusion of the Minho River plume inside these Rias can reverse their normal circulation pattern and affect the macronutrient concentrations, imposing a control on new production within the estuarine environment.

1.3.2. Tagus estuary

The Tagus Estuary has been widely studied over the last century. The first important study, as cited by Rodrigues da Silva (2003), was the one carried out by Baldaque da Silva (1893),motivated by the need to assure the easy and safe navigability within the estuary.

The first integrated study on this estuary was performed by Arantes e Oliveira (1941), who analysed the hydrodynamic and salinity distribution processes and the water quality in the Tagus Estuary. These two studies are worth mentioning due to their historical importance.

Vaz et al. (2009) analysed the dispersal of the Tagus estuarine plume, for winter case scenario, induced by wind and river flow forcing through the use of three-dimensional nested models. The authors observed near the Tagus mouth that the export of estuarine waters forms a plume which is highly influenced by the geometry of the coastline, inducing a plume trajectory very close to the coast shore. The authors also observed that northern winds events cause a displacement of the coastally trapped plume, driving a new offshore plume. Similarly, in the study performed also by Vaz et al. (2015), the authors described the main physical and biogeochemical processes in the Tagus ROFI, under strong freshwater inflow from the Tagus river, which in turn modulates the estuarine outflow to the Tagus ROFI.

Neves (2010) described some aspects of the physical oceanography of the Tagus estuary, in what concerns the propagation of the tide within the estuary, the termohaline and circulation patterns and the role of the principal forcing mechanisms of the estuarine dynamics. This analysis was accomplished researching of several monitoring programs performed along the Tagus estuary. The results indicate that the Tagus dynamics and hydrology is strongly dependent on the tidal forcing and seasonal changes of the river inflow. The author also concluded that the bottom topography and the coastline geometry play an important role on the estuarine circulation, complementing the fortnightly tide on the establishment of different residual circulation patterns.

Dias et al. (2013) applied a non-linear two-dimensional vertically integrated hydrodynamical model to simulate the tidal propagation along the estuary. The results showed that Tagus estuary tidal dynamics is extremely dependent on an estuarine resonance mode for the semi-diurnal constituents that induce important tidal characteristics. In particular, the estuarine coastline features

and topography determines the changes in tidal propagation along the estuary, which result essentially from a balance between convergence/divergence and friction and advection effects, in addition to the resonance effects.

These, and several other projects have been carried out on the Tagus Estuary, using in situ measurements, physical and numerical modelling or remote detection, which resulted on publications about pollution (Andreae et al., 1983; Duarte et al., 2014), suspended sediments (Vale and Sundby 1987; Jouanneau et al. 1998; Silva et al. 2004), circulation and tidal propagation (Fortunato et al. 1997; Fortunato et al. 1999), morphodynamics (Freire and Andrade 2008), chlorophyll (Sousa-Dias and Melo 2008; Vaz et al. 2015), estuary's plume (Valente and da Silva 2009; Vaz et al. 2009), flooding (Salgueiro et al., 2013; Tavares et al., 2015), hydrodynamics (Dias et al., 2013a) and sea level rise hazards (Valentim et al., 2013). Despite of the several studies found in literature, were not found any study devoted to the hydrodynamic features and the interaction of the Tagus estuary water in Sado estuary.

1.3.3. Sado estuary

Some studies have been made for Sado estuary to evaluate its dynamics and to study the environmental impacts.

Martins et al (2001) applied a three-dimensional model, to study the Sado estuary hydrodynamics. The results showed the influence of the main channel's strong curvature on the generation of secondary flows inside the estuary. The steep bathymetry of the outer platform gives rise to a recirculation flow in the vertical plane that lasts for most of the tidal cycle. These authors also the numerical model to study the environmental impact associated to dredging works in Setubal Harbour, and the use of sedimentary transport coupled to the hydrodynamical model.

INAG/MARETEC/IST (2002) conducted a study in the Sado estuary in order to evaluate the water quality and concluded that modelling proved to be a useful tool to overcome the difficulties associated with the lack of information and to its uneven distribution in space and time. Model results were also very useful for assessing the representativeness of data for explaining the ecological functioning of the estuaries and the spatial meaning of the average values defined for the Sado estuary.

Neves and Martins (2004) applied a three-dimensional baroclinic hydrodynamic model coupled to two transport models, one with langrangian formulation and the other with eulerian, to study the impact produced by the raise of nutrients on the primary production, assuming that the estuary has some sensivity to the raise of nutrients introduced by the Sado River producing eutrophication.

These and several other studies have been carried out on the Sado Estuary, using in situ measurements, physical and numerical modelling, which resulted on publications about circulation and tidal propagation (Sobral, 1995; Wollast, 1978), morphodynamics (Monteiro et al., 2004; Neves, 1982) and management (Caeiro et al., 2001). Despite of the several studies found in literature cited above, were not found any study devoted to the hydrodynamic features and the interaction of the Sado estuary water in Tagus estuary.

1.3.4. Numerical modelling

In this work the numerical model DELFT3D-Flow was used. Delft3D-Flow is a multi-dimensional (2D or 3D), finite differences hydrodynamic and transport model which calculates non-steady flows and transport phenomena that result from tidal and meteorological forcing on a rectangular or a curvilinear, boundary fitted grid. In 3D simulations, the vertical grid is defined following the Sigma or Cartesian coordinate approach.

The Navier-Stokes shallow water equations are solved with hydrostatic and Boussinesq approximations (Deltares, 2011a). Delft3D-Flow uses a horizontal Arakawa-C grid with control volumes and for the most applications an Alternating Direction Implicit (ADI) integration method (Deltares, 2011a; Lencart et al., 2013).

DELFT3D has previously been applied to study several estuarine systems worldwide, e.g. the Rhine ROFI (De Boer et al., 2000), Tomales Bay in California (Harcourt-Baldwin and Diedericks 2006),the Ria de Muros in North-West Spain (Carballo et al., 2009), Maputo Bay (Lencart e Silva et al., 2010; Markull et al., 2014), Meilang Bay of Taihy lake (Li et al., 2014) and in Tieshangang Bay in China (Li et al., 2015), Santa Marinella in Latium – Italy (Bonamano et al., 2015) and in Arabian Gulf (Elhakeem et al., 2015).

All this extensive number of studies in several coastal environments with different resolutions indicates that the numerical model DELFT3D-Flow has capabilities to simulate the hydrodynamics of coastal systems such as Tagus and Sado estuaries and the nearby coastal region.

1.4. Work structure

Concerning its structure, this dissertation is arranged in eight chapters. Chapter 1 presents a brief introduction which includes the motivation and the literature review. In Chapter 2, the characterization of the study area is presented, including the hydrography of the Tagus, Sorraia and Sado Rivers and Vale Michões and Marateca tributaries. In Chapter 3, the observational data used in this work is presented. Chapter 4 is devoted to the numerical model DELFT3D-Flow, and Chapter 5 to its implementation on this work. Chapter 6 presents the model application with the

description of the scenarios. Finally, Chapter 7 presents an overview of the results, followed by Chapter 8 with a summary of the conclusions and some suggestions of future work.

2. Study area: characterization of the Tagus estuary, Sado estuary and nearby coastal zone

2.1. Introduction

The topography associated with atmospheric processes, tides and river plumes are important factors to the ocean circulation. The present chapter is focused on the mesoscale physical processes identified in the Western Iberia System.

In the case of the North Eastern Atlantic system, the Canary and Iberian regions form two distinct subsystems (Barton et al., 1998). The separation is not simply geographical, but is a consequence of the distinctive characteristic of this Northeastern region: the discontinuity imposed by the strait of Gibraltar, allowing the exchange between two different water masses with a profound impact not only in the slope dynamics but also in the regional circulation (Relvas et al., 2007).

The Iberian Upwelling System (IUS) is located in western Iberia System, corresponding to the northern limit of the Eastern North Atlantic Upwelling System, prolonged to the south by the Canary Upwelling System (Barton et al., 1998). Coastal upwelling is a phenomenon that occurs at the western coasts of continents due to the presence of the mid-latitude high-pressure systems over the ocean that generate equatorward winds along the eastern boundary of the ocean basin. In the northern Hemisphere, southward winds along any continental western coast can induce, through the Coriolis effect, an offshore advection of water from the upper layers (Ramos et al., 2013). This flow in turn gives origin to an equatorward current due to the tilt of the sea level and consequent coastal divergence, giving rise to the upwelling of colder and nutrient-rich waters from deeper layers (Wooster et al. 1976). During periods without favourable winds for upwelling, the prevailing circulation at the western Iberian Peninsula coast is a northward current in the upper layers (Frouin et al., 1990). The upwelling events highly depend not only on large-scale atmospheric circulation, but also on the coastal ocean mesoscale variability (Relvas et al., 2009, 2007).

The region has various submarine canyons (Nazaré, Cascais and Setúbal-Lisbon), which cut the Western Iberia margin in an east-west direction from the continental shelf at water depths shallower than 50 m, down to the Tagus and Iberian abyssal plains at water depths exceeding 5000 m (Lastras et al., 2009).

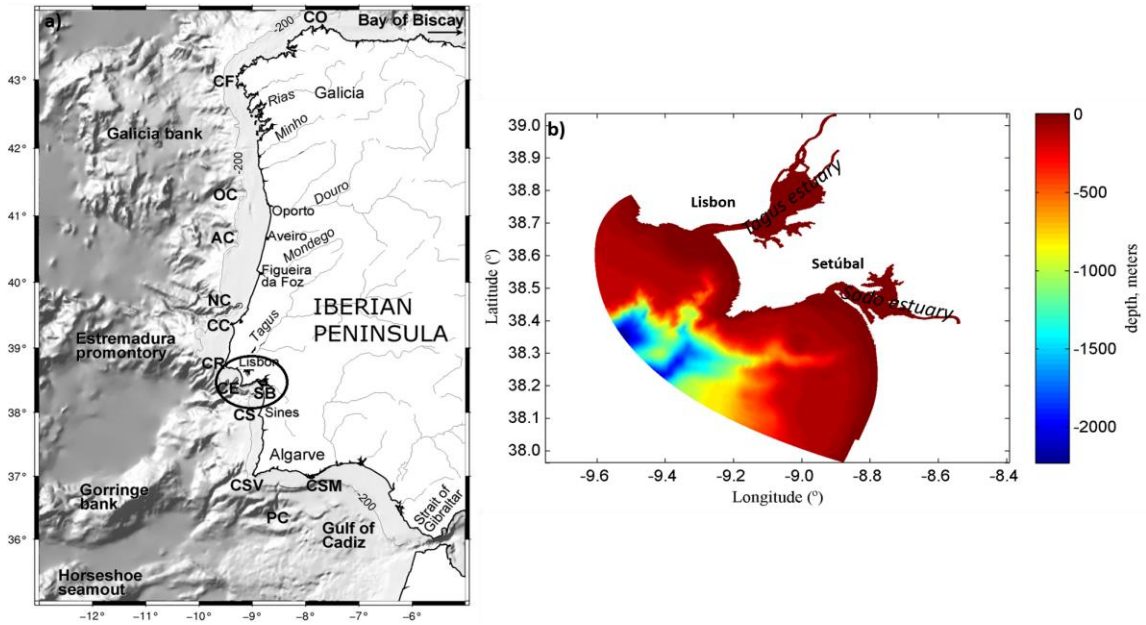

Figure 2.1: Study area: a) Geography of the Western Iberian System, showing the main features referred in the text. The 200 m bathymetric contour is shown, delimiting the continental shelf. From north to South: CO - Cape Ortegal; CF – Cape Finisterre; OC – Oporto Canyon; AC – Aveiro Canyon; CC – Cape Carvoeiro; CR – Cape Roca; CE – Cape Espichel; SB – Setubal Bay; CS – Cape Sines; CSV – Cape São Vicente; PC – Portimão Canyon; CSM – Cape Santa Maria. Adapted from Relvas et al. (2007); b) Bathymetries of Tagus and Sado estuaries and nearby coastal region.

The continental shelf and the coastal region morphology can influence the local ocean dynamics, in particular the patterns that are registered in region (Fiúza et al., 1982) under analysis in this work. The study site is located on the North Eastern Atlantic System as shown in 2.1a.

2.2. Tagus estuary

The Tagus estuary is one of the largest estuaries of the west coast of Europe and the largest of the Iberian Peninsula, having an East-West direction (Figure 2.1a), with a total area of 320 km^2 (Valente and da Silva 2009) and with a mean volume of 1.8 km^3 (Freire and Andrade 1999). Its mouth opens to a large bay in the adjacent coastal ocean, between Cape of Roca and Cape Espichel.

A deep, narrow inlet channel and a shallow inner bay compose the estuary. The inlet channel is 15 km long, 2 km wide and reaches depths of 40 m in some places (Figure 2.2), constituting the deepest part of the estuary (Fortunato et al, 1997). The inner bay is about 25 km long and 15 km wide, being the shallowest part of the estuary and has complex bottom topography with narrow channels, tidal flat areas and small islands on the inner most part of the estuary. Tidal flats corresponds to approximately 40% of the estuary's total area, and are known to have an important role in Tagus estuary's hydrodynamics by modifying the characteristics of the tidal wave (Fortunato et al. 1999; Fortunato and Oliveira 2005). The estuary is also characterized by the

existence of sand beaches, both in the inlet channel (northern margin) and in the inner bay (southern margin) (Freire and Andrade 2008).

The combined effects of low average depth, strong tidal currents, and high input river water make the Tagus a globally well-mixed estuary, with stratification being rare only in specific situations such as neap tides or after heavy rains. The Tagus estuary is meso-tidal and its circulation is mainly tidally driven. The amplitude of the tide is the controlling variable of the flow and is responsible largely for the turbidity of the Tagus, which in shallow areas of upstream part of the estuary is enhanced by small high frequency wind waves.

The tides are semi-diurnal, and the M_2 harmonic constituent is dominant with amplitudes of 1 m (Fortunato et al., 1999), with tidal ranges varying from 0.75 m in neap tides in Cascais to 4.3 m in spring tides in upper estuary (Fortunato et al., 1997; Portela and Neves, 1994). The amplitudes of astronomic constituents grow rapidly in the lower estuary and more steady in the upper estuary and then decrease up to Vila Franca de Xira (Fortunato et al., 1999). The tidal amplitude is larger than offshore as a result of a small resonance effect (Oliveira, 1992). The surface velocities present typical values around 1 m s^{-1} and the salinity above 20 m depth is about 34 psu. At the bottom, present salinity values of about 36 psu (typical oceanic values), except during high river runoff events, when lower salinity (around 34-35 psu) can be found (Vaz et al., 2009).

The influence of the river discharge seasonal variability is evidenced by several estimates for the water residence time within the Tagus estuary (Neves, 2010). As an example, Martins et al. (1983) reported a residence time between 6 and 65 days, respectively, for a river discharge between 2200 and 100 $m^3 s^{-1}$, and 23 days for a mean river discharge of 350 $m^3 s^{-1}$.

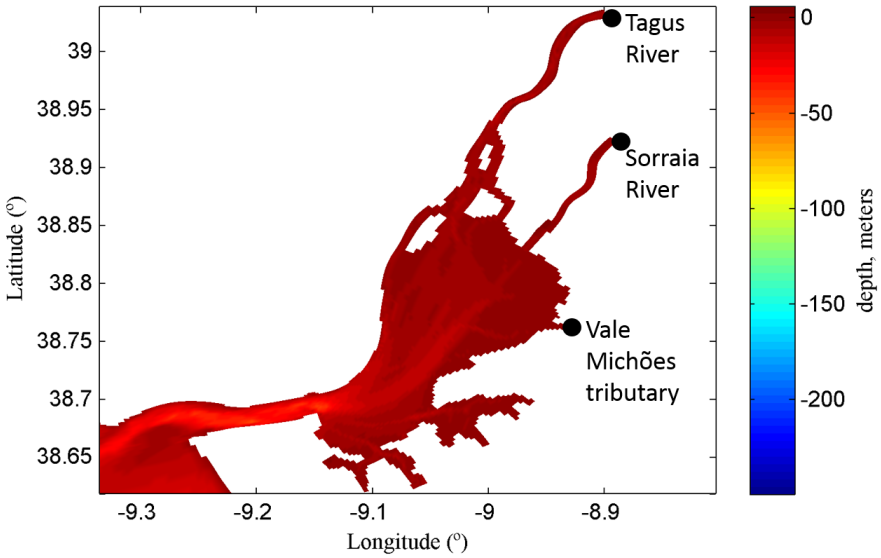

Figure 2.2: Location and bathymetry of Tagus estuary and the three freshwater inflows: Tagus river, Sorraia river and Vale Michões tributary.

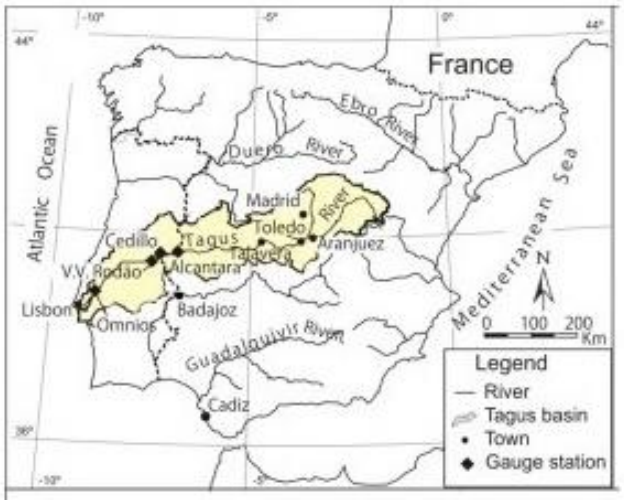

Figure 2.3: Tagus River basin location. Adapted from Salgueiro et al. (2013).

In summary, the hydrography of the estuary is modulated by the tidal propagation and fluvial discharge from the major rivers, Tagus and Sorraia and Vale Michões tributaries.

2.2.1. Tributaries

The Tagus River is the main source of freshwater of the estuary. The Tagus River is about 1038 km long, where 230 km are in Portugal, having a northeast-west direction as shown in Figure 2.1a. The river has a total catchment area of 80630 km^2 (Figure 2.3) (Vis et al., 2010).

The discharge usually shows a pronounced dry/wet season signal and a large inter-annual variation (Valente and da Silva 2009). According to Macedo (2006), the Tagus River discharge regime has been modulated since the fifties, due to the building of the most important dams of the Tagus hydrographic basin. This author presented a study on the Tagus river discharge during the period between 1974 and 2001 at Almourol – about 130 km upstream of the estuary's mouth - which showed a mean annual river discharge of 331 $m^3 s^{-1}$ and identified the year 1992 as a dry year and 1979 as a wet year.

The river has an annual average discharge of 350 $m^3 s^{-1}$, but varies greatly from summer to winter between approximately 30 $m^3 s^{-1}$ in a dry summer and 2000 $m^3 s^{-1}$ in a wet winter (Neves, 2010), instantaneous records can reach flows of about 15000 $m^3 s^{-1}$ (Vaz et al., 2009).

The river runoff can be calculated through the rainfall, this methodology is useful when the river discharge data is not available. Thus, a brief characterization of the rainfall is also presented. The mean annual rainfall in the Spanish Tagus basin for the 1949-2000 period was estimated at 655 mm (Egido et al., 2007), with a surface runoff of 11235 mm^3. A mean rainfall for the total Tagus basin for the period between 1940/1941 and 1992/1993 can be found in Appendix A (Serra, 2008).

The other two sources of freshwater of the Tagus estuary are the Sorraia River and the Vale Michões tributary.

The Sorraia River drainage system, an area measuring 7556 km^2, is the largest basin inside the Tagus River basin. The River forms at the confluence of Sor and Raia tributaries in Couço, flowing in a west direction towards the Tagus estuary. The Sorraia River has a length of 60 km from its source at Couço and a total length of 155 km from its longest source in Alentejo. The mean flow is about 39.5 $m^3 s^{-1}$ (http://www.maretec.mohid.com/portugueseestuaries).

The Vale Michões drainage system, an area measuring about 502 km^2 is located in Tagus River basin, flowing in a northwesterly direction from its source in Pegões until its confluence with Frio River, and flows directly in the Tagus estuary. The tributary has a total length of 36 km and it is characterized for the presence of four dams, used for irrigation and flood control. The flow of Vale Michões tributary is highly dependent of the rainfall.

2.3. Sado estuary

The Sado estuary is located 40 km south of Lisbon, Portugal, as shown in Figure 2.1b, with a South-West direction alignment in the Atlantic Ocean coast, with a total area of approximately 100 km^2. It is about 20 km long and 4 km wide. The maximum depth is higher than 50 m and it has an average depth of 8 m (Figure 2.4).

Several studies (Neves, 1982; Sobral, 1995; Wollast, 1979, 1978) highlighted the main processes controlling the circulation in the estuary and gave a first idea of its environment state.

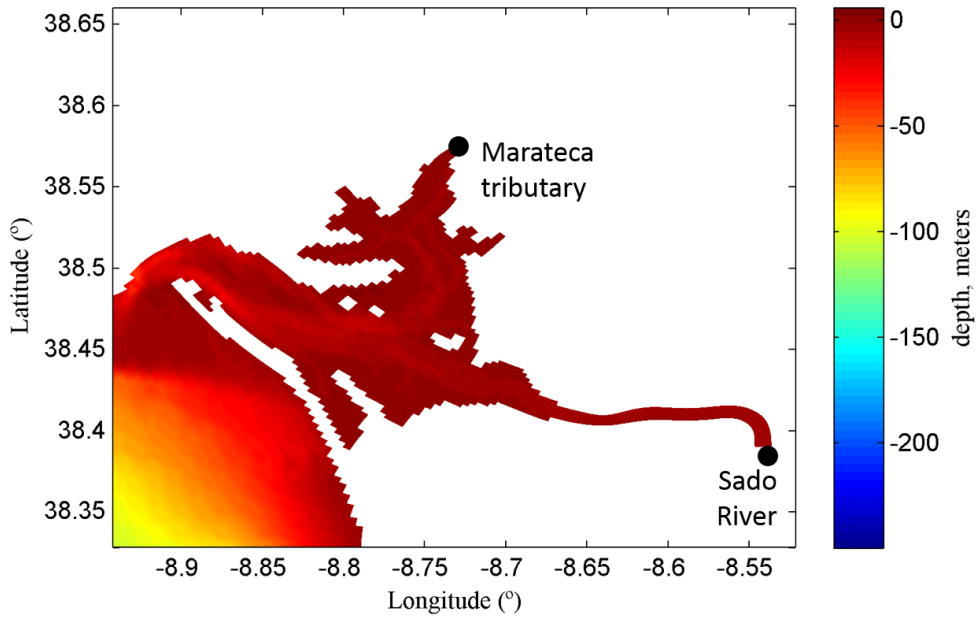

Figure 2.4: Location and bathymetry of Sado estuary and the two freshwater flows: Sado River and Marateca tributary.

The flow is mainly tidally driven and very strong residual eddies exist inside the estuary associated with the curvature of the main channels. The lower estuary is occupied by two major eddies, while in the upper estuary the residual flow is more complex. This circulation supports the subdivision of the estuary in its upper and lower parts as suggested by Wollast (1979) based on temperature and salinity distributions.

The estuary has intertidal sandbanks that individualize a northern and a southern channel. The lower estuary behaves as a coastal lagoon with small freshwater influence, while the upper estuary has a freshwater dependent behavior (Martins et al., 2001).

The upper estuary has two main channels: the Alcácer channel on southeast and the Marateca channel on the north side, with 80% and 10% of total freshwater input to the estuary respectively, being the most important freshwater entrances to the estuary.

The tide is semidiurnal, with an amplitude of about 1.6 m in spring tides, and 0.6 m in neap tides. The most important harmonic constituents are M_2 and S_2. At the mouth, their amplitudes are 0.98 m and 0.35 m respectively, both being amplified inside the estuary. The low average depth, strong tidal currents and low freshwater discharge make the Sado a well-mixed estuary, which is stratified only rarely in specified situations such as high river discharges (Barton et al., 1998).

In summary, the tidal propagation and fluvial discharge from the Sado River and the Marateca Tributary modulate the hydrography of the estuary.

2.3.1. Tributaries

The Sado River drainage system, an area measuring 8341 km^2, is bordered to the north by the Tagus River basin and by the Guadiana and the Mira River basins to the south and east respectively. The Sado River basin excluding the estuary has a total catchment of 7692 km^2 with a mean altitude of 127 m (Figure 2.5a). The Sado River is approximately 180 km, initially flowing in a northwestward direction from its source in the Serra da Vigia (altitude of 230 m), then northward along the western coast of Portugal until its confluence with the Odivelas River, where it changes its course and flows in a more westward direction towards the Atlantic Ocean (Burke et al., 2011).

Following the same methodology for the calculation of the river runoff, through the rainfall, a brief characterization of the rainfall is also presented: the mean annual rainfall in the Sado River basin for the period between 1941/42 and 1990/91 was estimated is 621 mm, from which only 175 mm is surface runoff (with mean annual flow volume of 1350 hm^3).

The highest instantaneous peak flow was 2008 $m^3 s^{-1}$ in December of 1949 [Appendix B]. The flow regime is very irregular being characterized by several months with very low flows or even without any flow (0.0 $m^3 s^{-1}$ in dry years) (Figure 2.5b).

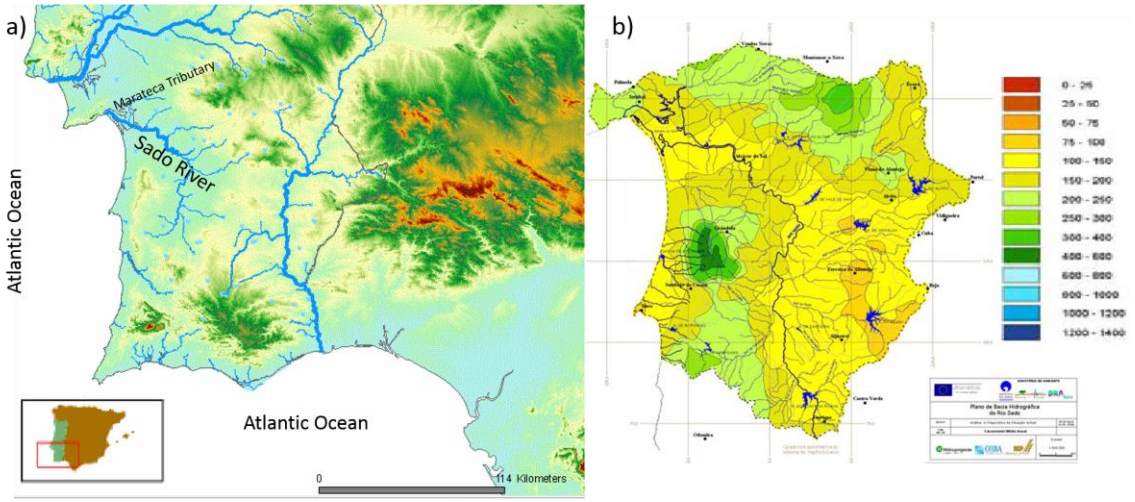

Figure 2.5: Sado River: a) Basin location; b) Mean annual flow (mm). Adapted from http://www.peer.eu/about_peer/euraqua_collaboration/network_of_hydrological_observatories/.

In summary, the Sado river flow displays a strong seasonal variability. In summer, monthly average values are lower than 1 $m^3 s^{-1}$, while in winter the average values are about 60 $m^3 s^{-1}$.

The other important freshwater source is the Marateca Tributary, located in Sado River basin (Figure 2.5a), flows directly into Sado estuary, having a total catchment of 134.07 km^2 and with a length of 17.79 km. The flow is highly dependent of the rainfall, with observations from 2660 (1980/81) to 0.002 $m^3 s^{-1}$ (1981/82) [Appendix B]

2.4. Circulation patterns

The preferential north-south orientation of the continents that bound the Atlantic Ocean lead to meridional eastern and (intensified) western boundary currents which, together with the wind-induced zonal currents – westward flow under the trade winds, and eastward flow under the mid-latitude westerly winds, centred about a large sub-tropical atmospheric high-pressure cell – form the closed oceanic gyres. The ocean circulation system of the Iberian Basin is the result of different mechanisms of forcing and interactions with the open ocean circulation. An overview of some of these mechanisms, their importance and their consequences for the ocean circulation will be enounced.

The prevailing weather conditions in the Western Iberia Peninsula are conditioned by permanent factors, such as latitude, topography, influence of the Atlantic Ocean and the continental influence. The shoreline is also an important factor (Instituto de Meteorologia, 2004).

The western Iberia System is located in the northern limit of the Eastern North Atlantic Upwelling system (Peliz et al., 2002). The Iberian Peninsula is located in the Northern Hemisphere

Climatic Subtropical High-pressure Belt, in this particular case in the Azores Anticyclone (Peixoto and Oort 1992). The variability in the positioning of the Azores Anticyclone is closely related to the climatic variability of the West Iberia Peninsula.

The monthly regime of the winds is strongly dependent on the evolution of the atmospheric circulation on regional scales, being related with the latitudinal migration of the subtropical front and with the dynamics of the Azores Anticyclone cell (Fiúza et al., 1982). From March to August, the anticyclone centre moves along the 38°W meridian from 27°N to 33°N, respectively. From November to February it moves eastwards from 38°W and reaches 27°W in January, as a consequence of the relative increase of the winter high pressures located over Europe and Africa (Fiúza et al., 1982).

According to Instituto de Meteorologia (2004), the annual average values of pressure are between 1016 and 1020 hPa. The higher values (1030 hPa) and the lower values of pressure (980 hPa) occur in winter, leading to a higher pressure gradient, caused by the Azores Anticyclone development.

The near-surface circulation in the west coast of the Iberian Peninsula is primarily driven by the wind (Relvas et al., 2007), that repeats a seasonal cycle induced by the differences of atmospheric pressure already referenced in section 2.4.1. The winds that blow near the ocean surface change the vertical and horizontal density distribution (Vieira et al., 2000). This current system in the west coast of Iberia Peninsula is the Portugal Current system (PC), and reveals a strong seasonality and variability of mesoscale patterns.

The PC extends from about 36°N to 46°N and from the Iberian shores to about 24°W (Martins, 2002; Pérez et al., 2001). The PC itself is poorly defined spatially because of the complicated interactions between coastal and offshore currents, bottom topography, and water masses.

The system is comprised of the following main currents:

- The PC, which is a broad, slow, generally southward-flowing current that extends from about 10°W to about 24°W longitude;
- The Portugal Coastal Counter-Current (PCCC), a southward flowing surface current along the coast during winter season (Frouin et al., 1990; Peliz et al., 2005). This current transports to north warm and saltier water, from tropical regions, mainly over the narrow continental shelf to about 10-11°W longitude and flow from about 41-44°N
- The Portugal Coastal Current (PCC), a generally poleward current that dominates over the PCCC during the Summer and like the PCCC extends to about 10-11°W from

shore, also is present mainly from 41-44°N, where flow is 13.5 ± 5.7 cms^{-1} (Martins, 2002; Pérez et al., 2001).

In Figure 2.6 are listed the main water masses and currents in the eastern North Atlantic region. The principal masses are Eastern North Atlantic Central Water of sub-polar ($ENACW_P$) and sub-tropical ($ENACW_T$) origins, and South Atlantic Central Water (SACW). The main large-scale surface currents are the North Atlantic Current (NAC), the Azores Current (AC), the Canary Current (CaC) and Portugal Current (PoC). Also shown are the North Atlantic Drift Current (NADC), the North Equatorial Current (NEC) and the North Equatorial Counter-Current (NECC).

The PC is supplied mainly by the intergyre zone in the North Atlantic, a region of weak circulation bounded to the north by the North Atlantic Current and to the south by the Azores Current (Pérez et al., 2001).

The PC System also suffers influence of seasonal winds, freshwater runoff from the Iberian

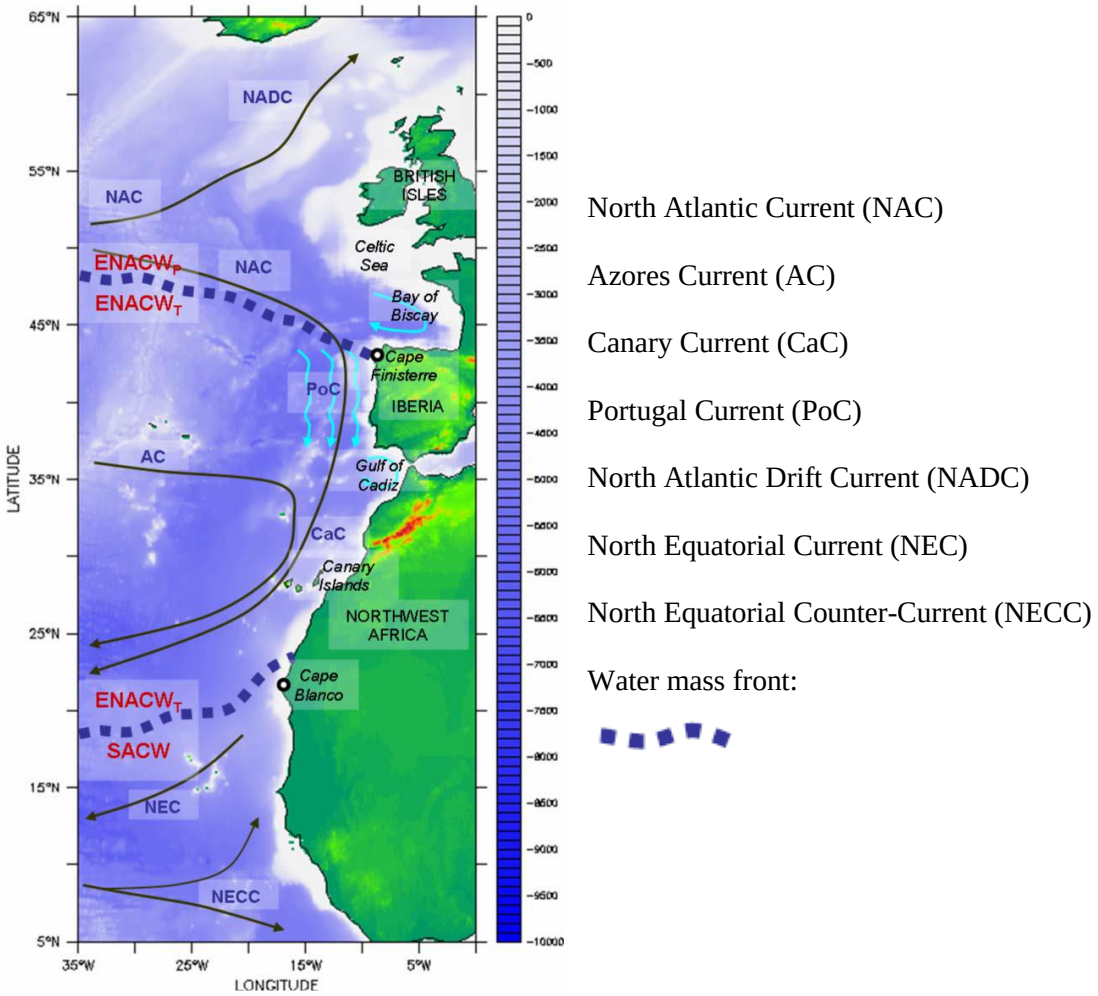

Figure 2.6: The eastern North Atlantic region. Principal currents in the eastern North Atlantic (Mason et al., 2010).

Peninsula and the bottom topography (Ambar and Fiuza 1994; Pérez et al. 2001; Huthnance et al. 2002; Martins 2002). Meddies are also present, particularly in the region of the Tagus Abyssal Plain (about 11-13°W; 37-39°N) and along the shelf break, which are thought to be controlled mainly by the topography of the seafloor (Cherubin et al. 2000; Bower 2002; Coelho 2002; Huthnance et al. 2002).

According to Huthnance et al. (2002), the average flow of the top water column fluctuates according to season and varies more with increasing proximity to the shorecoast: northwards in autumn and winter, west and southwards in spring and summer (Martins, 2002; Pérez et al., 2001).

There are two major Rivers in the study area of west coast of Iberian Peninsula - Tagus and Sado. The river runoff is mainly dependent on rainfall (see section 2.2.1 and 2.3.1) and, therefore, is higher during winter. During this season, the slope and other shelf are under the influence of the Iberian Poleward Current (IPC) (Peliz et al., 2005). The IPC is a narrow (25-40 km) slope-trapped tongue – like structure that flows northerly along a distance exceeding 1500 km off the coasts of the Iberian Peninsula (DeCastro et al., 2011).

2.5. Summary of the characterization of the study area

In this chapter was presented a characterization of the topography, hydrography and dynamics of the Iberia Peninsula, with special attention to the Tagus and Sado estuaries and the nearby coastal region. This characterization allowed to identify and understand the role played by the major factors that establish the dynamics in this study area. A characterization of the hydrology of the rivers in terms of runoff was performed. The mean rainfall of the basins was also performed.

Thus, these factors will be taken into account in the next steps of this work, which aim the numerical model implementation.

3. Data presentation

The fate of a model simulation is largely determined by the inputs. These inputs reflect the accuracy on how to model certain physical processes. This section summarizes bathymetry, tide, wind and river discharge data used in the model.

3.1. Bathymetry

The bathymetry data used in the model was obtained from several sources. The coastal region bathymetry was constructed based on the General Bathymetric Chart of the Oceans (GEBCO). This bathymetric samples were given in format .xyz, the same format as Delft3D requires for bathymetry sample inputs, whereas the Tagus and Sado estuaries samples were obtained in Portuguese Hydrographic Institute (http://www.hidrografico.pt/) with shapefile format. The bathymetry of Tagus and Sado are a compilation of data surveys collected between 1964 and 2009, with spatial resolution of 100 m. Thus, it was necessary to use the software ArcGIS in order to convert the data to the format of .xyz.

3.2. Tidal forcing and initial conditions

Two different methods of tidal forcing are applied in the model implementation: one with the Portuguese Coast Operational Modelling System (PCOMS) (http://www.maretec.org/) and the other with TOPEX/POSEIDON data (MacMillan et al., 2004).

Transport conditions and tide propagation are calculated based on inputs from the Portuguese Coast Operational Modelling System (PCOMS) (http://www.maretec.org/). The tide propagation of PCOMS is given by FES2004 (Finite Element Solution). Two sets of data were collected, the year 2009-2010 and the year 2012. The system provides 3 days forecast of hourly ocean currents, sea surface height, water temperature and salinity. The year 2009-2010 (March 6 of 2009 to March 3 of 2010) comprise 50 vertical layers. The year 2012 (July 25 to December 31) comprise 47 vertical layers. The PCOMS domain has 0.06° (~6 km) of horizontal resolution.

The tide propagation for the second method are based in a global ocean tide model (NAO.99b model) representing the major 16 constituents with a spatial resolution of 0.25°, and have been estimated by assimilating about 5 years of TOPEX/POSEIDON altimeter data.

The propagation of the tide was interpolated across the open boundary using Matlab scripts, for a posterior implementation described in section 4.3.1.

3.3. Hydrographic

3.3.1. Water level

The data set available for this study are from three field surveys in Tagus estuary, one carried out in 1972, the second in 1981 and the third in 1986. The Sado estuary data are from six tidal stations placed along the estuary (Figure 3.1). Sea surface measurements presented in Table 3.1 were performed hourly during the period stated in the Time-series column, where Tagus data is given in water level value and Sado data in harmonics. This data set aims the calibration of the model.

In Figure 3.1 is also presented the location of stations referred in Table 3.1. The harmonic constituents used for Sado tide reconstruction were the M_2, S_2, N_2, K_2, K_1, O_1, P_1, M_4, MS_4, L_2, $2N_2$, NU_2, MU_2, T_2, R_2, Q_1, $2Q_1$, RHO_1, M_3, S_4 and $2SM_2$.

3.3.1. Salinity and water temperature

Water temperature and salinity offshore is described in several studies (Quintino et al., 2006; Santos et al., 2002; Silva et al., 2004) using a compilation of the available data surveys of 2009, on

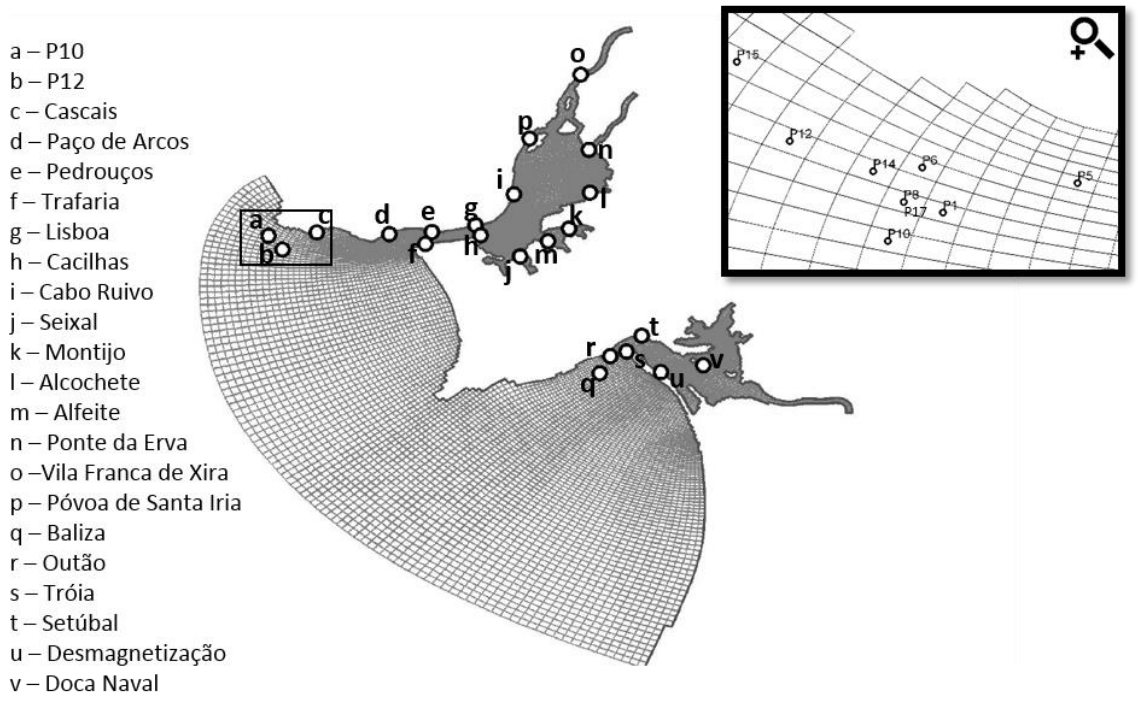

Figure 3.1: Numerical grid and the location of the tide gauge, water temperature and salinity stations used in the model calibration (black square – grid zoom).

Table 3.1: Sample Stations for water level.

Estuary	Station	Latitude (N)	Longitude (W)	Time-series
Tagus	Cascais	38°41'28.54''	9°25'02.35''	1986
	Paço de Arcos	38°41'26.38''	9°17'37.29''	26-01-1972 31-12-1972
	Pedrouços	38°41'36.40''	9°13'31.97''	28-09-1971 27-09-1972
	Trafaria	38°40'32.07''	9°14'08.80''	1972
	Cacilhas	38°41'59.64''	9°09'48.17''	1972
	Lisboa	38°41'17.47''	9°08'53.25''	1972
	Seixal	38°39'03.25''	9°04'38.73''	1972
	Alfeite	38°40'05.34''	9°02'04.11''	09-04-1981 14-05-1981
	Montijo	38°42'04.46''	8°58'36.36''	1972
	Cabo Ruivo	38°45'56.26''	9°05'34.85''	1972
	Alcochete	38°45'25.95''	8°57'57.84''	05-01-1972 31-12-1972
	Ponta da Erva	38°49'35.68''	8°58'10.69''	1972
	Póvoa de Santa Iria	38°51'23.39''	9°03'39.99''	04-08-1972 16-10-1972
	Vila Franca de Xira	38°57'13.23''	8°59'09.59''	1972
Sado	Outão	38°29'32.80''	8°55'57.21''	Harmonic constituents
	Baliza	38°27'02.59''	8°57'00.70''	
	Tróia	38°29'37.53''	8°54'07.71''	
	Setúbal	38°31'15.62''	8°53'05.39''	
	Desmagnetização	38°28'00.19''	8°51'45.23''	
	Setenave	38°28'18.94''	8°47'37.35''	

March 20, June 23, August 20 and October 15 and 16, obtained between 11 am and 4 pm, are summarised in Table 3.2.

Although more data were available for other stations, were not considered in this study due to the closest location between them, as shown in zoom area in Figure 3.1. The stations considered are shown in Figure 3.1. This data set aims the validation of the model.

Table 3.2: Sample Stations for salinity and temperature.

Station	Latitude (N)	Longitude (W)	Sample average depth
P1	009º27'25.98''	38º40'10.98''	40
P5	009º25'43.98''	38º40'40.02''	30
P6	009º27'46.98''	38º40'48.00'	35
P8	009º27'58.98''	38º40'28.98''	40
P10	009º28'19.98''	38º40'04.02''	50
P12	009º29'21.00''	38º40'58.98''	50
P14	009º28'31.98''	38º40'46.98''	40
P15	009º30'00.00''	38º41'46.02''	50
P17	009º28'16.02''	38º40'28.98''	40

3.4. Meteorological

The atmospheric input used in this work was obtained from two different data sets, aiming the calibration of the model. The period obtained was June of 2009 to February of 2010 and July 27 to November 30 of 2012.

The air temperature, relative humidity and radiant heat flux was supplied by the National Center for Environmental Prediction (NCEP) model (http://www.ncep.noaa.gov/). The NCEP reanalysis (Kalnay et al., 1996) has a temporal resolution of 6 h. Several variables were obtained to calculate the radiant heat flux. This budget is composed of the net long and shortwave radiation flux across the atmosphere-ocean interface. Thus, the following variables were obtained: air temperature at 2 m; specific humidity; downwelling shortwave; upwelling shortwave and downwelling longwave.

The wind and atmospheric pressure was supplied by Weather Research and Forecasting Model (WRF) (http://www.wrf-model.org). The WRF model version 3.6 (Skamarock et al., 2008) was applied for the study area. The application developed by Núcleo de Modelação Estuarina e Costeira (NMEC) comprises three two-way nested domains, where the parent domain has a horizontal resolution of 36 km, and the other two domains present 12 and 4 km of resolution, with a temporal resolution of 1 h. The vertical discretization was composed by 28 unequal spaced layers for each domain. The 4 km resolution domain was used between 37.414°N and 40.613°N and -12.709°W and -12.880°W, to generate the input for zonal and meridional wind at 10 m and the atmospheric

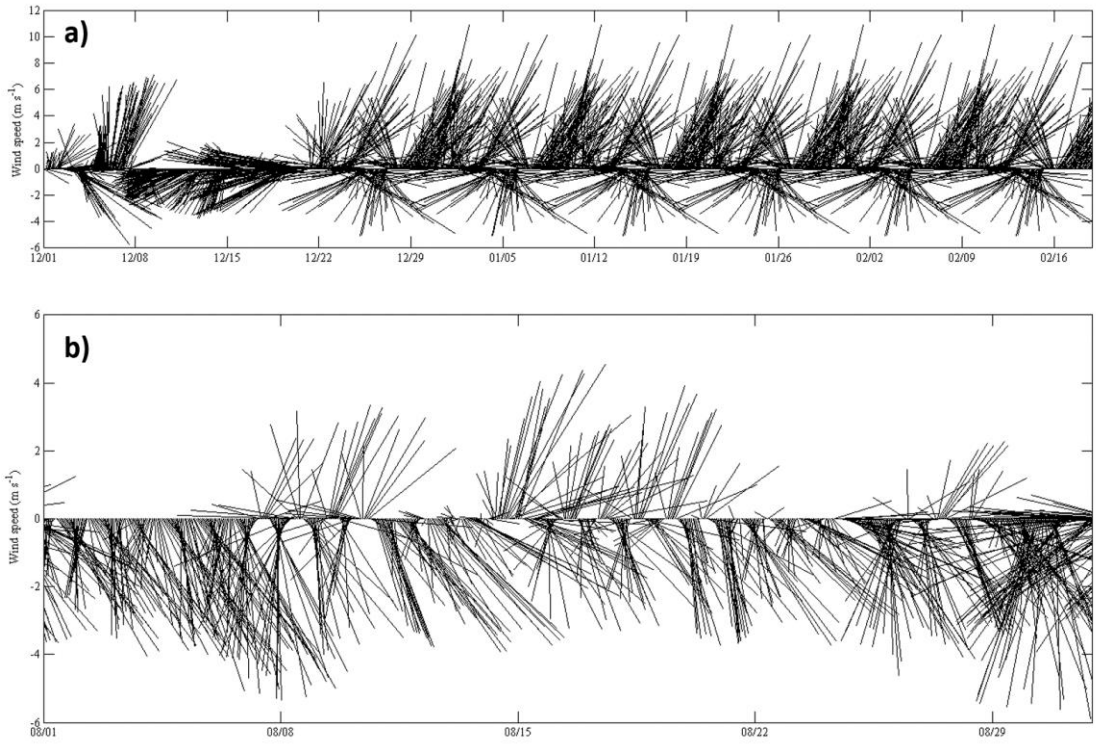

Figure 3.2: Local wind for the study area: wind vector for the period of a) 2009 and b) 2012.

pressure. Figure 3.2a and 3.2b show the wind for the period of 2009/2010 and 2012, respectively.

The wind direction tends to be northward for the period of 2009 – prescribing the winter pattern in this region, and southward for the period of 2012, characteristic of the summer season in the region.

3.5. River discharge

The daily river discharge data were obtained for the Tagus and Sado basin. The Portuguese Agency of Environment (http://www.apambiente.pt/), undertakes flow monitoring in a number of sites within Tagus and Sado River basin, with the longest series of records starting in the early 1930s, available in the internet at the Nacional System of Information of Hydric Resources (SNIRH) (http://snirh.apambiente.pt/).

According to APA there are 177 and 39 stream gauges stations in Tagus and Sado River Basin respectively, from which a significant number is presently inactive. Some stations have flow records, most of them during very short recording periods. From those stations, few are located in the Sorraia River and Vale Michões and Marateca tributaries, and most of them are presently deactivated. In this site it is also available other data, such as meteorological including rainfall.

After a brief analysis of the data available in SNIRH, it was observable numerous flaws, some days to months of data were missing for all the freshwater inflows and inexistence data for the Vale Michões and Marateca tributaries. Thus, a new search was needed to find time-series for the river discharges.

The Hydrological Predictions for the Environment (HYPE) (http://hypeweb.smhi.se/), from the Swedish Meteorological and Hydrological Institute (SMHI) has calculations of long-term series of several variables for the different basins in Europe, such as river discharges and rainfall. Through the HYPE v 2.1 was obtained time series of 30 years (01-01-1980 to 31-12-2010) for Tagus, Sorraia, Sado Rivers and Marateca and Vale Michões tributaries.

For a better approximation of the real freshwater temperature, the temperature of freshwater inputs is the air temperature provided by NCEP, due to the lack of information related to water temperature in both HYPE model and SNIRH database.

The missing discharge data for 2012 led to a research for methods that allow the prediction of discharges. Several documented methods for empirical formulas (Shaw, 1983) and cinematic formulas (Castiglioni et al., 2010) are limited to the hydrographic basin area, or require other variables on which there are no available data. According to Romano et al (2013), all approaches need long time series of rainfall as well as outflow of the basin during the year, in order to be calibrated and validated. Moreover, any methodology has been specifically developed to the

synthetic reconstruction of discharge time series, which is usually performed coupling methodologies devoted to the reconstruction of missing daily rainfall time series to one of the input-output models cited above. Thus, the main goal is to generate synthetic time series of discharge consistent with the observed precipitation regimen in the Tagus and Sado basins for 2012.

For this objective, in section 2 was made a research of the rainfall on the different basins of the five rivers. The datasets were obtained from the European Reanalysis and Observations for Monitoring, with a special resolution of 5 km and daily values of precipitation. Through the functional analysis, it was made a deconvolution of the discharge and precipitation time series for the 30 years (01-01-1980 to 31-12-2010), for all the five freshwater inputs, in order to filter the discharge time-series from the influence of the precipitation. Then, a convolution of the obtained signal was made with the precipitation time-series for the year 2012.

3.6. Summary of the inputs

This chapter presented the necessary inputs for the aims of this work: the bathymetry applied on the grid; the tidal forcing at the open boundaries; the hydrographic data such as water level, water temperature and salinity time series needful for the calibration and validation of the model; the atmospheric input used in the calibration and validation of the model, and in the spinups for the scenarios; and the river discharge used in this work.

Although several problems were encountered when acquiring the necessary data for the atmospheric and river discharge input, it was possible to set the necessary model runs to calibrate and validate the model, and to execute several scenarios.

Thus, these inputs will be taken into account in the next steps which aim the model calibration and validation, and further implementation of several scenarios.

4. Numerical model DELFT3D-Flow

Simulations were carried out using the Delft3D model (research version 9.001). In particular it was used the hydrodynamic module Deflt3D-Flow. Delft3D-Flow is the integrated flow and transport modelling of Deltares for the aquatic environment. The flow model can be used to predict the flow in shallow seas, coastal areas, estuaries, lagoons, rivers and lakes. It aims to model flow phenomena of which the horizontal length and time scales are significantly larger than the vertical scales.

The hydrodynamic module DELFT3D-Flow simulates two-dimensional (2DH, depth-averaged) or three-dimensional (3D) unsteady flow and transport phenomena resulting from tidal and meteorological forcing, including the effect of density differences due to a non-uniform water temperature and salinity distribution (density-driven flow). Three-dimensional modelling is of particular interest in transport problems where the horizontal flow field shows significant variation in the vertical direction (e.g. dispersion of waste or cooling water in coastal areas, upwelling and downwelling of nutrients, salt intrusion in estuaries, fresh water river discharges in bays, thermal stratification in seas and estuarine circulation even in well mixed estuaries) (Deltares, 2011a).

4.1. Numerical aspects

The system of equations solved by the model consists in the horizontal equations of motion, the continuity equation, and the transport equations for conservative constituents. The equations are formulated in orthogonal curvilinear co-ordinates or in spherical co-ordinates on the globe. In curvilinear co-ordinates, the free surface level and bathymetry are related to a flat horizontal plane of reference, whereas in spherical co-ordinates the reference plane follows the Earth's curvature.

In the horizontal direction Delft3D-Flow uses orthogonal curvilinear co-ordinates, in spherical (decimal degrees). In this grid, the quantities such as water levels, salinities and velocities are defined in different locations of the grid as shown in Figure 4.1.

The variables water level and velocity describe the flow and are arranged in a special way on the grid, see Figure 4.1. This particular staggered grid is called the Arakawa C-grid. Water level points (pressure points) are defined in the centre of a (continuity) cell and the velocity components are perpendicular to the grid cell faces where they are situated.

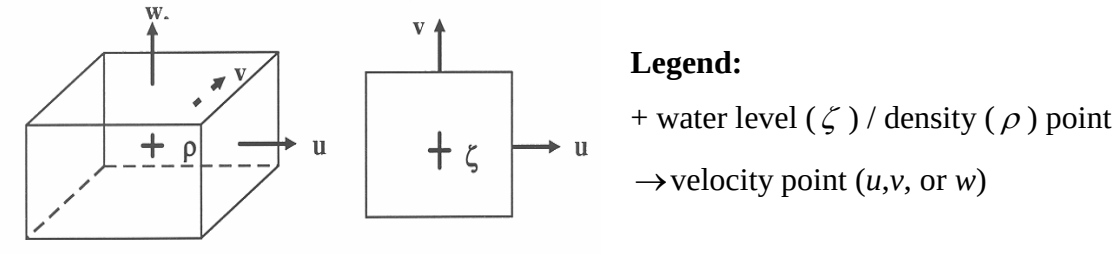

Figure 4.2: Numerical grid and the location of the tide gauge, water temperature and salinity stations used in the model calibration (black square – grid zoom).

This staggered grid has several advantages: the boundary conditions can be implemented in an easier way, giving the possibility to use a smaller number of discrete state variables in comparison with discretizations on non-staggered grids, without affecting the accuracy. Also, for shallow water solvers can prevent spatial oscillations in the water levels (Deltares, 2011a).

In the vertical direction, Delft3D-Flow offers two different vertical grid systems as shown in Figure 4.2: the σ co-ordinate system (σ model) and the Cartesian Z co-ordinate system (Z-model).

In this work, it was chosen the sigma co-ordinate system. This co-ordinate system consists of layers bounded by two sigma planes, which follow the bottom topography and the free surface. The number of layers over the entire horizontal computational area is constant. This approach allows more resolution in the regions of interest such as the surface area.

The σ co-ordinates are defined as:

$$\sigma = \frac{z-\zeta}{d+\zeta} = \frac{z-\zeta}{H} \qquad \textbf{(1)}$$

With z being the vertical co-ordinate in physical space, ζ the free surface elevation above the reference plane (at $z = 0$) and d the depth below the reference plane.

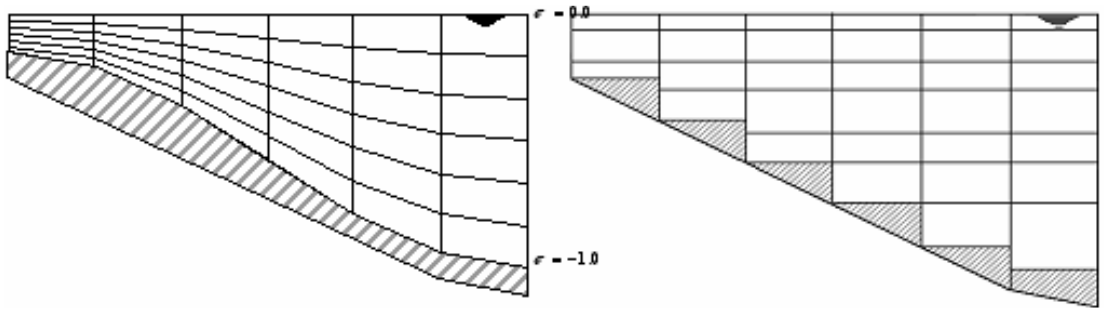

Figure 4.1: Example of σ (sigma-grid on left) and Z-grid (right) (Deltares, 2011a).

4.2. Governing equations

Delft3D-Flow is based on several mathematical formulations that take into account the physical phenomena.

The depth-average continuity equation is a mathematical statement of the conservation of mass (Officer, 1976), given by:

$$\frac{\partial \zeta}{\partial t}+\frac{1}{\sqrt{G_{\xi\xi}}\sqrt{G_{\eta\eta}}}\frac{\partial\left[(d+\zeta)U\sqrt{G_{\eta\eta}}\right]}{\partial \xi}+\frac{1}{\sqrt{G_{\xi\xi}}\sqrt{G_{\eta\eta}}}\frac{\partial\left[(d+\zeta)V\sqrt{G\xi\xi}\right]}{\partial \eta}=Q \qquad \textbf{(2)}$$

With Q representing the contributions per unit area due to the input or output of water through discharge or withdrawal, precipitation and evaporation:

$$Q=H\int_{-1}^{0}\left(q_{in}-q_{out}\right)d\sigma+P-E \qquad \textbf{(3)}$$

With q_{in} and q_{out} the local sources and sinks of water per unit of volume [1/s], respectively, P the non-local source term of precipitation (P = 0 in the present model implementation) and E non-local sink term due to evaporation and $\sqrt{G_{\xi\xi}}$ and $\sqrt{G_{\eta\eta}}$ being the coefficients to transform values from curvilinear to rectangular coordinates (Deltares, 2011a).

The horizontal momentum equations in the x and y directions are defined as:

$$\frac{\partial u}{\partial t}+\frac{u}{\sqrt{G_{\xi\xi}}}\frac{\partial u}{\partial \xi}+\frac{v}{\sqrt{G_{\eta\eta}}}\frac{\partial u}{\partial \eta}+\frac{w}{d+\zeta}\frac{\partial u}{\partial \sigma}-\frac{v^2}{\sqrt{G_{\xi\xi}}\sqrt{G_{\eta\eta}}}\frac{\partial\sqrt{G_{\eta\eta}}}{\partial \xi}+\frac{uv}{\sqrt{G_{\xi\xi}}\sqrt{G_{\eta\eta}}}\frac{\partial\sqrt{G_{\xi\xi}}}{\partial \eta}-fv=$$

$$-\frac{1}{\rho_0\sqrt{G_{\xi\xi}}}P_\xi+F_\xi+\frac{1}{(d+\zeta)^2}\frac{\partial}{\partial\sigma}\left(\nu_v\frac{\partial u}{\partial\sigma}\right)+M_\xi \qquad \textbf{(4)}$$

and

$$\frac{\partial v}{\partial t}+\frac{u}{\sqrt{G_{\xi\xi}}}\frac{\partial v}{\partial \xi}+\frac{v}{\sqrt{G_{\eta\eta}}}\frac{\partial v}{\partial \eta}+\frac{w}{d+\zeta}\frac{\partial v}{\partial \sigma}-\frac{uv}{\sqrt{G_{\xi\xi}}\sqrt{G_{\eta\eta}}}\frac{\partial\sqrt{G_{\eta\eta}}}{\partial \xi}+\frac{u^2}{\sqrt{G_{\xi\xi}}\sqrt{G_{\eta\eta}}}\frac{\partial\sqrt{G_{\xi\xi}}}{\partial \eta}+fu=$$

$$-\frac{1}{\rho_0\sqrt{G_{\eta\eta}}}P_\eta+F_\eta+\frac{1}{(d+\zeta)^2}\frac{\partial}{\partial\sigma}\left(\nu_v\frac{\partial v}{\partial\sigma}\right)+M_\eta \qquad \textbf{(5)}$$

The density variations are neglected, except in the baroclinic pressure terms where P_ξ and P_η represent the pressure gradients. The forces F_ξ and F_η represent the unbalance of horizontal Reynold's stresses. M_ξ and M_η represent the contributions due to external sources of sinks of momentum and the Coriolis parameter f.

The turbulence closure models respond only to shear production. A constant (space and time) background mixing coefficient is specified, which is a background value for the vertical eddy viscosity in the momentum equation (4 and 5). Consequently, the vertical eddy viscosity coefficient ν_v is defined by:

$$\nu_v = \nu_{mol} + \max\left(\nu_{3D}, \nu_H^{back}\right) \tag{6}$$

ν_{mol} being the kinematic viscosity of water, ν_{3D} the three-dimensional part of viscosity and ν_H^{back} the ambient vertical mixing coefficient (Deltares, 2011a).

The vertical velocity *w* in the adapting σ co-ordinate system is computed from the continuity equation:

$$\frac{\partial \zeta}{\partial t} + \frac{1}{\sqrt{G_{\xi\xi}}\sqrt{G_{\eta\eta}}}\frac{\partial\left[(d+\zeta)u\sqrt{G_{\eta\eta}}\right]}{\partial \xi} + \frac{1}{\sqrt{G_{\xi\xi}}\sqrt{G_{\eta\eta}}}\frac{\partial\left[(d+\zeta)v\sqrt{G_{\xi\xi}}\right]}{\partial \eta} + \frac{\partial w}{\partial \sigma} = H\left(q_{in} - q_{out}\right) \tag{7}$$

At the surface the effect of evaporation is taken into account (the precipitation is zero). The vertical velocity *w* is defined at the iso σ -surfaces. *w* is the vertical velocity relative to the moving σ-plane.

Under the shallow water assumption, the vertical momentum equation is reduced to a hydrostatic pressure equation, not taking into account vertical accelerations due to buoyancy effects and due to sudden variations in the bottom topography.

$$\frac{\partial P}{\partial \sigma} = -g\rho H \tag{8}$$

After integration this last equation, the hydrostatic pressure is given by:

$$P = P_{atm} + {}_g H\int_{\sigma}^{0} \rho\left(\xi, \eta, \sigma', t\right) d\sigma' \tag{9}$$

Considering water of constant density and taking into account the atmospheric pressure P_{atm}, the pressure gradients are given by:

$$\frac{1}{\rho_0\sqrt{G_{\xi\xi}}}P_{\xi} = \frac{g}{\sqrt{G_{\xi\xi}}}\frac{\partial \zeta}{\partial \xi} + \frac{1}{\rho_0\sqrt{G_{\xi\xi}}}\frac{\partial P_{atm}}{\partial \xi} \tag{10}$$

$$\frac{1}{\rho_0\sqrt{G_{\eta\eta}}}P_{\eta} = \frac{g}{\sqrt{G_{\eta\eta}}}\frac{\partial \zeta}{\partial \eta} + \frac{1}{\rho_0\sqrt{G_{\eta\eta}}}\frac{\partial P_{atm}}{\partial \eta} \tag{11}$$

These represent the gradients of the free surface level, and so-called barotropic pressure gradients. The atmospheric pressure is included in the system for storm surge simulations. The

atmospheric pressure gradients dominate the external forcing at peak winds during storm events (Deltares, 2011a).

In case of non-uniform density, the density is closely related to the values of water temperature and salinity given by the equation of state: the density of water ρ is a function of salinity (s) and water temperature (t) (UNESCO, 1981). The baroclinic term of the pressure gradient is taken into account to obtain the following expressions for the horizontal pressure gradients:

$$\frac{1}{\rho_0\sqrt{G_{\xi\xi}}}P_\xi = \frac{g}{\sqrt{G_{\xi\xi}}}\frac{\partial\zeta}{\partial\xi} + g\frac{d+\zeta}{\rho_0\sqrt{G_{\xi\xi}}}\int_\sigma^0\left(\frac{\partial\rho}{\partial\xi}+\frac{\partial\rho}{\partial\sigma}\frac{\partial\sigma}{\partial\xi}\right)d\sigma' \qquad \textbf{(12)}$$

$$\frac{1}{\rho_0\sqrt{G_{\eta\eta}}}P_\eta = \frac{g}{\sqrt{G_{\eta\eta}}}\frac{\partial\zeta}{\partial\eta} + g\frac{d+\zeta}{\rho_0\sqrt{G_{\eta\eta}}}\int_\sigma^0\left(\frac{\partial\rho}{\partial\eta}+\frac{\partial\rho}{\partial\sigma}\frac{\partial\sigma}{\partial\eta}\right)d\sigma' \qquad \textbf{(13)}$$

Where the first term in equations 12 and 13 represents the barotropic gradient (without atmospheric pressure gradients) and the second term the baroclinic pressure gradient.

Flows in rivers, estuaries and coastal seas often transport dissolved substances, salinity or heat. This transport is modelled by an advection-diffusion equation in the three co-ordinate directions.

The transport equation is formulated in a conservative form in orthogonal curvilinear co-ordinates in the horizontal direction and σ co-ordinates in the vertical direction:

$$\frac{\partial(d+\zeta)c}{\partial t} + \frac{1}{\sqrt{G_{\xi\xi}}\sqrt{G_{\eta\eta}}}\left\{\frac{\partial\left[\sqrt{G_{\eta\eta}}(d+\zeta)\right]uc}{\partial\xi} + \frac{\partial\left[\sqrt{G_{\xi\xi}}(d+\zeta)\right]vc}{\partial\eta}\right\} + \frac{\partial\omega c}{\partial\sigma} =$$

$$\frac{d+\zeta}{\sqrt{G_{\xi\xi}}\sqrt{G_{\eta\eta}}}\left\{\frac{\partial}{\partial\xi}\left(D_H\frac{\sqrt{G_{\xi\xi}}}{\sqrt{G_{\eta\eta}}}\frac{\partial c}{\partial\xi}\right) + \frac{\partial}{\partial\eta}\left(D_H\frac{\sqrt{G_{\xi\xi}}}{\sqrt{G_{\eta\eta}}}\frac{\partial c}{\partial\eta}\right)\right\} +$$

$$\frac{1}{d+\zeta}\frac{\partial}{\partial\sigma}\left(D_V\frac{\partial c}{\partial\sigma}\right) - \lambda_d(d+\zeta)c + S \qquad \textbf{(14)}$$

With D_H the horizontal diffusion coefficient, D_V the horizontal diffusion coefficient, λ_d representing the first order decay process and S the source and sink terms per unit area due to discharge q_{in} or withdrawal q_{out} of water and/or the exchange of heat through the free surface Q_{tot}:

$$S = (d+\zeta)(q_{in}c_{in} - q_{out}c) + Q_{tot} \qquad \textbf{(15)}$$

4.3. Boundary conditions

To get a well-posed mathematical problem with a unique solution, a set of initial and boundary conditions for water levels and horizontal velocities are specified.

In the σ co-ordinate system, the free surface (σ = 0, or $z = \zeta$) and the bottom (σ = -1, or $z = -d$) are σ co-ordinate surfaces and w is the vertical velocity relative to the σ-plane. The impermeability of the surface and the bottom is defined by:

$$\omega\big|_{\sigma=-1} = 0 \text{ and } \omega\big|_{\sigma=0} = 0 \tag{16}$$

At the seabed, the boundary conditions for the momentum equations in the ζ and η are:

$$\frac{\nu_v}{H}\frac{\partial u}{\partial \sigma}\bigg|_{\sigma=-1} = \frac{1}{\rho_0}\tau_{b\xi} \tag{17}$$

and

$$\frac{\nu_v}{H}\frac{\partial v}{\partial \sigma}\bigg|_{\sigma=-1} = \frac{1}{\rho_0}\tau_{b\eta} \tag{18}$$

where $\tau_{b\xi}$ and $\tau_{b\eta}$ represent the bed stress (Deltares, 2011a).

For three-dimensional flow, a quadratic bed stress formulation is used. The bed shear stress in 3D is related to the current above the bed, is given by:

$$\vec{\tau}_{b3D} = \frac{g\rho_0 \vec{u}_b |\vec{u}_b|}{C_{3D}^2} \tag{19}$$

with $|\vec{u}_b|$ the magnitude of the horizontal velocity in the first layer just above the bed and C_{3D} the three-dimensional Chézy coefficient, and can be expressed in the roughness height z_0 of the bed:

$$C_{3D}^2 = \frac{\sqrt{g}}{k}\ln\left(1 + \frac{\Delta z_b}{2z_0}\right) \tag{20}$$

where z_0 is the actual geometric roughness as a fraction of the RMSE-value of the sub-grid bottom fluctuations (Deltares, 2011a). The default Chezy formulation is for specifying a constant Chezy value for the whole domain. For manning formulation, the Chezy coefficient is related to the Manning roughness coefficient, η, *as*,

$$C = \frac{h^{\frac{1}{6}}}{n} \tag{21}$$

where h is the water depth.

At the free surface, the boundary conditions for the momentum equations are:

$$\frac{\nu_v}{H}\frac{\partial u}{\partial \sigma}\bigg|_{\sigma=0} = \frac{1}{\rho_0}|\vec{\tau}_s|\cos(\theta) \tag{22}$$

and

$$\left.\frac{\nu_v}{H}\frac{\partial v}{\partial \sigma}\right|_{\sigma=0} = \frac{1}{\rho_0}|\vec{\tau}_s|\sin(\theta) \quad \textbf{(23)}$$

where θ is the angle between the wind stress vector and the local direction of the grid-line, and η is constant. Without wind the stress at the free surface is zero. The magnitude of the wind is determined by the following quadratic expression:

$$|\vec{\tau}_s| = \rho_a C_d U_{10}^2 \quad \textbf{(24)}$$

With ρ_a being the density of air, C_d the wind drag coefficient, dependent on U_{10}, and U_{10} the wind speed at 10 meter above the free surface (time and space dependent)

The open water boundaries are virtual "water-water" boundaries, it is the location where the model is connected to the open ocean or freshwater areas. The data used for the boundary conditions are obtained from river discharge measurements, tidal data or from a larger model, which encloses the model – nested models. The incoming tidal waves at open boundary must be well prescribed in order to lower the reflection of the outgoing waves at the boundary and avoid the propagation as a disturbance into the area (Deltares, 2011a).

Several boundary conditions can be chosen depending on the aims:

- Water level:

$$\zeta = F_\zeta(t) + \delta_{atm} \quad \textbf{(25)}$$

- Velocity (in normal direction):

$$U = F_U(t) \quad \textbf{(26)}$$

- Discharge (total and per cell):

$$Q = F_Q(t) \quad \textbf{(27)}$$

- Riemann invariants simulates a weakly reflective boundary, avoiding the reflections of the outgoing waves into the model area. This type of boundary reproduces the mesoscale processes. Assuming zero flow along the boundary, the zero order boundary condition is obtained using the Riemann invariant for the 1D equation at the open boundary:

$$R = U \pm 2\sqrt{gH} \quad \textbf{(28)}$$

The two Riemann invariants are two waves moving in opposite direction with propagation speed $R = U \pm \sqrt{gH}$. Thus, the linearized invariant is given by (positive sign – left boundary):

$$U + 2\sqrt{gH} = U + 2\sqrt{g\left(d+\zeta\right)} \approx U + 2\sqrt{gd} + \zeta\sqrt{\frac{g}{d}} \qquad \frac{|\zeta|}{d} << 1 \tag{29}$$

Stelling (1984) added the time-derivative of the Riemann invariant to the water level boundary conditions in order to make the boundary less reflective for disturbances with the eigen frequency of the model area. This reduces the spin-up time of a model from a cold start:

Water level boundary:

$$\zeta + \alpha \frac{\partial}{\partial t}\left\{U \pm 2\sqrt{gH}\right\} = F_{\zeta}\left(t\right) \tag{30}$$

Velocity boundary:

$$U + \alpha \frac{\partial}{\partial t}\left\{U \pm 2\sqrt{gH}\right\} = F_{U}\left(t\right) \tag{31}$$

For the discharge type of boundary condition, the flow is assumed to be perpendicular to the open boundary. It was prescribed a uniform profile for the freshwater areas, and a 3D profile in the vertical for the open ocean area. A 3D-profile means that the velocity at each sigma-layer is specified as any of the forcing types: Riemann and Harmonic components for the open ocean and time-series for the freshwater areas (for detailed information see Section 4.5.2 in Delft 3D Flow Manual) (Deltares, 2011a).

The closed boundary is situated at the transition between land and water. At a closed boundary, two boundary conditions are prescribed: the flow normal to the boundary and the shear stress along the boundary. The boundary condition for flow normal to the boundary specifies no flow through the boundary, thus the boundary is impermeable. For the shear stress along the boundary the following condition is prescribed: Partial slip. For large-scale simulations, the influence of the shear-stresses along the closed boundary is neglected (Deltares, 2011a).

4.4. Transport boundary conditions

The horizontal transport of dissolved substances in rivers, estuaries, and coastal seas is dominated by advection, considering horizontal diffusion in flow direction being of secondary importance. At an open boundary during inflow, a boundary condition is needed to describe this advective transport. During outflow, the concentration must be free. At inflow is specified the concentration which may be determined by the concentration at outflow of the former ebb period – previous outflows. Usually only the background concentration is known from measurements or from a larger model area, and a special boundary condition based on the concentration in the interior area in combination with a return time is applied, which does not completely fix the

concentration at the background value. This is the so-called Thatcher-Harleman boundary condition (Deltares, 2011a). The return time depends on the renovation of the water at the open boundary.

The transport of dissolved substances such as salt, sediment, and heat is described by the advection-diffusion equation. The concentration is determined by pure advection from the interior area:

$$\frac{\partial C}{\partial t}+\frac{U}{\sqrt{G_{\xi\xi}}}\frac{\partial C}{\partial \xi}=0 \qquad \textbf{(32)}$$

If the concentration at outflow differs from the boundary condition at inflow, there is a discontinuity in the concentration at the turn of the flow. The transition of the concentration at the boundary from the outflow value to the inflow value may take some time, depending on the refreshment of the water in the boundary region. The transition time is called the return time, and called memory-effect for open boundary. The formulation of this memory effect is given by:

$$C(t)=C_{out}+\frac{1}{2}(C_{bnd}-C_{out})\left(\cos\left(\pi\frac{T_{ret}-t_{out}}{T_{ret}}\right)+1\right) \qquad 0\le t_{out}\le T_{ret} \qquad \textbf{(33)}$$

where C_{out} is the computed concentration at the open boundary at the last time of outward flow, C_{bnd} is the background concentration, t_{out} is the elapsed time since the last outflow and T_{ret} is the constituent return period. When the flow turns inward (t_{out} = 0), the concentration is set equal to C_{out}. During the interval $0 \le t_{out} \le T_{ret}$ the concentration will return to the background concentration C_{bnd}. After that period, the concentration will remain C_{bnd}.

The vertical diffusive flux through the free surface and bed is zero with exception of the heat flux through the free surface (Deltares, 2011a).

4.5. Turbulence

The turbulence processes occur in sub-grid scales because the horizontal and vertical grid are too coarse and the time step too large to resolve the turbulent scales of motion. Closure assumptions are needed to filter the equations when using space- and time averaged quantities.

For 3D shallow water flow the horizontal eddy viscosity coefficient V_H and eddy diffusivity coefficient D_H are much larger than the vertical coefficients V_V and D_V. The horizontal coefficients consists in three factors: a part due to molecular viscosity, one due to two-dimensional turbulence another due to three-dimensional turbulence (Deltares, 2011a).

Delft3D-Flow offers four turbulence closure models implemented to determine V_V and D_V:

1. Constant coefficient;
2. Algebraic Eddy viscosity closure Model (AEM);
3. *k-L* turbulence closure model;

4. *k-ε* turbulence closure model.

The first turbulence closure model is based on a constant value which is previously specified, the other three turbulence closure models are based on the eddy viscosity concept of Kolmogorov (1942) and Prandtl (1945), and has the following form:

$$\nu_{3D} = c_{\mu}^{'} L\sqrt{k} \tag{34}$$

With $c_{\mu}^{'}$ being a constant determined by calibration (Rodi, 1984), *L* the mixing length and *k* the turbulent kinetic energy.

Here, only is mentioned the *k-ε* turbulence closure model, for more details for the others turbulence closure models see Delft 3D Flow Manual section 9.5 (Deltares, 2011a).

In the *k-ε* turbulence model, the transport equations must be solved for both the turbulent kinetic energy *k* and for the energy dissipation ε. The mixing length L is then determined from ε and *k* according to:

$$L = C_D \frac{k\sqrt{k}}{\varepsilon} \tag{35}$$

The transport equations for *k* and *ε*, assuming the production, buoyancy and dissipation terms are the dominating terms, and the horizontal length scales are larger than the vertical ones, so:

$$\frac{\partial k}{\partial t} + \frac{u}{\sqrt{G_{\xi\xi}}}\frac{\partial k}{\partial \xi} + \frac{v}{\sqrt{G_{\eta\eta}}}\frac{\partial k}{\partial \eta} + \frac{w}{d+\zeta}\frac{\partial k}{\partial \sigma} = \frac{1}{(d+\zeta)^2}\frac{\partial}{\partial \sigma}\left(D_k \frac{\partial k}{\partial \sigma}\right) + P_k + P_{kw} + B_k - \varepsilon \tag{36}$$

and

$$\frac{\partial \varepsilon}{\partial t} + \frac{u}{\sqrt{G_{\xi\xi}}}\frac{\partial \varepsilon}{\partial \xi} + \frac{v}{\sqrt{G_{\eta\eta}}}\frac{\partial \varepsilon}{\partial \eta} + \frac{w}{d+\zeta}\frac{\partial \varepsilon}{\partial \sigma} =$$

$$\frac{1}{(d+\zeta)^2}\frac{\partial}{\partial \sigma}\left(D_\varepsilon \frac{\partial \varepsilon}{\partial \sigma}\right) + P_\varepsilon + P_{\varepsilon w} + B_\varepsilon - c_{2\varepsilon}\frac{\varepsilon^2}{k} \tag{37}$$

With:

$$D_k = \frac{\nu_{mol}}{\sigma_{mol}} + \frac{\nu_{3D}}{\sigma_k} \text{ and } D_\varepsilon = \frac{\nu_{3D}}{\sigma_\varepsilon}$$

$$P_k = \nu_{3D}\frac{1}{(d+\zeta)^2}\left[\left(\frac{\partial u}{\partial \sigma}\right)^2 + \left(\frac{\partial v}{\partial \sigma}\right)^2\right]$$

$$B_k = \frac{\nu_{3D}}{\rho\sigma_\rho}\frac{g}{H}\frac{\partial \rho}{\partial \sigma^{'}}$$

$$P_\varepsilon = c_{1\varepsilon} \frac{\varepsilon}{k} P_k$$

$$B_\varepsilon = c_{1\varepsilon} \frac{\varepsilon}{k} (1 - c_{3\varepsilon}) B_k$$

With L prescribed by Equation 38 and the calibration constants by (Rodi, 1984):

$c_{1\varepsilon}$ = 1.44

$c_{2\varepsilon}$ = 1.92

$c_{3\varepsilon}$ = 0.0 for unstable stratification, and 1.0 for stable stratification (Deltares, 2011a).

4.6. Heat flux

The heat radiation emitted by the sun reaches the earth, in the atmosphere the radiation scatters, reflection and absorption by air, cloud, dust and particles. On average neither the atmosphere nor the earth accumulates heat, which implies that the absorbed heat is emitted back again. In Delft3D-Flow the heat exchange at the free surface is modelled by taking into account the separate effects of solar (short wave) and atmospheric (long wave) radiation, and heat loss due to back radiation, evaporation and convection.

In Delft3D-Flow five heat flux models are available, however it was used the *Heat flux model 2,* which uses the combined net solar (short wave) and net atmospheric (long wave) radiation. The terms related to heat losses due to evaporation, back radiation and convection are computed by the model. This Heat flux model is based on formulations given by Octavia et al. (1977). The source of data for the combined net incoming radiation terms (Q_{sn} + Q_{an}) must come from direct measurements. The remaining terms (back radiation, evaporation, convection) are computed similarly as for heat flux model option 1 (Deltares, 2011a).

5. Model Implementation

The fate of a model simulation is largely determined by the values of the free model parameters. These parameters reflect the uncertainty on how to model certain physical process and provide the opportunity to tune models using measured data. This section summarizes the free model parameters in the Delft3D-Flow module, which are considered the most uncertain and important given the scope of the study. More specifically for the aim of this study several parameters have been tested and selected for posterior application in the model such as: the calibration factor for ripples and megariples in the roughness predictor. Most of free model parameters have been treated as such in the sensibility analysis, except for the vertical background viscosity and diffusity.

5.1. Model Establishment

The Delft3D-Flow platform was setup with several steps. Initially, a spherical, curvilinear orthogonal grid was designed to represent the main hydrodynamic features of the study area with the minimum number of calculation points. Here, two approaches of grid design were tested in order to check their accuracy to the aim of this work. Thus, in an initial phase it was built a grid using the multi-domain methodology of Delft3D-Flow (for detailed information see section 5.3.11 of Delft3D-RGFGRID User Manual (Deltares, 2011b) as shown in Figure 5.1a. However, this horizontal grid was insufficient for the present work because the region of interest is not well represented in order to evaluate the interactions between the two estuaries. In addition, the domain decomposition frontiers need to be carefully set, due to the abrupt depth in the region, in order to avoid errors in the water velocities. For that reason and taking into account the main aims of this work a second grid was built, giving a special interest in the mouth of the estuaries and in the coastal shore by refining the grid, as shown in Figure 5.1b.

The generation of this new grid was made using the same methodology as used in the first grid. This task was enormously time consuming due to the complex geometry of the study region, with the presence of canyons (abrupt depth changes), narrow channels inside the estuaries and depths from -2500 to 5 meters in the study area. Thus, to generate the presented grid which represents the domain dimensions was necessary to use the tools for irregular grids, and check the orthogonality several times during the process.

In addition, an offshore zone was set to allow the dissipation of spurious open ocean boundary effects before reaching the mouth of both estuaries, however this is required only when the harmonic boundaries are used, and not for the Riemann boundaries. The grid has 253×174 cells

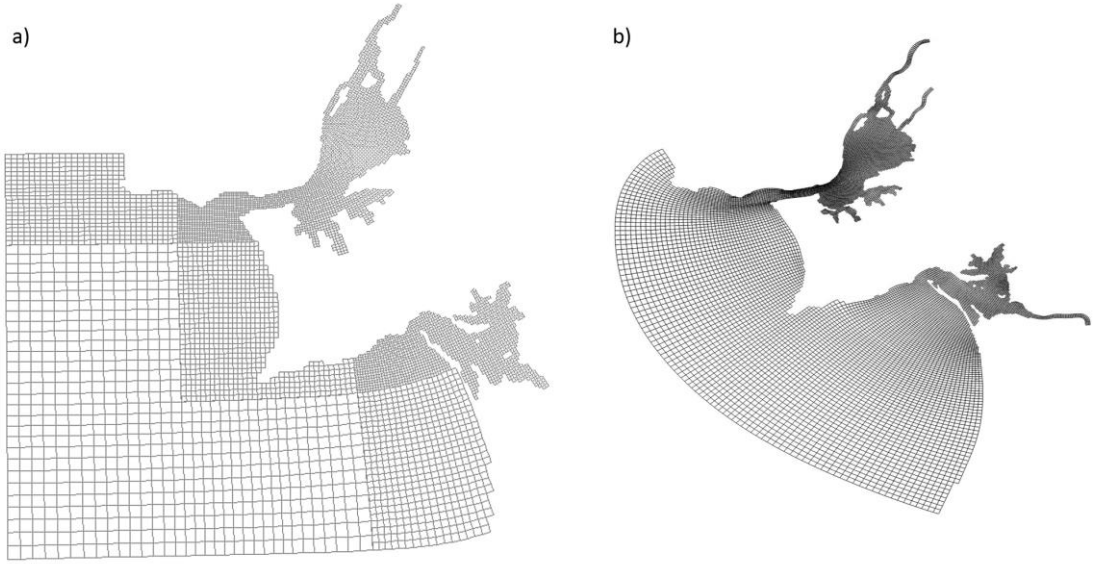

Figure 5.2: Horizontal grid: a) multi-domain. b) single-domain.

with a mean resolution of approximately 450 m (high resolution inside the estuaries and near the coast – 100 m, and lower resolution outside the estuaries – 1500 m). The computational domain extends from the upstream limits of the estuaries to the continental shelf.

The bathymetry used results from the interpolation to the numerical grid of a set of topo-hydrographic surveys as mentioned in section 3.1. The interpolation of this generated bathymetry was made using the tools available in Delft3D-QUICKIN (Deltares, 2011c). This task was equally time consuming due to the format of the several bathymetry samples used (as mentioned in section 3.1). The numerical bathymetry, referent to chart datum, for Lisbon (2.08 m), is presented in Figure 5.2. The model uses 15 sigma layers with refined surface layers, to improve the model's ability to

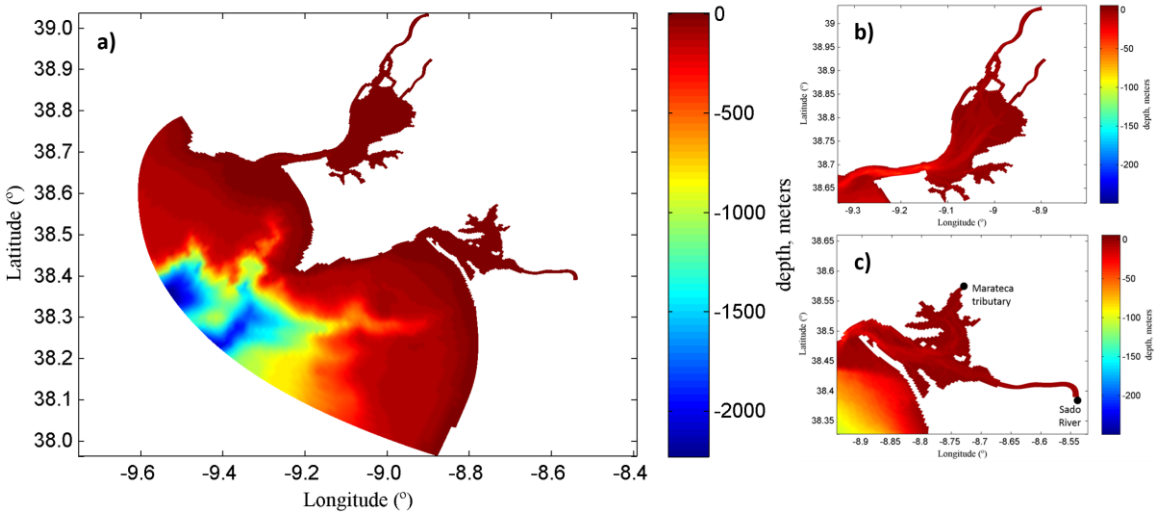

Figure 5.1: Study area numerical bathymetry, with depth in meters relative to chart datum (2.08 m): a) Entire study area; Detail bathymetry of Tagus b) and Sado c) estuaries.

Table 5.1: Percentage of Depth per layer, with layer 1 representing the surface and layer 15 the bottom.

Layer	**1**	**2**	**3**	**4**	**5**	**6**	**7**	**8**	**9**	**10**	**11**	**12**	**13**	**14**	**15**
Percentage of Depth	2	3	4	5	6	8	8	8	8	8	8	8	8	8	8

resolve mixing.

The surface layers were refined comparing to the intermediate and the bottom layers, due to the most important dynamics related to the freshwater plumes occur in the surface layers. The percentage of depth of each layer is presented in Table 5.1.

The propagation of the tide was modelled by prescribing a linearized Riemann invariant (Deltares, 2011a) (weakly reflective boundary condition), i.e. a combination of water levels and velocities, through the use of PCOMS data. It was also used the harmonic forcing in the propagation of the tide in other scenarios. Additionally, it was prescribed the use of a per-layer specified profile at inflow boundaries. The tidal propagation was calibrated through the adjustment of bottom roughness.

To set up the bed roughness were tested several set ups for the bottom roughness coefficient. Initially was tested a linear roughness coefficient, but after a few tests it was observable that a new approach was needed due to the high Root Mean Square Error (RMSE) and low Skill obtained. During the investigation of the bed roughness it was tested the predictor of Van Rijn et al. (2007) for the calibration of bed roughness purpose.

This predictor contains three contributions to the current related roughness, associated with the presence of ripples, mega-ripples and dunes when in the presence of rivers (Briere et al., 2011). However, the preliminary results were slightly worse when compared to a Manning varying bottom roughness, probably due to the lack of information and data for grain size distribution tables (D50) required for the Van Rijn predictor. Thus, it was decided to use a depth dependent Manning coefficient. This parameter assumes the Manning formulation of the Chezy coefficient (Deltares, 2011a). The manning coefficients were adjusted using the guide principle that an increase in the bottom friction will produce a decrease in the tidal wave amplitude in that zone of the channel and in the channel's upstream. Another principle used is that an increase in the bottom roughness will produce an increase in the phase lag for high tide and a decrease for low tide (Fry and Aubrey, 1990). The Manning values used to calibrate the hydrodynamic model were based on the values presented by Dias et al. (2001) and Picado et al. (2010) for the Ria de Aveiro and were adapted in order to achieve a good calibration (Table 5.2).

Table 5.2: Bottom friction coefficients.

Depth (m)	Manning's n values
$-5 \le h < -2.5$	0.028
$-2.5 \le h < -2.0$	0.025
$-2.0 \le h < -1.5$	0.020
$-1.5 \le h < -1.0$	0.016
$-1.0 \le h < 0.0$	0.015
$0.0 \le h < 0.5$	0.022
$0.5 \le h < 1.0$	0.023
$1.0 \le h < 3.0$	0.022
$3.0 \le h < 10.0$	0.020
$10.0 \le h < 5000.0$	0.019

The modelling time step was 30 seconds to be in accordance with the Courant-Friedrichs-Lewy number (CFL). The CFL number of wave propagation is given by:

$$CFL_{wave} = 2\Delta t\sqrt{gH}\sqrt{\frac{1}{\Delta x^2}+\frac{1}{\Delta y^2}} \qquad < \mathbf{1} \qquad \textbf{(38)}$$

Where t is the time step, g is the gravity, H is the depth of the water column and $\Delta x = \sqrt{G_{\xi\xi}}$ and $\Delta y = \sqrt{G_{\eta\eta}}$ are the smallest grid spaces in the ξ- and η-direction, respectively (Deltares, 2011a).

The time step has to be well calculated, if the time step of the model is too large in relation to the grid cell size and the water depth, instabilities can occur and develop from the tidal wave propagations. Decreasing the time step lead to a change in CFL. The maximum values are in the shelf region (11.08) and the lower (0.05) within the bay, being in the range recommended by Deltares (2011b).

Background horizontal eddy viscosity and diffusivity were set to 10 m^2s^{-1}.

A Heat flux model 2 (section 4.2.5) was applied, taking into account air temperature, relative humidity and net solar radiation to calculate heat losses from convection, evaporation and back radiation. These data was obtained from NCEP reanalysis. The wind intensity and direction are obtained from a local implementation of the WRF model, with a resolution of 4 km (Section 3.4).

A total of 5 freshwater points were defined as outflows representing the Tagus, Sorraia, Vale Michões, Sado and Marateca. These time series were obtained from the HYPE v 2.1 hydrological model for the year 2009/2010, and generated for the year 2012.

5.2. Model Calibration and validation

Process or physically based models are simplified representations of natural systems, containing equations that express scientifically accepted principles such as the continuity and momentum conservation for particular processes (see section 4.1) and their manifestation on specific scales of interest.

The model predictions obtained are only reliable as the model assumptions, inputs, and parameters estimates. The presence of parameters in process-based models is a direct consequence of the need to simplify reality or even represent unknown or sub-scale processes. These parameters or parameterizations account for lacking information in the model due to the complexity or non-described spatial and/or temporal variability of the processes considered in the model. The model parameters do not represent measurable attributes of the study area and the generated values have to be determined through calibration using input/output relationships.

The purpose of the calibration in this study is to determine the optimum parameter setting of the Delft3D-FLOW module to compute correctly the flows according to the morphological characteristics in coastal areas with complex bottom topography like the system in study. Several model runs were performed to calibrate the numerical model, in order to reduce the differences between the available observational data and predictions.

The calibration runs were set up from a cold start, including wind forcing, river flow from the Tagus, Sado and Sorraia rivers and Vale Michões and Marateca tributaries. A heat model as well as open-boundary forcing with linearized Riemann invariant were applied. Model predictions were compared against observations (Section 3.3).

The calibration and validation is divided in four steps:

1. Model's ability to represent the tide propagation inside the model domain was evaluated through visual analysis;
2. A comparison between observed and predicted tidal amplitudes and phases of mean tidal constituents;
3. A comparison between observed and predicted temperature and salinity vertical profiles;
4. The predicted and observed horizontal velocities were compared.

For this purpose, step one and two were set up for the year of 2009, where the step three was also performed for the year 2009, on 1st of July. Step four was set up for the period between July and November of 2012. The model set up uses the inputs for the corresponding periods with the available data already mentioned in section 3 of this work.

5.2.1. Hydrodynamic

The model predictions for water level were compared with observations, consisting in sea surface height, taken at 20 stations within the Tagus and in harmonic reconstruction of the tide for the six stations in Sado estuary (Section 3.3).

Following the methodology proposed by Dias and Lopes (2006) at first a visual comparison of observed and predicted water levels was performed. For this, the data set for the stations were compared with modelled sea surface elevations for the same locations. Due to the number of stations, the dimension of the study area, only stations near the mouth and inner (mid and upper) estuaries are represented (Figure 5.3), as shown in Figure 5.4 and 5.5 for Tagus and Sado estuaries, respectively.

The visual comparison shows that the model represents very well the sea surface elevations over the spring-neap cycle.

After the visual comparison, the model performance was quantified by two error parameters: the Root Mean Square Error (RMSE) (Stow et al., 2009) and the Skill (Willmott, 1981) parameter:

$$RMSE = \sqrt{\frac{\sum_{i=1}^{N}\left[\zeta_0(t_i) - \zeta_m(t_i)\right]^2}{N}} \quad \textbf{(39)}$$

Where $\zeta_0(t_i)$ is the observed sea surface elevation at time t_i, $\zeta_m(t_i)$ is the modelled sea surface elevation at time t_i and N is the number of observations. A value close to zero indicates a good model performance. Dias et al. (2009) suggested that an RMSE lower than 5% of the local amplitude represents an excellent agreement between model and observations, while an RMSE between 5% and 10% indicates a very good agreement.

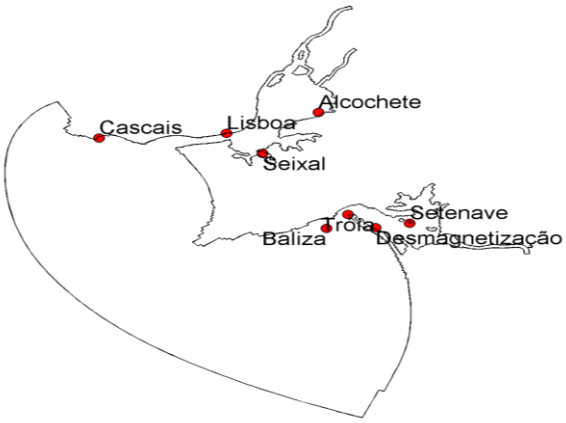

Figure 5.3: Location of the stations used for visual comparison between the observed and predicted water levels.

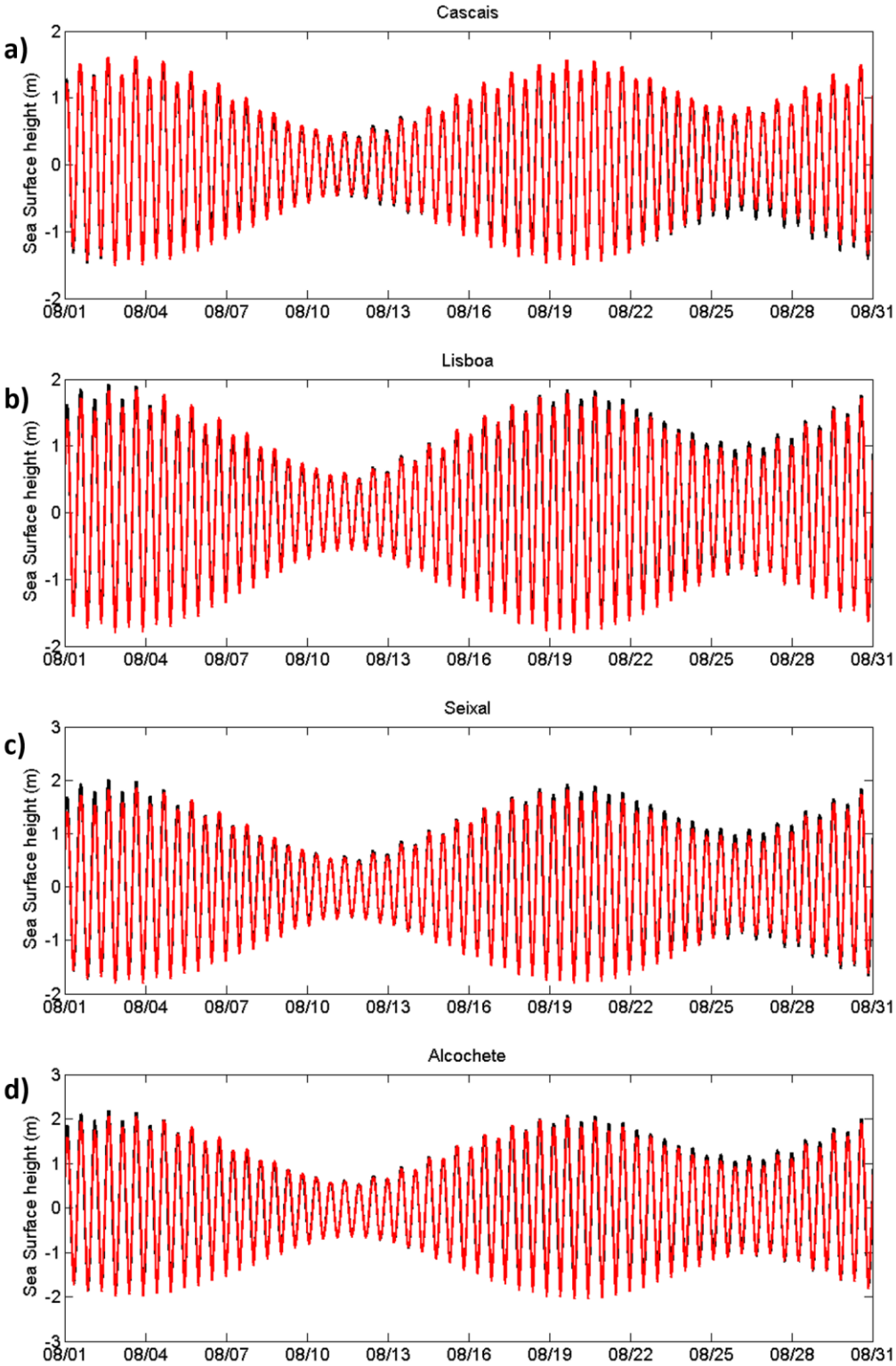

Figure 5.4: Comparison between predicted and observed sea surface height (red line: observed measurements; black: model results) for Tagus: a) Cascais; b) Lisboa; c) Seixal and d) Alcochete stations.

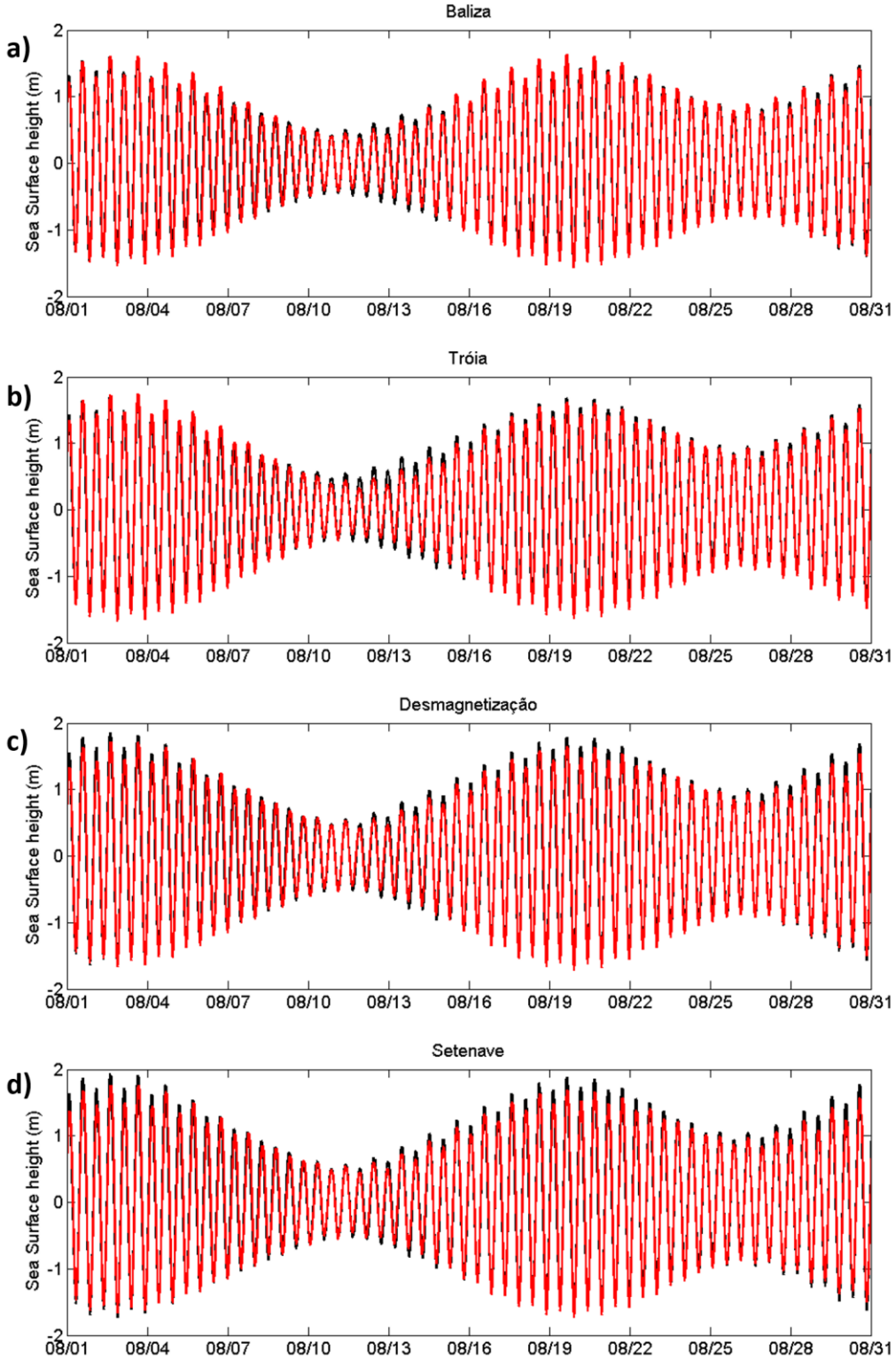

Figure 5.5: Comparison between predicted and observed sea surface height (red line: observed measurements; black: model results) for Sado: a) Baliza; b) Tróia; c) Desmagnetização and d) Setenave stations.

$$Skill = 1 - \frac{\sum \left| \zeta_m - \zeta_0 \right|^2}{\sum \left[\left| \zeta_m - \overline{\zeta}_0 \right| + \left| \zeta_0 - \overline{\zeta}_0 \right| \right]^2} \quad \textbf{(40)}$$

A skill of one means a perfect representation of observations by the model. Dias et al. (2009) suggested that sea surface elevation skills higher than 0.95 can be considered excellent.

The RMSE and Skill were determined for 20 stations within the estuaries (Figure 3.1), for six months of records, as shown in Table 5.3.

RMSE errors of about 9 and 6 cm were found for the stations located at the mouth of Tagus and Sado estuaries, respectively. The best model results were obtained for the stations closer to the estuary's mouth (e.g. Lisboa and Tróia stations with a RMSE of 12 and 8 cm, respectively) and the highest disagreements were found for station Vila Franca de Xira with RMSE around 0.33 m (error of about 7.8 %) of tidal range. Sado stations presents the lowest RMSE values when compared to Tagus stations, this can be explained due to the morphology and the dimension of Tagus estuary, also because all the stations for Sado are relatively close to the estuary mouth, whereas Tagus stations are equally distributed in the estuary. These results have lower RMSE values for all the stations, except for Vila Franca de Xira, than those found in previous studies (Dias et al., 2013b). The skill values were higher than 0.99 for most of the stations in both estuaries, except for Vila Franca de Xira, whose skill is 0.97.

The model's ability in predicting the spring-neap cycle for the inner stations is slightly smaller

Table 5.3: Error values for tidal water levels.

Estuary	Station	RMSE (m)	Skill
Tagus	Cascais	0.0874	0.9967
	Paço de Arcos	0.0951	0.9962
	Pedrouços	0.1064	0.9957
	Trafaria	0.1064	0.9957
	Cacilhas	0.1202	0.9953
	Lisboa	0.1190	0.9954
	Seixal	0.1345	0.9944
	Alfeite	0.1492	0.9935
	Montijo	0.1380	0.9944
	Cabo Ruivo	0.1471	0.9938
	Alcochete	0.1529	0.9938
	Ponta da Erva	0.1775	0.9919
	Póvoa de Santa Iria	0.1874	0.9913
	Vila Franca de Xira	0.3284	0.9732
Sado	Outão	0.0726	0.9977
	Baliza	0.0595	0.9984
	Tróia	0.0801	0.9974
	Setúbal	0.0868	0.9970
	Desmagnetização	0.0953	0.9966
	Setenave	0.1102	0.9957

than the stations near the mouth, indicated by the smaller skill and higher RMSE. Generally, the model predicts the water levels to a satisfactory level.

Harmonic analysis is a method used in the analysis of tidal surface elevations and currents time series. This method uses the least squares technique to examine specific frequencies and to solve for the harmonic constituents. The tidal signal is modelled as the sum of a finite set of sinusoids of specific frequencies, and each one of these frequencies is specified by various combinations of sums and differences of integer multiples of six fundamental frequencies originated by the planetary motions (Godin, 1972).

In this work, the harmonic analysis was performed through the use of T_TIDE, a package of MATLAB routines (Pawlowicz et al., 2002). This harmonic analysis package was applied on a scalar time series – water level. An important feature of this harmonic analysis package is the estimation of the 95% confidence interval associated with each calculated amplitude and phase.

The harmonic analysis was performed to model predictions and observed sea surface height time series. Results for the major semidiurnal and diurnal tidal constituents (M_2, S_2, O_1 and K_1) are presented in Figure 5.6, as well as for the shallow water constituent, M_4.

The agreement between predictions and observations values is good, both in amplitude and in phase for the semidiurnal M_2 and S_2 constituents, which are the major tidal constituents in Tagus and Sado estuaries. For the semidiurnal constituents, which amplitude are the highest, the mean difference between predictions and observations amplitudes are lower for the Stations in Sado and near the mouth of Tagus estuary. The highest differences of amplitude and phase are located in the most inner stations in Tagus estuary (up to 33 cm for M_2 and 0.05 cm for S_2 in Vila Franca de Xira), near the Tagus and Sorraia Rivers.

For the diurnal constituents (O_1 and K_1) the agreement may be considered good for all stations, however for the Alfeite station it was found the highest difference of amplitude and phase.

For the shallow water constituent M_4, the mean difference between model results and observed amplitude and phase shows that the model does not reproduce well the constituent M_4 in the inner stations of Tagus estuary, showing high differences arbitrarily in the stations. The differences found in the M_4 reproduction may be due to bathymetric errors that can not be corrected by the adjustment of the bottom coefficient previously done in section 4.3.1. Bathymetric and water level field data used to calibrate the model were measured with the time gap between 3 and 48 years (bathymetric data was main collected between 1964 and 2009, while the tidal data used in the M_4 was observed in 2012). Additionally according to Araujo et al. (2008), in a similar study for Ria de Aveiro, errors in M_2 amplitude will induce errors in M_4 amplitude.

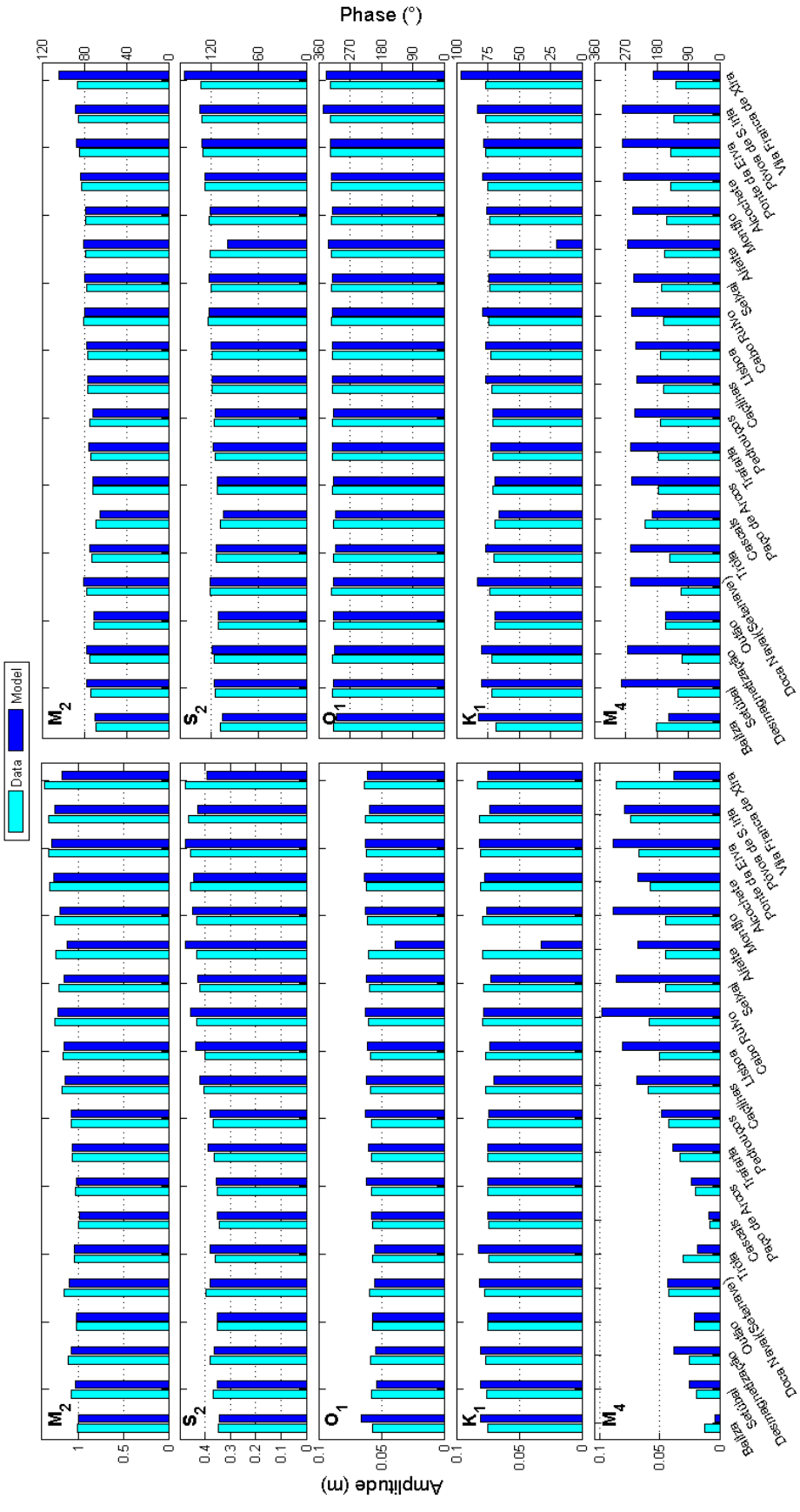

Figure 5.6: Harmonic comparison for the 20 tidal stations spatially distributed in the Tagus and Sado estuaries.

Generally, the model accurately represents the tidal amplitudes, especially for the most important semidiurnal constituents M_2 and S_2.

The model's performance concerning horizontal velocities at surface was furthermore determined by applying the RMSE and skill parameters between model predictions and observations though the high frequency radar - *Sistema de Monitorização Operacional de Correntes Costeiras* (SIMOC) (http://www.hidrografico.pt/simoc.php), for the period between July and November of 2012. The model used the generated discharges for the year of 2012. Also, RMSE and skill calculation consider the month of August.

The SIMOC data has different spatial resolution than the model, which led to an interpolation of the grids and the data to the same spatial resolution. Then, after a brief observation of the SIMOC data revealed the existence of several gaps during this period, which were necessary processed in order to perform the RMSE and Skill calculation.

Figure 5.7 shows that velocity components *u* and *v* are well represented near the shoreline, with low RMSE (Figure 5.7 a,c) and high skill (Figure 5.7 b,d) values. The velocity components are represented less accurately by the model (with skill values between 0.7 and 0.95) near the

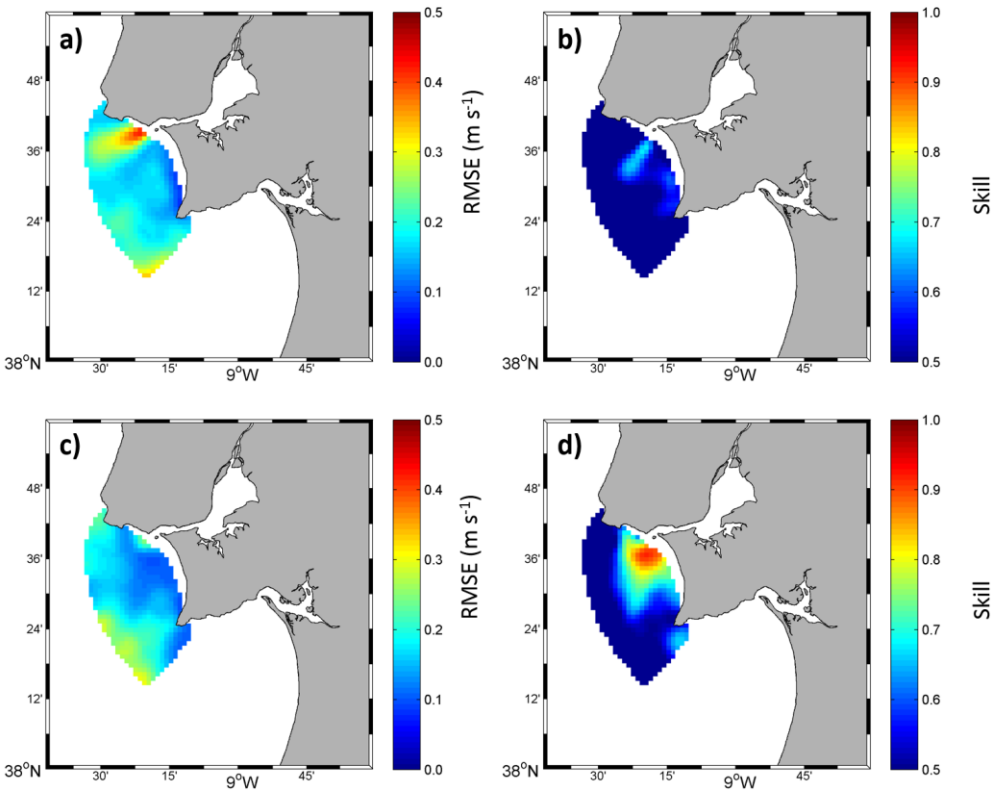

Figure 5.7: Horizontal velocities: RMSE values for *u* a) and *v* c) direction, and skill values for *u* b) and *v* d) direction.

shoreline and in the western part of the study below 0.5.

Skill values are comparably low due to the small variability within the data, even if the RMSE indicates a good fit of the model. Small differences of RMSE are observed in the proximity of the shoreline. High values of RMSE are generally found due to the model predicting higher velocities than those found in observations.

Generally the model accurately reproduces the coastal currents at surface, which have an important role on the buoyancy of freshwater plumes.

5.2.2. Salt and heat transport

Observations of salinity and water temperature consist in CTD profiles obtained in surveys taken in 2008-2009 (section 3.3.2). The surveys of July 1 of 2009 were chosen to perform the model calibration. A total of 9 stations with vertical profiles of salinity and water temperature are available, however, due to their geographic proximity and the grid resolution adopted in this work, only 2 stations will be considered for this study (Figure 5.8). As observed in Figure 5.8, the water temperature is well represented over the stations P10 and P12, with differences between predictions and observations around 1.5°C. Salinities profiles show the same pattern between predictions and observations salinities, with differences comprising 0.5. The results for salinity are similar to those found in previous studies (Vaz et al., 2009).

Generally, the model reproduces the observed patterns, although predicting lower water

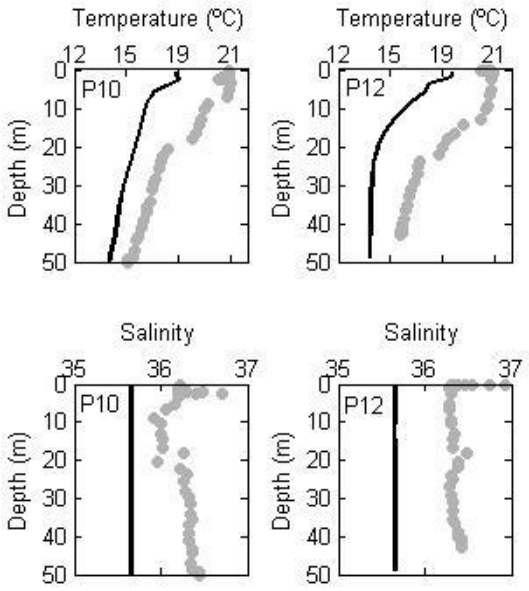

Figure 5.8: Observations (points) and predictions (black line) for salinity vertical profiles for the sampling stations P10 and P12, for July 1 of 2009.

temperature and salinity than observed.

5.3. Limitations of the model

Lencart e Silva (2007) stated that hydrodynamic model's performance is largely influenced by the accuracy of the bathymetry used. As mentioned before, the bathymetry applied in this model result from a compilation of data surveys collected between 1964 and 2009, and considering that the study area is a dynamic system, the bathymetry in 2012, when the observational data was collected may significantly differ from the bathymetry used in the model.

Even after the calibration, uncertainties remain, the high RMSE of the velocity component *u*. A possible source of these uncertainties can be the input discharge of the model for Tagus River, due the error associated to the generation of the discharge for the summer of 2012, since Tagus River is highly dependent on the dams discharge along its course.

Another limitation of the model is the lack of the offshore mesoscale dynamics, when using the Harmonic forcing, due to the limited spatial extent of the model over open ocean, meaning that no fronts on the shelf or mesoscale currents outside the domain can be represented.

6. Model Application

6.1. Setup

Different scenarios were developed to investigate the hydrodynamic response of Tagus and Sado estuarine plumes to river discharges and wind forcing. The scenarios were setup from two different spin-ups, under winter season of 2009-2010 conditions.

The spin-ups have the same conditions as the calibration runs, including wind forcing, river flows from the Tagus, Sado and Sorraia rivers and Vale Michões and Marateca tributaries and a heat flux model. However, two different open ocean boundary forcing were applied, one with linearized Riemann invariant, with water levels and water velocities, salinities and water temperatures. The second with harmonic open ocean boundary forcing. All scenarios were run for 10-days after a 2 weeks spin-up.

The final modelling configurations are common to all production runs, and are listed in Table 6.1.

Table 6.1: Modelling configuration for the study area.

Parameter	Specification
Layers	15, top layers refined
Time step	30 seconds
Duration	10 days
Constituents	Salinity, water temperature, conservative tracer for Tagus and Sado
Wind	Variable
Discharge	Variable
Waves	No
Tide	Warm start of 2 weeks
Initial Conditions	Warm start of 2 weeks
Boundary Forcing	Riemann invariant Harmonic constituents
Bottom roughness method	Variable Manning coefficient
Wall slip condition	Free
Background horizontal eddy viscosity	10 m^2s^{-1}
Background horizontal eddy diffusity	10 m^2s^{-1}
Background vertical eddy viscosity	0
Background vertical eddy diffusity	0
Turbulence closure	k-ε
Threshold depth	0.1 m
Temperature	Heat flux model
Heat flux model	Absolute flux, net solar radiation

6.1. Ocean Boundaries

Two sets of scenarios were chosen: one with linearized Riemann Invariant, and other with harmonic forcing at the open ocean boundaries. Here, the main goal is testing the two forcing's and evaluate the propagation of the estuarine plumes in the nearby coastal region, as well as evaluate if punctual water intrusions occur from the neighbor estuary.

As mentioned in Section 4.4, the Riemann boundaries includes water levels, velocities, salinities and temperatures. This boundary imposition method has the advantage of accurately reproduce the mesoscale currents. On the other hand, the harmonic imposition method includes water levels, salinities and temperatures, and cannot reproduce the mesoscale currents. However, astronomic water level boundaries produce more errors that may propagate inside the model.

6.2. Runoff

Following the methodology adopted by Sousa et al. (2014a), a statistical analysis of the rivers discharge was applied. This consists in the analysis of the maximum annual values for the six rivers discharges in order to characterize the extreme discharge events. This statistical procedure identified the most probable river discharge at a chosen probability of non-exceedance. As presented in previous sections of this work, the Tagus River (Figure 6.1a) and Sado River (Figure 6.1b) have the highest discharges amount, and can represent the discharge pattern for each estuary. Therefore, only in Figure 6.1 is shown the maximum annual values for these Rivers, as well as the probability distributions.

This study considers the following probability distributions: Generalized Extreme Value distribution (GEV), Gamma, Log-normal, Exponential and Weibull. The best distribution was

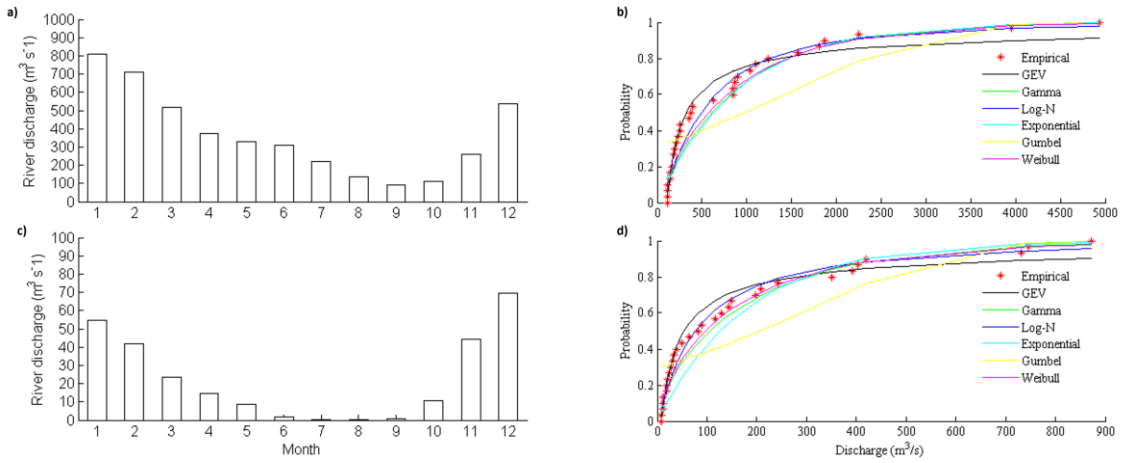

Figure 6.1: Monthly mean of Tagus a) and Sado c) discharge for the period January 1980 to December 2010. Probability distributions for Tagus b) and Sado d) discharge.

Table 6.2: Non exceedance Probability (NEP).

	River discharges ($m^3 s^{-1}$)				
NEP	**Tagus**	**Sorraia**	**Vale Michões**	**Sado**	**Marateca**
0.05	118	8	1	4	1
0.20	158	14	2	10	3
0.50	324	45	8	35	7
0.80	1359	259	26	162	23
0.95	11575	2771	83	1167	119

selected according to the best fit between the empirical cumulative distribution and each analytical probability distribution (Figure 6.1b,d). The best distribution was chosen based on the Chi-squared, Kolmogorov-Smirnov (95% confidence level) and RMSE results between empirical and analytical distribution pairs. The GEV distribution gives the best fit, with the lowest RMSE value for the 5 rivers discharges (Tagus in Figure 6.1b, Sado in Figure 6.1d). From these probability distributions, the discharges for non-exceedance probability (NEP) of 0.05, 0.20, 0.50, 0.80 and 0.95 were calculated and are shown in Table 6.2.

6.3. Atmosphere

Each set of scenarios have different wind directions of 6 m s^{-1} blowing from each of the main four compass points, as well as a no wind condition.

The NCEP input (Section 3.4) was used for the air temperature and the radiant flux for all the scenarios.

6.4. Tracers

Two conservative passive tracers were introduced in all model runs, one for Tagus (Figure 6.2a) and other for Sado (Figure 6.2b) estuary, in the 15 layers, with a concentration of 1000 kg m^{-3}. The tracer were applied to the area covered by the mask in Figure 6.2, in order to investigate the estuarine plumes propagation through the domain and observe the exchanges between the estuaries. The tracer was also introduced in all freshwater inputs with the same concentration, to keep a source of the tracer in each estuary.

This method has the advantage to characterize the water masses and estuarine plumes from the Tagus and Sado estuary. The reliability of using the tracer to evaluate the plume propagation and the water masses is higher than salinity fields, due to the different characteristics of estuarine plumes and water masses. Estuarine plumes have different spatial scales, thinning, spreading and buoyancy, while the water masses can move at any depth.

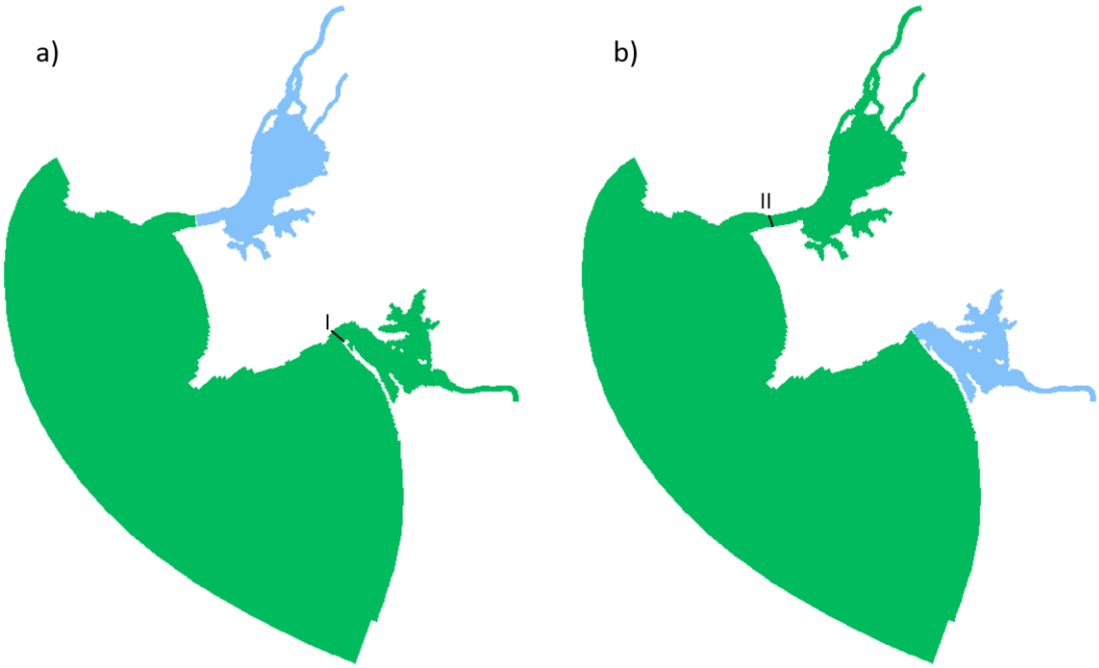

Figure 6.2: Mask applied to the grid area to calculate the propagation of the estuary plume of a) Tagus and b) Sado, blue and green being the dye with concentration of 1000 and 0 kg m^{-3}, respectively. Cross-section to measure the advected tracer from I) Tagus estuary and II) Sado estuary.

The intrusion of the water masses are observed through the calculation of the cumulative advection of the tracer in cross-sections I and II, as shown in Figure 6.2. The cumulative advection of Tagus tracer is measured in cross-section I (Figure 6.2a) at the entrance of Sado estuary, on the other hand the cumulative advection of Sado tracer is measured in cross-section II (Figure 6.2b), at the entrance of Tagus estuary. This method allows measuring the advected quantity of tracer that intrudes in each estuary, in a selected layer or in the 15 layers.

6.5. Summary of the model runs

With all the data acquired in the previous chapters, it was possible to calibrate the model for the sea surface height, through direct comparison between predictions and observations, calculation of RMSE and Skill and harmonic analysis. For the validation, temperature and salinity vertical profiles and horizontal velocities fields were used to calculate the RMS and Skill for the velocity fields, salinity and temperature profiles.

After the calibration and validation process, it was possible to proceed for the application of the model for idealized scenarios.

Two sets of scenarios were chosen, with linearized Riemann Invariant and with harmonic forcing at the open ocean boundaries. Taking into account the river discharges (Table 6.2), several numerical experiments were defined to investigate the distribution and behavior of the Tagus and Sado estuarine plumes considering three scenarios of high (0.95), moderate (0.80) and lower river

(0.50) discharges, combined with wind conditions, and considering a no wind condition (Table 6.3). Five scenarios with idealized high discharges, varying the wind directions and with no wind compose each set.

The results of these five scenarios were analyzed through the analysis of the cumulative advection of the tracer in cross-sections I and II. After the analysis, eight new scenarios were developed considering the scenarios where the intrusion of tracer was worth analyzing, for 0.80 and 0.50 of non-exceedance probability. In addition, four scenarios for 0.80, and four scenarios for 0.50 non-exceedance probability were done, considering North Wind, East Wind, South Wind and without wind.

This methodology also allowed in order to observe how Tagus and Sado estuarine water masses move, when advected to the interior or outside of the estuaries. Vertical profiles are shown at a point located in each one of the estuary's mouth.

Table 6.3: Overview of the scenarios used for simulations.

	Rivers input	**Discharge (non-exceedance probability – Table 4.6)**	**Wind direction (°CW from N)**	**Wind speed (m s^{-1})**	**Tide**
First set	Tagus, Sorraia, Sado, Vale Michões, Marateca	0.95	0	6	Riemann
		0.95	90	6	
		0.95	180	6	
		0.95	270	6	
		0.95	-	-	
		0.80	0	6	
		0.80	90	6	
		0.80	180	6	
		0.80	-	-	
		0.50	0	6	
		0.50	90	6	
		0.50	180	6	
		0.50	-		
Second set	Tagus, Sorraia, Sado, Vale Michões, Marateca	0.95	0	6	Harmonic
		0.95	90	6	
		0.95	180	6	
		0.95	270	6	
		0.95	-	-	
		0.80	0	6	
		0.80	90	6	
		0.80	180	6	
		0.80	-	-	
		0.50	0	6	
		0.50	90	6	
		0.50	180	6	
		0.50	-		

Varying these different characteristics, a set of 26 different scenarios was developed in order to study the region hydrodynamics, as well as the possible conditions for the propagation of the estuarine plumes and the associated patterns at the surface layer. All scenarios are summarized in Table 6.3.

Thus, these scenarios will be analysed to evaluate the key processes in the propagation of the estuaries plumes, through the analysis of a tracer injected on the 15 layers inside the estuaries and in all freshwater inputs.

7. Results and Discussion

The wind forcing and the rivers discharge play an important role in the dispersion of the Tagus and Sado estuarine plumes through the nearby coastal region. This section will be presented the results for the different scenarios (see Table 6.3), in two sets: firstly, the results for linearized Riemann invariant forcing, and secondly the results for Harmonic forcing at the open ocean boundaries. The main goal here is to evaluate how mesoscale affect the transport of the water masses from the Tagus and Sado estuary.

Scenarios have a duration of 10-days, with the same initial conditions from a previous run as spin-up (see Section 6.1). The initial instant for each scenario is midnight of January 1st of 2010, and the last is midnight of January 11th of 2010.

To allow a better comprehension of the propagation of estuarine plumes was prescribed a separate tracer for each estuary individually: one tracer for Tagus estuary plume and other tracer for Sado estuary plume. The propagation of the estuary's plume and the water masses will be evaluated through the analysis of the tracer dispersion at the first layer and at the bottom layer - it was chosen the layer 14, in order to neglect the hydrodynamic effects due to bottom friction- for each one of the tracers.

Several scenarios for discharges of 0.95 of non-exceedance probability, with different wind directions and the absence of wind were evaluated, by measuring the cumulative tracer advected for the neighbor cross-section (Figure 7.1). After a careful analysis, new scenarios were made for the discharges of 0.80 and 0.50 of non-exceedance probability, with different wind directions and the absence of wind, for the scenarios where it was evident the presence of significant quantity of tracer in the neighbor estuary's mouth.

Vertical profiles will be shown at a point, located in each one of the estuary's mouth in order to observe how both tracers behave when they are advected to the interior or outside of the estuaries.

The associated mesoscale patterns will be analyzed to determine how the plume front propagates in the coastal region and in some scenarios intrudes in the estuaries.

As mentioned before, every scenarios starts from a common instant, with common tracer concentration and dispersion as shown in Figure 7.1, and according to the different forcing's mentioned in Table 6.3 in scenarios, the tracer propagation is recorded and presented in the next sub-sections of this work.

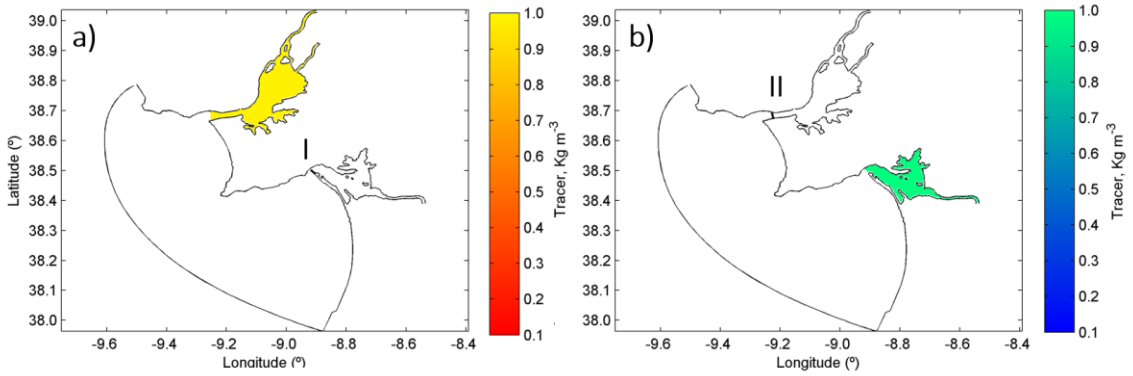

Figure 7.1: Initial instant for Tagus (left panel) and Sado (right panel) in all scenarios, for all the layers. Cross-section to measure the advected tracer from I) Tagus estuary and II) Sado estuary. Colorbar: yellow and green being the dye concentration of 1 and blue and red the concentration 0 kg m^{-3}, for Tagus and Sado estuaries respectively.

7.1. Plume propagation

7.1.1. Mesoscale currents

Horizontal profiles at surface and bottom layer were calculated over the study area, taking into account tracer concentrations between 0 and 1 for a better visualization of the dispersion. The plumes are shown in the following figures, being defined as surface-advected plumes following Yankovsky and Chapman (1997) classification. The wind forcing and the river discharge play an important role in the dispersion of the Tagus and Sado estuarine plumes. To allow a better comprehension of the estuarine water was considered two distinct color-range for each tracer: yellow-red scale for Tagus tracer (Figure 7.1a) and green-blue for Sado tracer (Figure 7.1b).

Winds for the four different directions, and with no wind, associated with high discharge of 0.95 non-exceedance probability, are shown in the following Figures for 240 hours after discharge. The influence of Tagus estuarine water scenarios are shown in Figure 7.2, and Sado estuarine water scenarios in Figure 7.3, for the surface (Figure 7.2 and Figure 7.3 a,b,c,d,e) and near bottom (Figure 7.2 and Figure 7.3 f,g,h,i,j) layers.

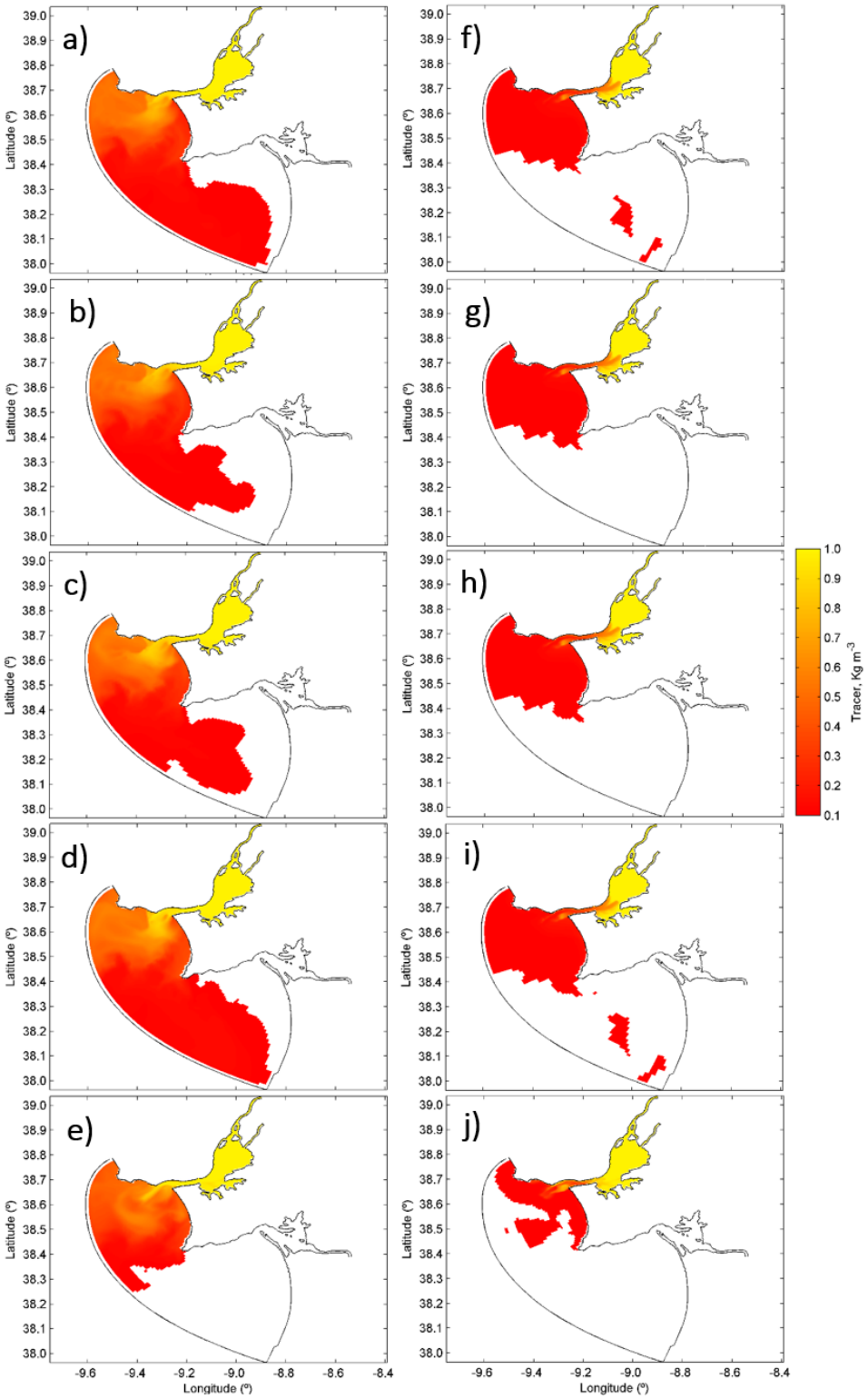

Figure 7.2: Tagus scenarios after 10 days for the surface layer (left) and bottom layer (right), under high river discharges of 0.95 non-exceedance probability for southward (a,f), westward (b,g), northward (c,h), eastward (d,i) winds of 6 m s^{-1} and without wind (e,j) for mesoscale currents.

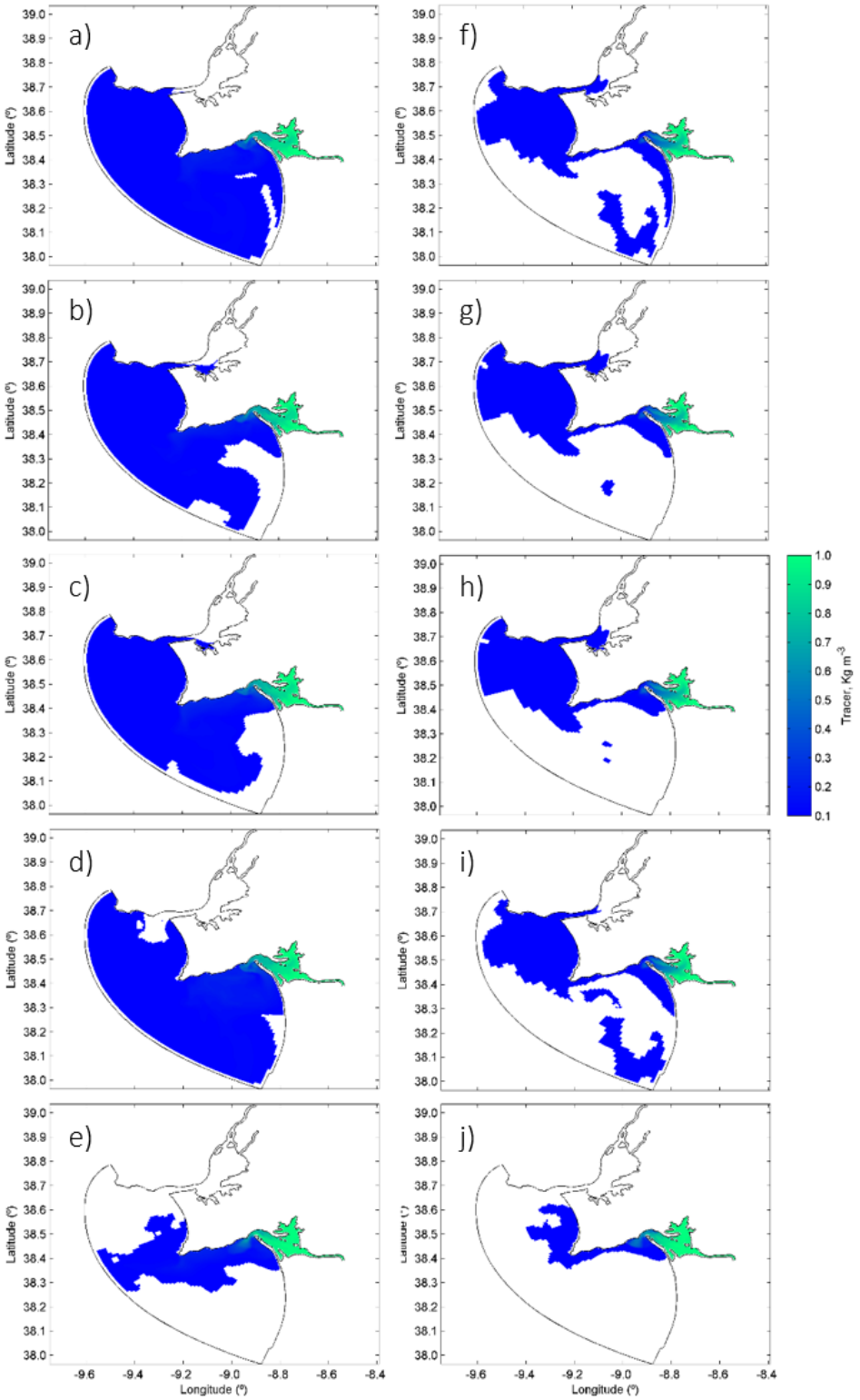

Figure 7.3: Sado scenarios after 10 days for the surface layer (left) and bottom layer (right), under high river discharges of 0.95 non-exceedance probability for southward (a,f), westward (b,g), northward (c,h), eastward (d,i) winds of 6 m s^{-1} and without wind (e,j) for mesoscale currents.

As can be observed in Figure 7.2, after 240 hours of high discharge, the Tagus estuarine plume flows out of the estuary and generally propagates offshore in North-northwest direction, following the pattern observed in previous studies (Valente and da Silva, 2009b; Vaz et al., 2009). A visual analysis of the estuarine plume shows that under every scenario of wind forcing the Tagus plume expands offshore and south, creating a bulge in front of the coastal region (Figure 7.2 a, b, c, d), with a larger area impacted on scenarios with southward (Figure 7.2a) and eastward (Figure 7.2d) winds. In absence of wind, it is observable that the Tagus estuarine plume has a smaller area when compared to wind scenarios cases. However, in all the scenarios of different wind directions and without wind, the Tagus estuarine plume propagates southward without affecting the Sado estuary circulation.

On the other hand, under westward (Figure 7.3 b,g) and northward (Figure 7.3 c,h) winds, the Sado estuarine plume spreads towards the Tagus estuary at the surface and bottom layer. Southward (Figure 7.3a) and eastward (Figure 7.3d) winds tend to induce an accumulation of buoyant water near the Tagus estuary mouth at surface, but at the bottom layer (Figure 7.3f and 7.3I, respectively) the Sado estuarine plume spreads towards the Tagus estuary. With no wind forcing, the Sado estuarine plume tends to propagate north-northwest, confined to the coastline towards Tagus estuary mouth.

As observed in Figure 7.3, under 0.95 non-exceedance probability discharges, a plume intrusion is observed in Tagus estuary after a 10-day period. To observe which discharge most influences the propagation of the Sado plume towards the Tagus estuary, an evaluation of the cumulative advective transport of Tagus and Sado tracer is reported in cross-sections I and II, respectively.

Thus, Figure 7.4a shows the cumulative advective transport of Sado tracer that was registered

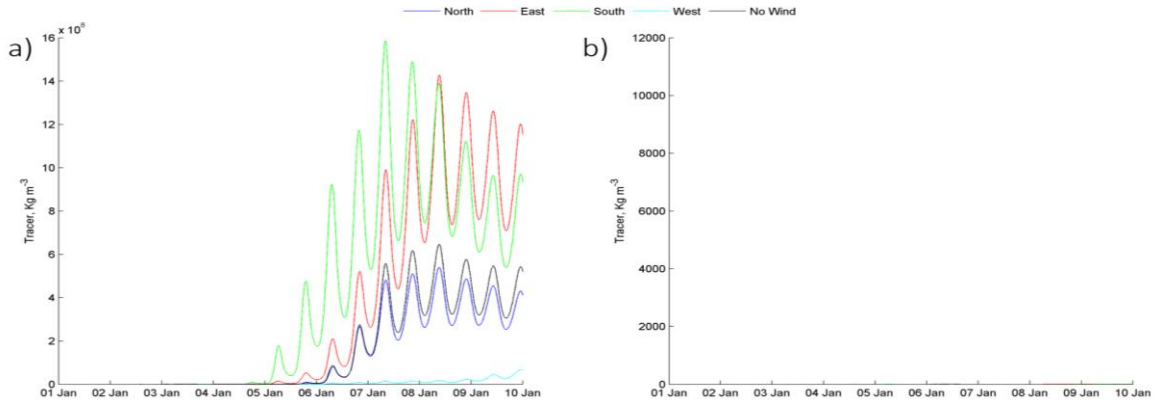

Figure 7.4: Cumulative advective transport of a) Sado tracer in Cross-section II and b) Tagus tracer in Cross-section I, under high river discharges of 0.95 non-exceedance probability for the different scenarios of wind.

in cross-section II, and Figure 7.4b the cumulative advective transport of Tagus tracer registered in cross-section I.

Figure 7.4 supports the results observed in Figure 7.2 and Figure 7.3. In all scenarios of different wind directions the Sado estuarine water intrudes in Tagus estuary, even in the absence of wind forcing. However, the comparison between Figure 7.4a and Figure 7.3e,j suggests that Sado estuarine water intrudes in Tagus estuary in the absence of wind, but the horizontal profiles do not show the same evidence. This is explained due to the 15 layers considered by the model, whereas only the surface and bottom layers are shown in the Figures, suggesting that Sado estuarine water intrudes in the middle layers in Tagus estuary.

Figure 7.4a also indicates that under different wind conditions the Sado estuarine plume arrived at different moments at the Tagus estuary, taking less time with northward winds (around 120 hours after the run start) following by westward winds (around 126 hours), indicated by high concentrations of advected Sado tracer up to $18x10^{16}$ kg m^{-3}, which represent the Sado estuarine water.

At the end of 5^{th} day, in southward and no wind scenarios, the Sado estuarine plume intruded in Tagus estuary, reaching high concentrations of Sado tracer, of 6.2 and $5.8x10^{16}$ kg m^{-3} respectively. In eastward wind scenario, the Sado tracer took longer to reach the Tagus estuary than in the other scenarios. The Sado tracer was observable only after 144 hours of the simulation start, and advected low tracer concentration. This indicates that eastward winds are not favorable for the Sado estuarine water propagation into Tagus estuary.

Figure 7.4b demonstrate that Tagus estuarine water does not propagate to the Sado estuary during the 10-day simulations.

Stated this, a new set of simulations with discharges of 0.80 (Figure 7.5 and Figure 7.6) and 0.50 (Figure 7.7 and Figure 7.8) non-exceedance probability for northward, westward and southward winds, and without wind were performed. The eastward wind scenario was neglected due to the low concentration of the Sado tracer as evidenced in Figure 7.4a.

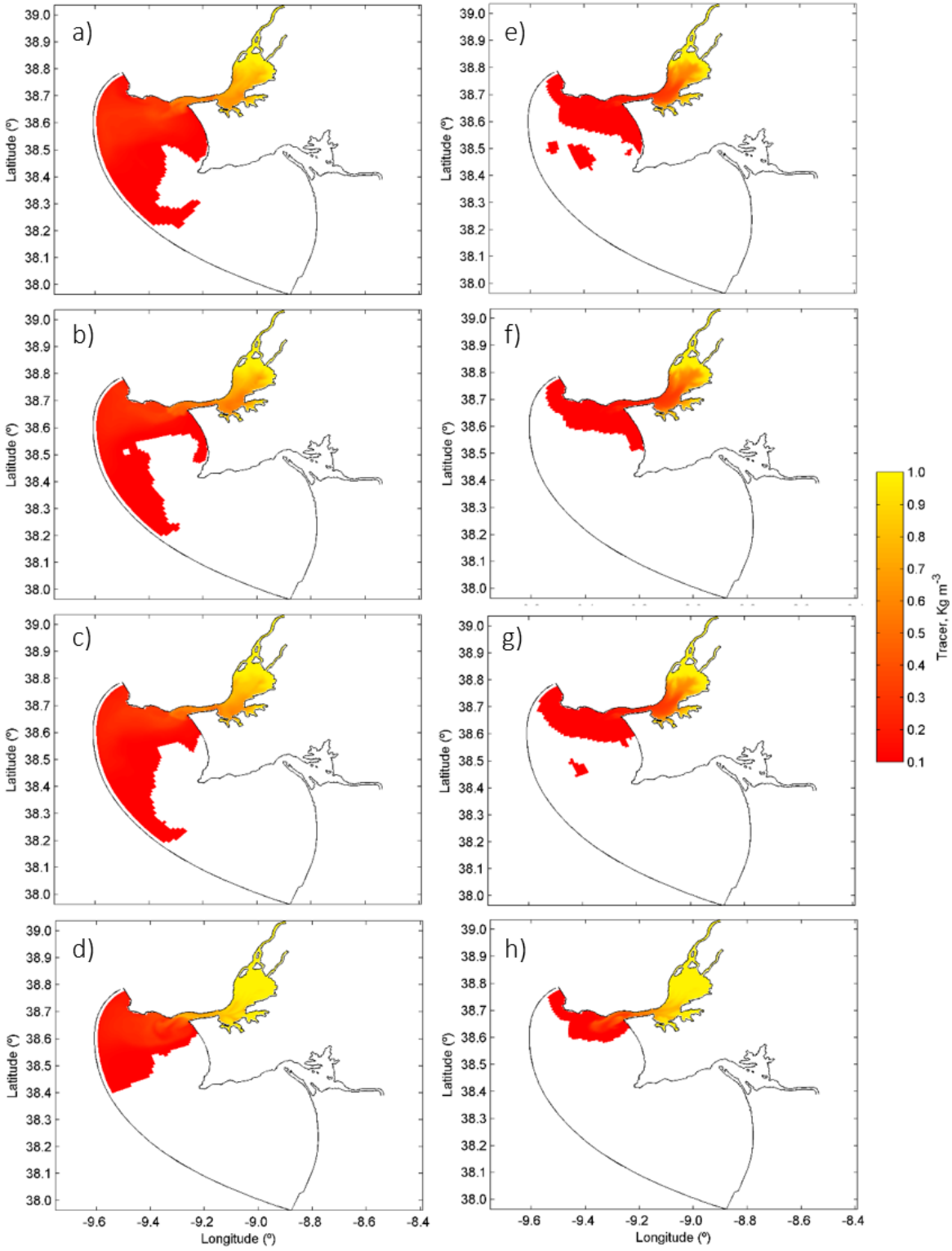

Figure 7.5: Tagus scenarios after 10 days for the surface layer (left) and bottom layer (right), under moderate river discharges of 0.80 non-exceedance probability for southward (a,e), westward (b,f), northward (c,g) winds of 6 m s^{-1} and without wind (d,h) for mesoscale currents.

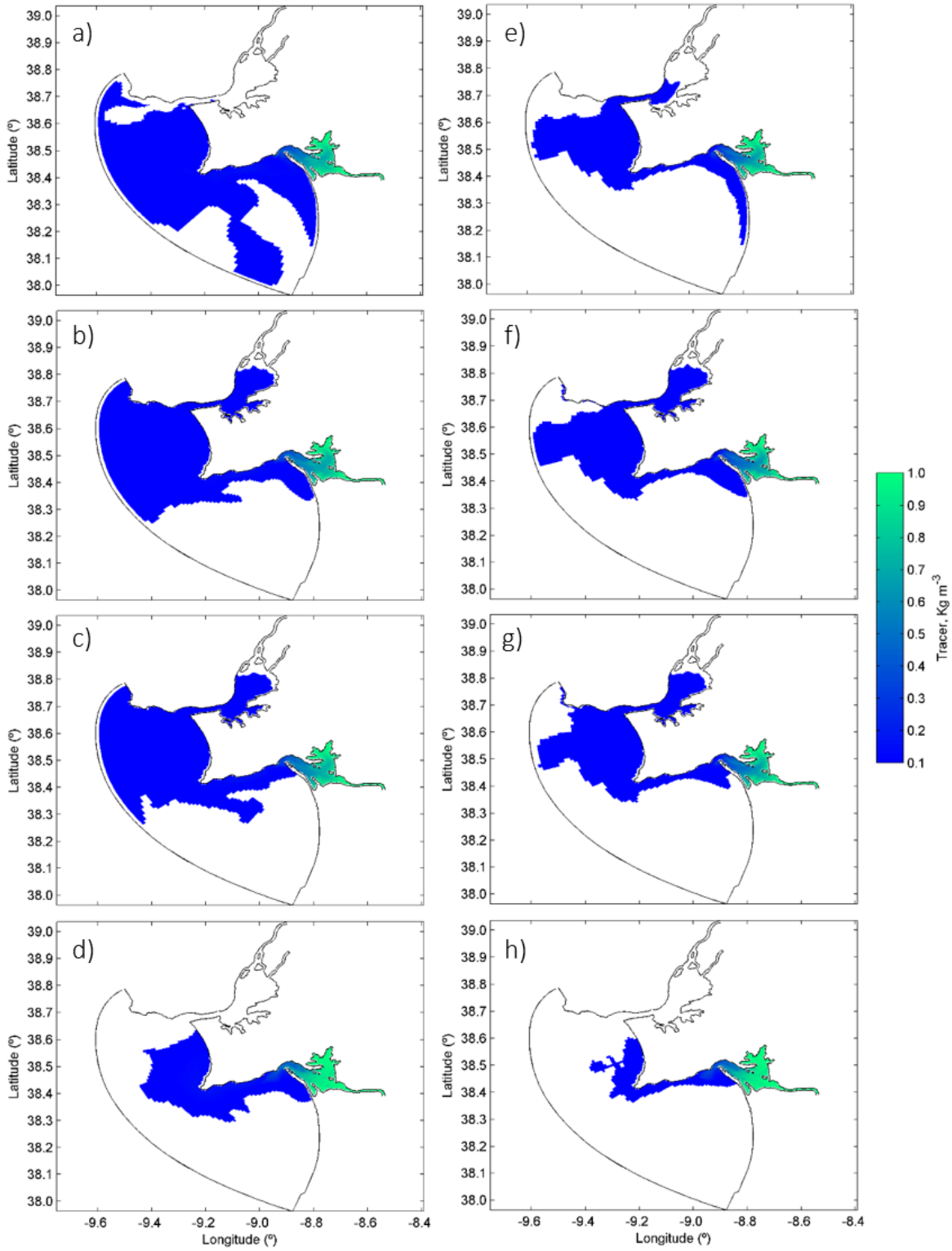

Figure 7.6: Sado scenarios after 10 days for the surface layer (left) and bottom layer (right), under moderate river discharges of 0.80 non-exceedance probability for southward (a,e), westward (b,f), northward (c,g) winds of 6 m s^{-1} and without wind (d,h) for mesoscale currents.

As expected, for moderate river discharges of 0.80 non-exceedance probability, the Tagus estuary plume (Figure 7.5) kept the same pattern as in scenarios with high river discharge, moving offshore and north-northward. However, the plume area drastically decreases when compared to the high discharge scenarios.

During events of southward (Figure 7.6a), westward (Figure 7.6b) and northward (Figure 7.6c) winds, for discharges of 0.80 non-exceedance probability, the Sado estuarine plume propagates to north, near the coastline, and after a 10-day simulation it is also observed its intrusion in Tagus estuary, as for the previous scenarios of 0.95 non-exceedance probability. For the no wind scenario, it is observed the same pattern than with high discharge scenario, but showing a shorter plume area that is confined closed to shoreline.

In Figure 7.6a,e, for southward wind scenario, the Sado estuary plume intrudes in the lower layers. For the westward (Figure 7.6b,f) and northward (Figure 7.6c,g) wind scenario, its more notorious the intrusion of Sado estuary plume in Tagus estuary, in surface and bottom layers, showing the same pattern as shown in high river discharges, but covering a higher area inside the estuary. This can be explained due to the lower freshwater discharges of Tagus, Sorraia and Vale Michões, conferring lower velocities at the surface, allowing the Sado estuarine plume propagate to the inner estuary.

For low river discharges of 0.50 non-exceedance probability, the Tagus estuary plume (Figure 7.7) kept the same pattern as in scenarios with high and moderate river discharge, moving offshore and north-northward. However, the plume area drastically decreases when compared to the previous discharge scenarios.

During events of southward (Figure 7.8a,e), westward (Figure 7.8b,f) and northward (Figure 7.8c,g) winds, for discharges of 0.50 non-exceedance probability, the Sado estuarine plume propagates to north, near the coastline, and after a 10-day simulation it is also observed its intrusion in Tagus estuary. For the no wind scenario, it is observed the same pattern as shown with previous discharge scenario, but showing shorter plume area. The same patterns of moderate discharge scenarios are also observed for low discharge scenarios, with a notorious intrusion of Sado estuary plume in Tagus estuary, in surface and bottom layers, for westward and northward wind scenarios.

These results show that the wind stress and the river discharge are important factors determining the plume propagation to north and are in accordance with the results obtained by Choi and Wilkin (2007) and Sousa et al. (2014a).

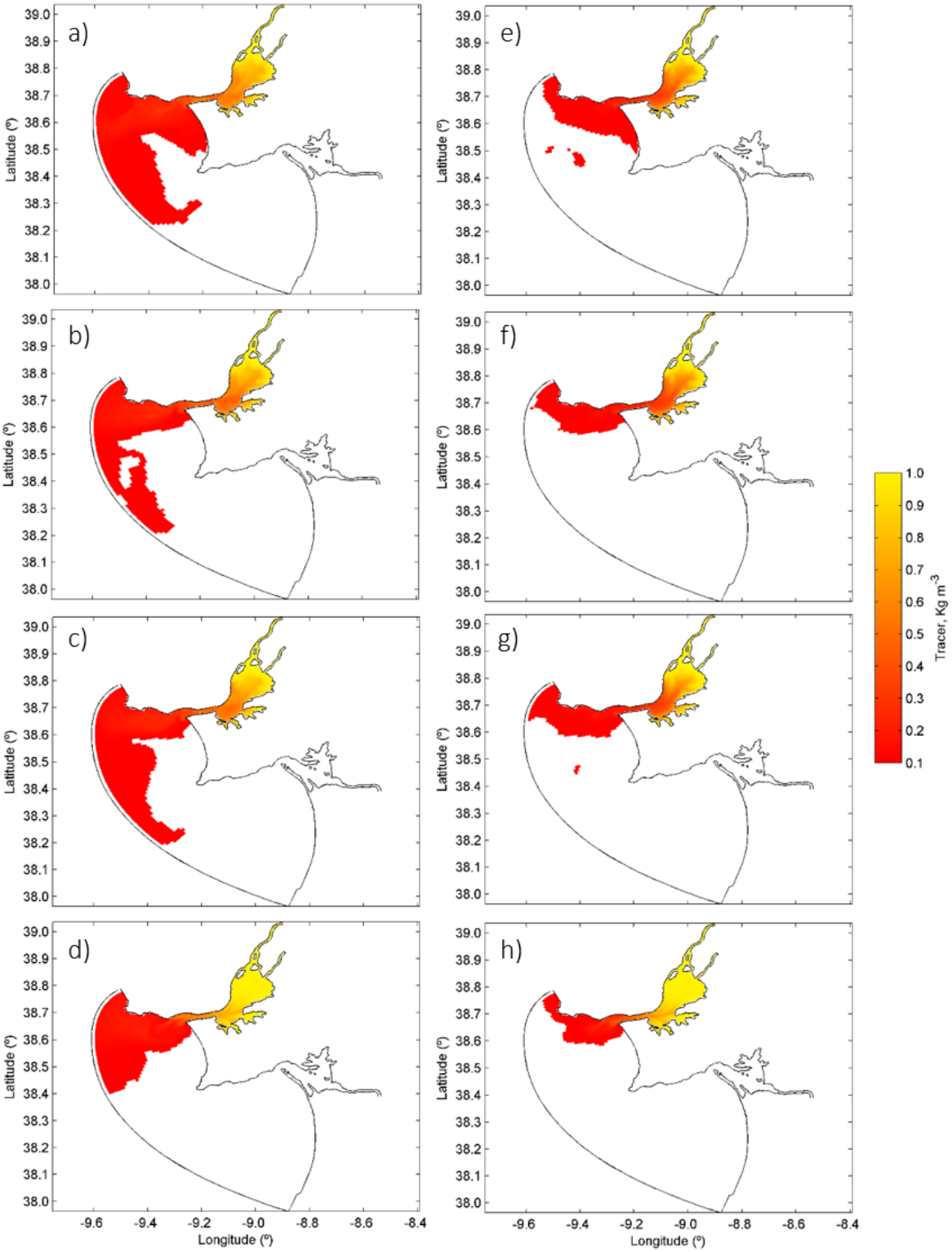

Figure 7.7: Tagus scenarios after 10 days for the surface layer (left) and bottom layer (right), under low river discharges of 0.50 non-exceedance probability for southward (a,e), westward (b,f), northward (c,g) winds of 6 m s^{-1} and without wind (d,h) for mesoscale currents.

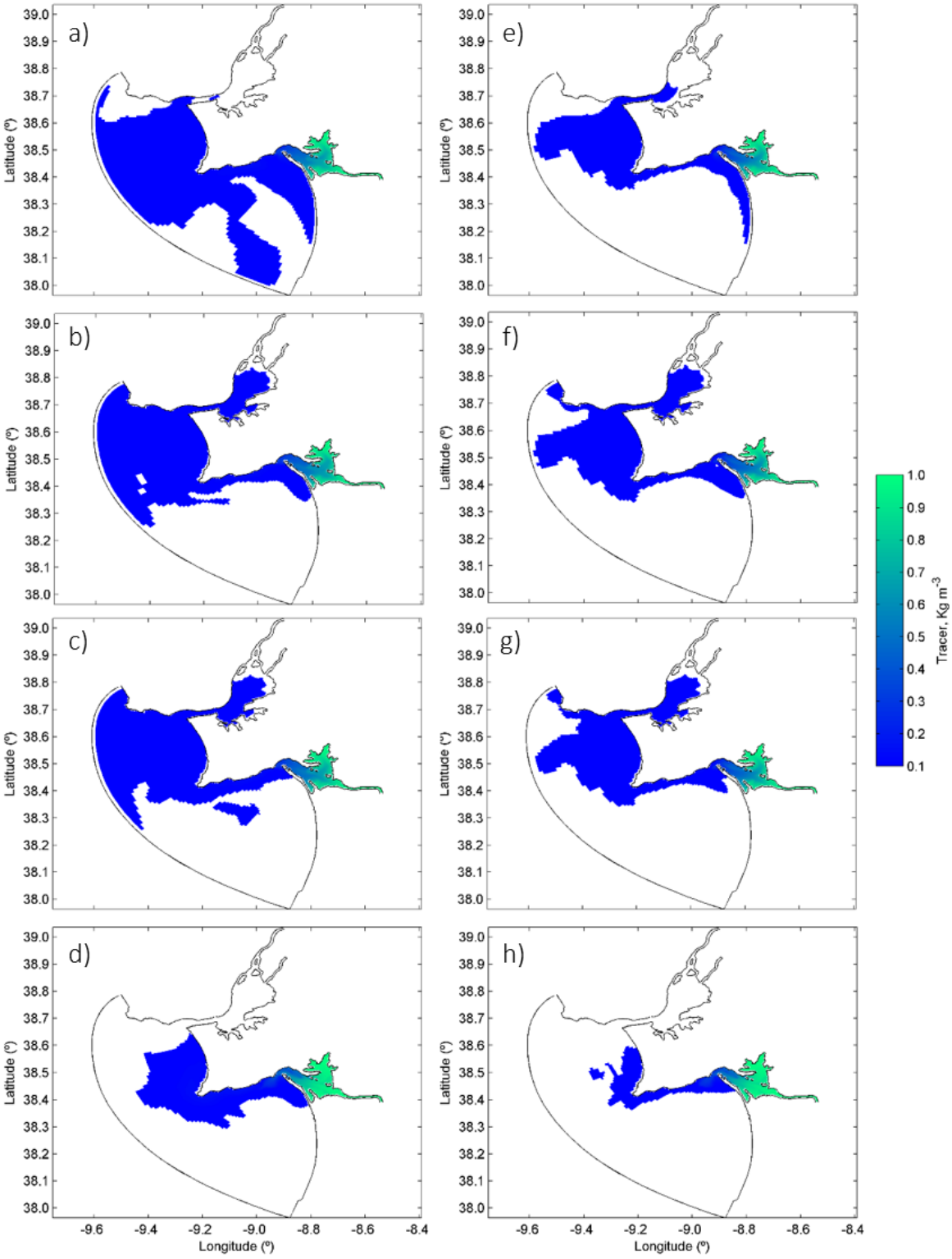

Figure 7.8: Sado scenarios after 10 days for the surface layer (left) and bottom layer (right), under low river discharges of 0.50 non-exceedance probability for southward (a,e), westward (b,f), northward (c,g) winds of 6 m s^{-1} and without wind (d,h) for mesoscale currents.

7.1.2. Coastal dynamics

Horizontal profiles at surface and bottom layer were calculated over the study area, taking into account tracer concentrations between 0 and 1 kg m^{-3} for a better visualization of the dispersion.

Here, the open ocean boundaries will be prescribed with harmonic forcing, excluding the mesoscale current system of the study area. This methodology was applied in previous works (Chao, 1990), aiming to evaluate which factor is the most important, the mesoscale currents or the local dynamics.

Thus, several scenarios with wind stress for the four different directions and without wind, with high discharge of 0.95 non-exceedance probability is applied in 10-days scenarios, obtaining the following Figures for 240 hours after discharge.

Tagus estuarine water scenarios are shown in Figure 7.9, and Sado tracer scenarios in Figure 7.10, for the surface (Figure 7.9 and Figure 7.10 a,b,c,d,e) and bottom (Figure 7.9 and Figure 7.10 f,g,h,i,j) layers.

As it can be observed in Figure 7.9, after 240 hours of high discharge, the Tagus estuarine plume flows out of the estuary and creates a bulge in front of the estuary mouth. A visual analysis of the estuarine plume shows that under every scenario of wind forcing the Tagus plume expands offshore and southward, expanding the bulge in front of the coastal region (Figure 7.9 a, b, c, d), with a larger area impacted on scenarios with southward (Figure 7.9a) and eastward (Figure 7.9d) winds. In absence of wind (Figure 7.9e), it is observable that the Tagus estuarine plume has approximately the same plume area when compared to wind scenarios. However, in all the scenarios of different wind directions and without wind, the Tagus estuarine plume propagates southward without affecting the Sado estuary circulation. On the bottom layer can be observed that the Tagus estuarine water flows offshore, without crossing Espichel cape and being confined at the northern part of the study area, as shown in Figure 7.9f,g,h,i,j.

On the other hand, under southward (Figure 7.10a), westward (Figure 7.10b), northward (Figure 7.10c) and eastward (Figure 7.10d) winds, the Sado estuarine water spreads northward, near the coastline, towards the Tagus estuary, at the surface and bottom layer. However, it is more noticeable the intrusion of Sado estuarine water on the bottom layer.

The wind tend to induce an accumulation of buoyant Sado estuarine water near the Tagus estuary mouth, but at the bottom layer the Sado estuarine water spreads towards the Tagus estuary. With no wind stress, the same pattern appear to occur as wind scenarios.

As observed in Figure 7.10, under 0.95 non-exceedance probability discharges, a plume intrusion is observed in Tagus estuary after a 10-day period.

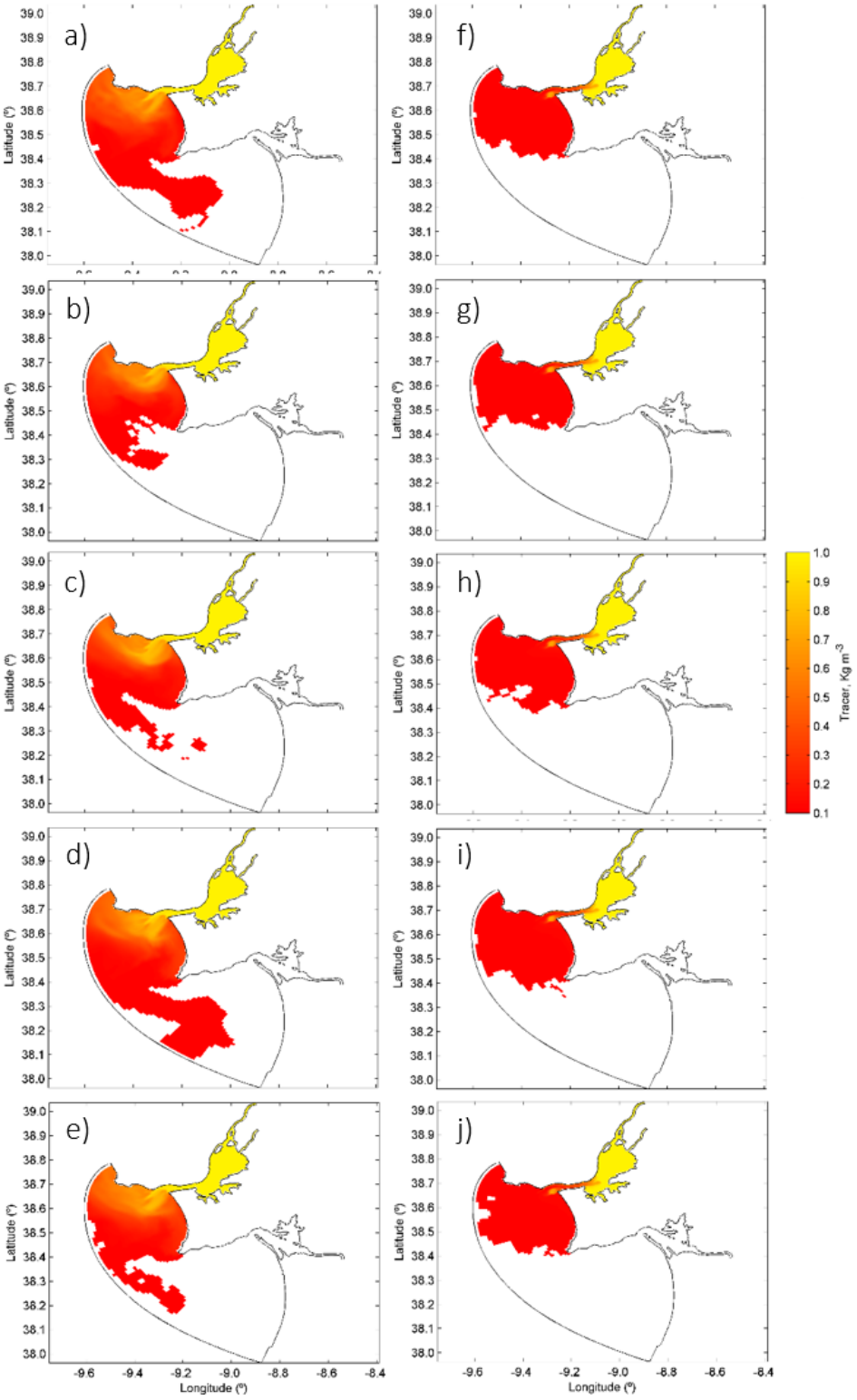

Figure 7.9: Tagus scenarios after 10 days for the surface layer (left) and bottom layer (right), under high river discharges of 0.95 non-exceedance probability for southward (a,f), westward (b,g), northward (c,h), eastward (d,i) winds of 6 m s^{-1} and without wind (e,j) for coastal dynamics.

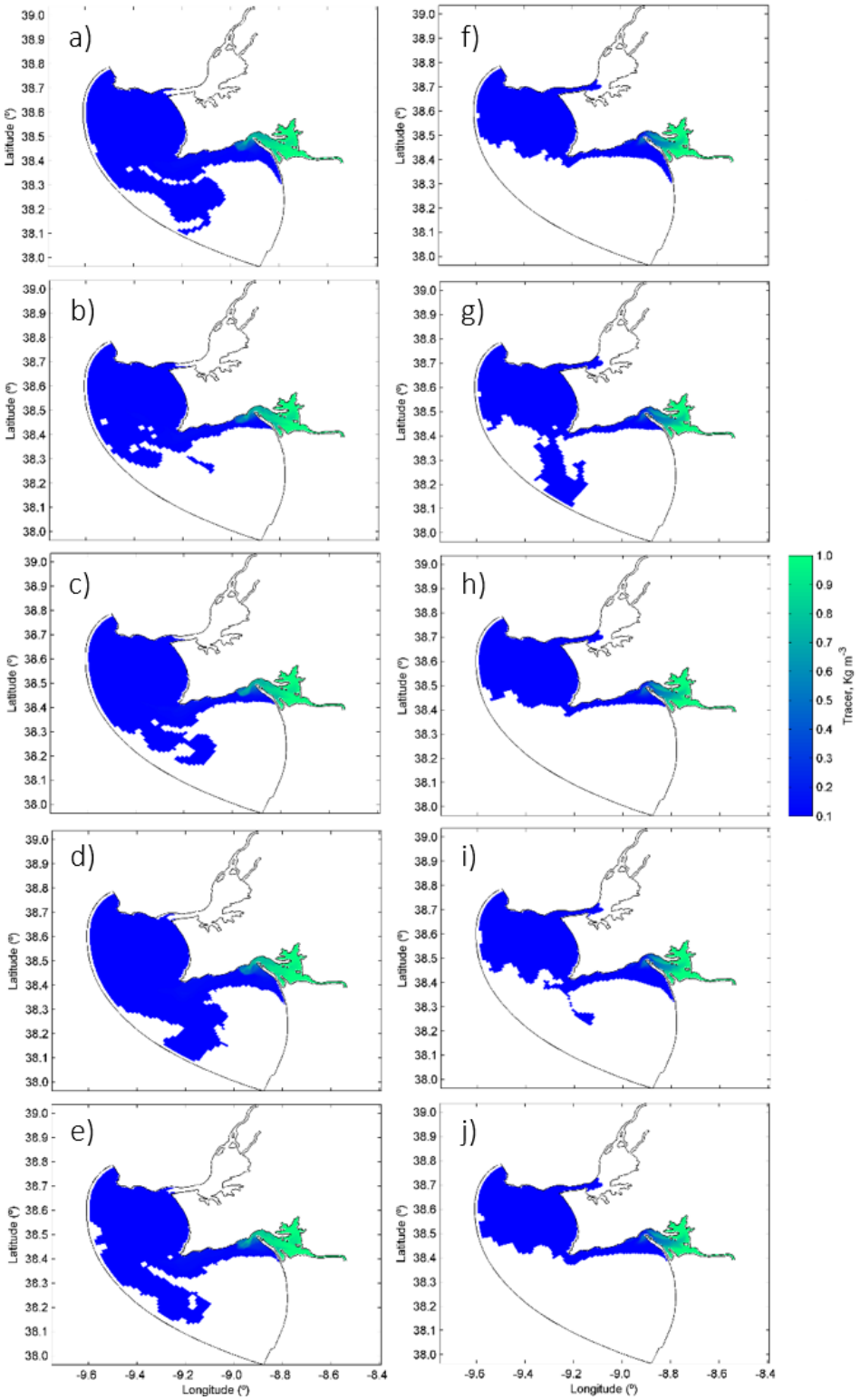

Figure 7.10: Sado scenarios after 10 days for the surface layer (left) and bottom layer (right), under high river discharges of 0.95 non-exceedance probability for southward (a,f), westward (b,g), northward (c,h), eastward (d,i) winds of 6 m s^{-1} and without wind (e,j) for coastal dynamics.

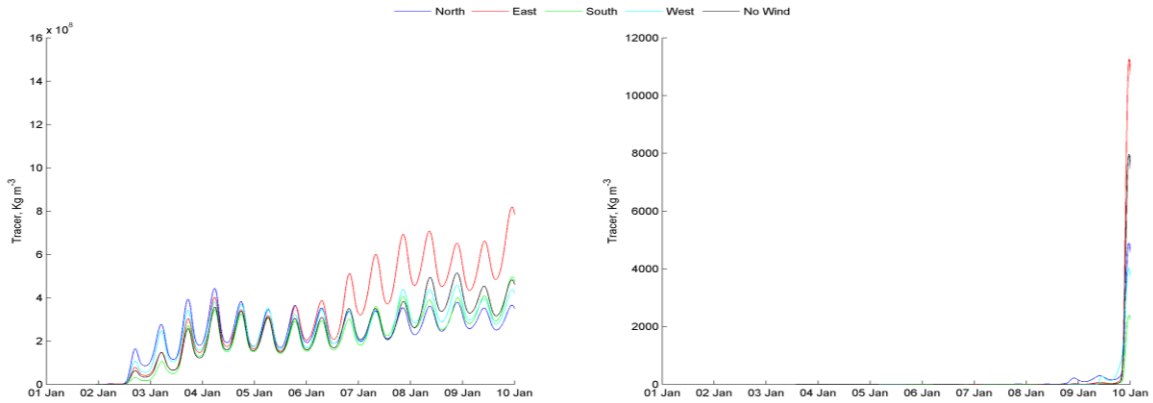

Figure 7.11: Cumulative advective transport of a) Sado tracer in Cross-section II and b) Tagus tracer in Cross-section I, under high river discharges of 0.95 non-exceedance probability for the different wind scenarios.

To observe which scenario most influences the propagation of the Sado plume towards the Tagus estuary, an evaluation of the cumulative advective transport of Tagus and Sado tracer are also reported in cross-sections I and II, respectively. Thus, Figure 7.10a shows the cumulative advective transport of Sado tracer that was registered in cross-section II, and Figure 7.10b the cumulative advective transport of Tagus tracer registered in cross-section I.

Figure 7.11 supports what was previously observed in Figure 7.9 and Figure 7.10. The different wind directions and no wind scenarios, there are an intrusion of the Sado estuarine water in Tagus estuary.

Figure 7.11a also indicates that the Sado tracer arrived at the same moment for all the scenarios at the Tagus estuary, around 36 hours after the run start, characterized by high tracer concentrations of advected Sado tracer up to $8x10^{16}$ kg m^{-3} for westward winds, and around $4.5x10^{16}$ kg m^{-3} for the other scenarios. It is also observed that Sado tracer has almost the same cumulative advected concentration pattern for all the scenarios. This results indicates that in every scenario of wind stress occur the propagation of Sado estuarine water in Tagus estuary.

It can be observed the coastal dynamics on the tracer concentration of Sado estuarine plume as observed for the mesoscale currents scenarios. Figure 7.11b indicates that Tagus tracer in the 10-day scenarios does not propagate to the Sado estuary with concentrations worth analyzing. However, it is evident that on the 10^{th} day some advected estuarine water from Tagus estuary intrudes in Sado estuary.

Stated this, a new set of simulations with discharges of 0.80 (Figure 7.12 and Figure 7.13) and 0.50 (Figure 7.14 and Figure 7.15) non-exceedance probability for northward, westward, southward and eastward winds, and without wind were performed.

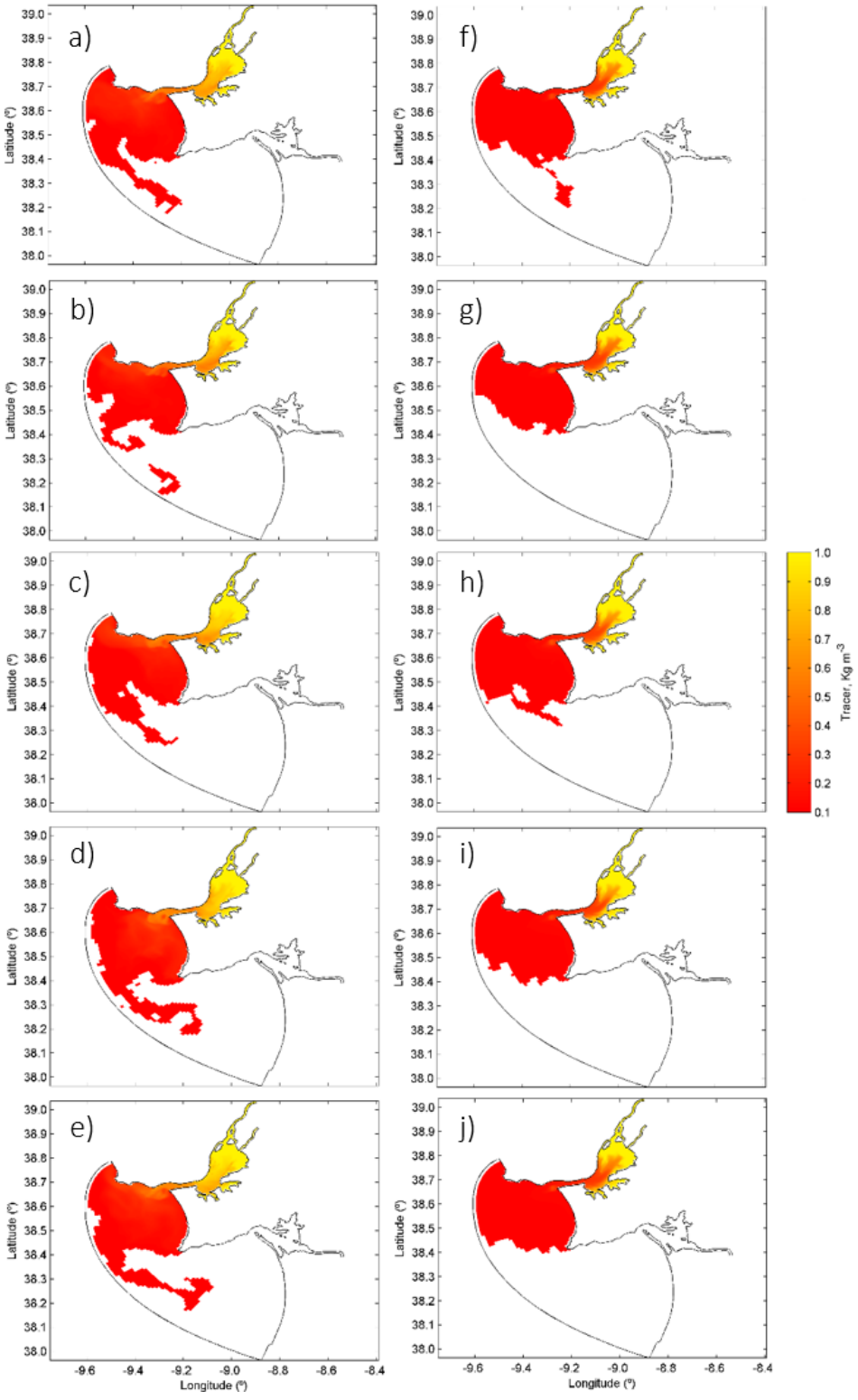

Figure 7.12: Tagus scenarios after 10 days for the surface layer (left) and bottom layer (right), under moderate river discharges of 0.80 non-exceedance probability for southward (a,f), westward (b,g), northward (c,h), eastward (d,i) winds of 6 m s^{-1} and without wind (e,j) for coastal dynamics.

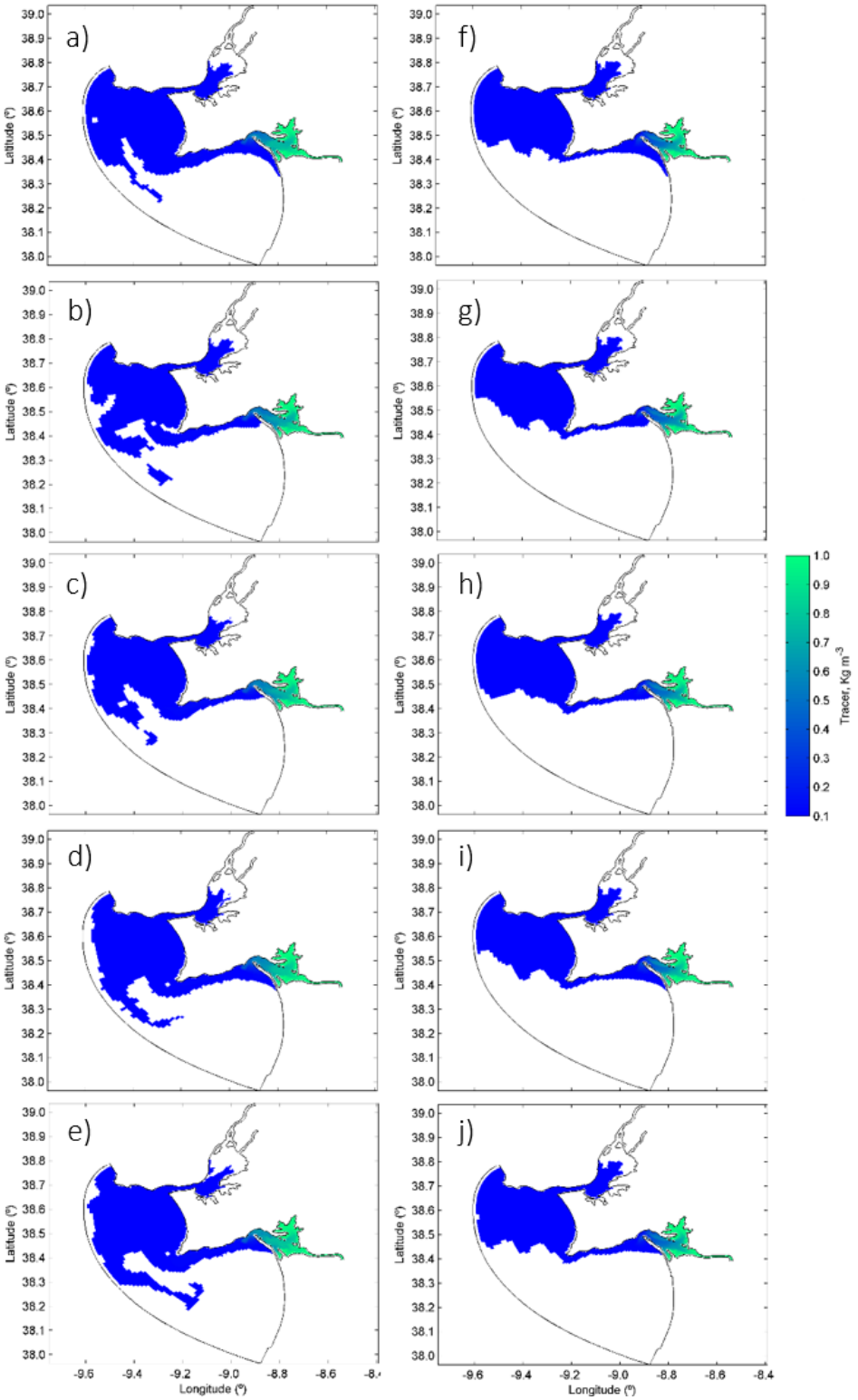

Figure 7.13: Sado scenarios after 10 days for the surface layer (left) and bottom layer (right), under moderate river discharges of 0.80 non-exceedance probability for southward (a,f), westward (b,g), northward (c,h), eastward (d,i) winds of 6 m s^{-1} and without wind (e,j) for coastal dynamics.

As expected, for moderate river discharges of 0.80 and 0.50 non-exceedance probability, the Tagus estuary plume (Figure 7.12 and Figure 7.13, respectively) kept the same pattern as in scenarios with high river discharge, flowing offshore. However, the plume area slightly decreases when compared to the high discharge scenarios.

This pattern is observed also for all wind direction events as well as without wind, for discharges of 0.80 non-exceedance probability. The Sado estuarine plume propagates to the north, confined to the coastline, and after a 10-day simulation is also observed an intrusion of the Sado estuarine water in Tagus estuary. The intrusion of Sado estuarine water in Tagus estuary is more notorious, in both surface and bottom layers, covering a bigger area inside the estuary than in previous scenarios for high discharge.

For low river discharges of 0.50 non-exceedance probability, the Tagus estuary plume (Figure 7.14) kept the same pattern as in scenarios with high and moderate discharge, flowing offshore, and being confined at north of Espichel cape at the bottom layer. However, the plume area is approximately the same when compared to the previous discharge scenarios.

During events of wind and without wind, for discharges of 0.50 non-exceedance probability, the Sado estuarine plume propagates to north, confined to the coastline, and is also observed an intrusion of the Sado estuarine plume in Tagus estuary. The same patterns observed in moderate discharge scenarios are also observed for low discharge scenarios, with a notorious intrusion of the Sado estuarine water in Tagus estuary, in surface and bottom layers for all the wind and no wind scenarios.

These results show that the wind stress and the river discharge are factors determining the plume propagation, due to the similar propagation pattern at the surface for all the scenarios.

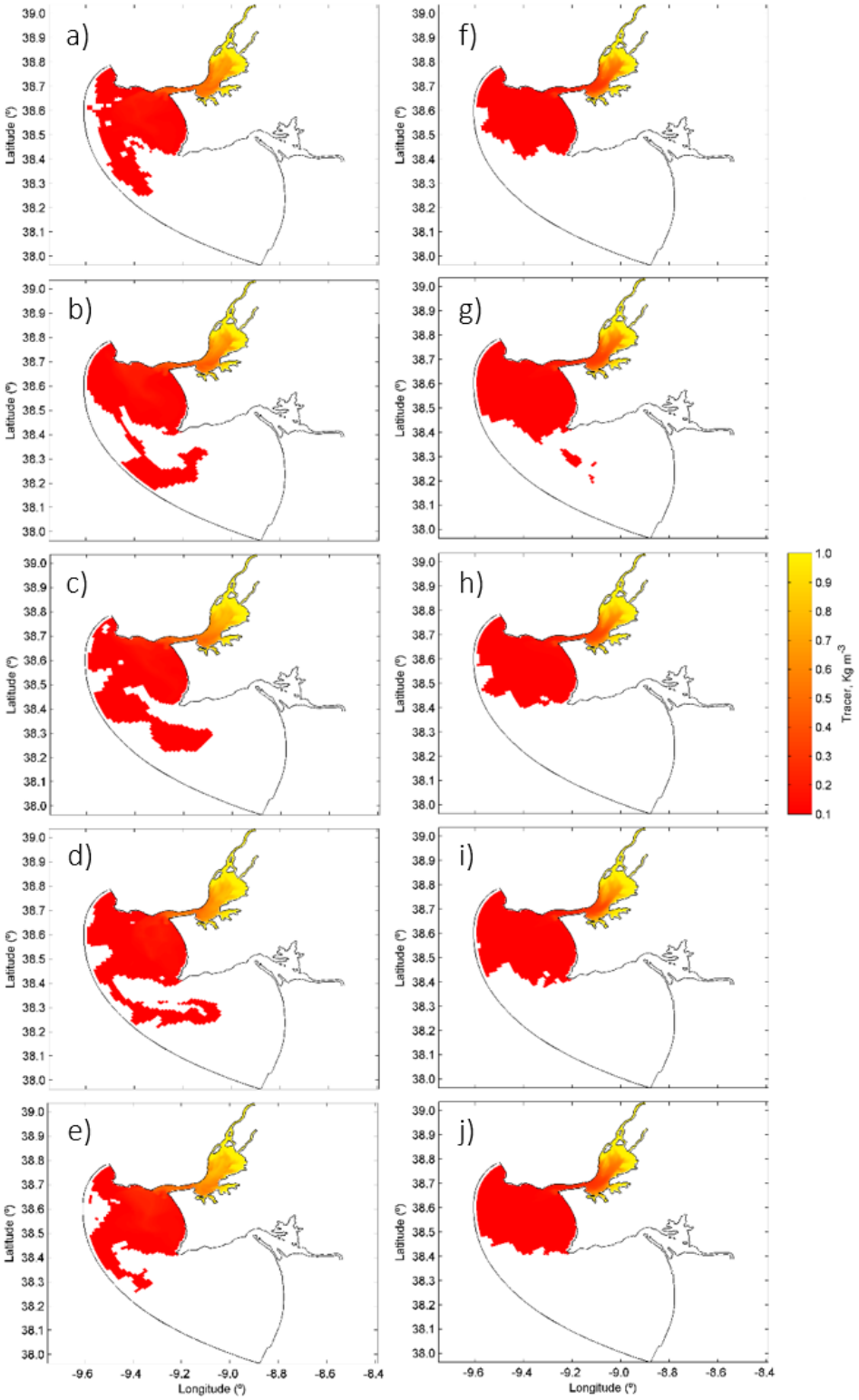

Figure 7.14: Tagus scenarios after 10 days for the surface layer (left) and bottom layer (right), under low river discharges of 0.50 non-exceedance probability for southward (a,f), westward (b,g), northward (c,h), eastward (d,i) winds of 6 m s^{-1} and without wind (e,j) for coastal dynamics.

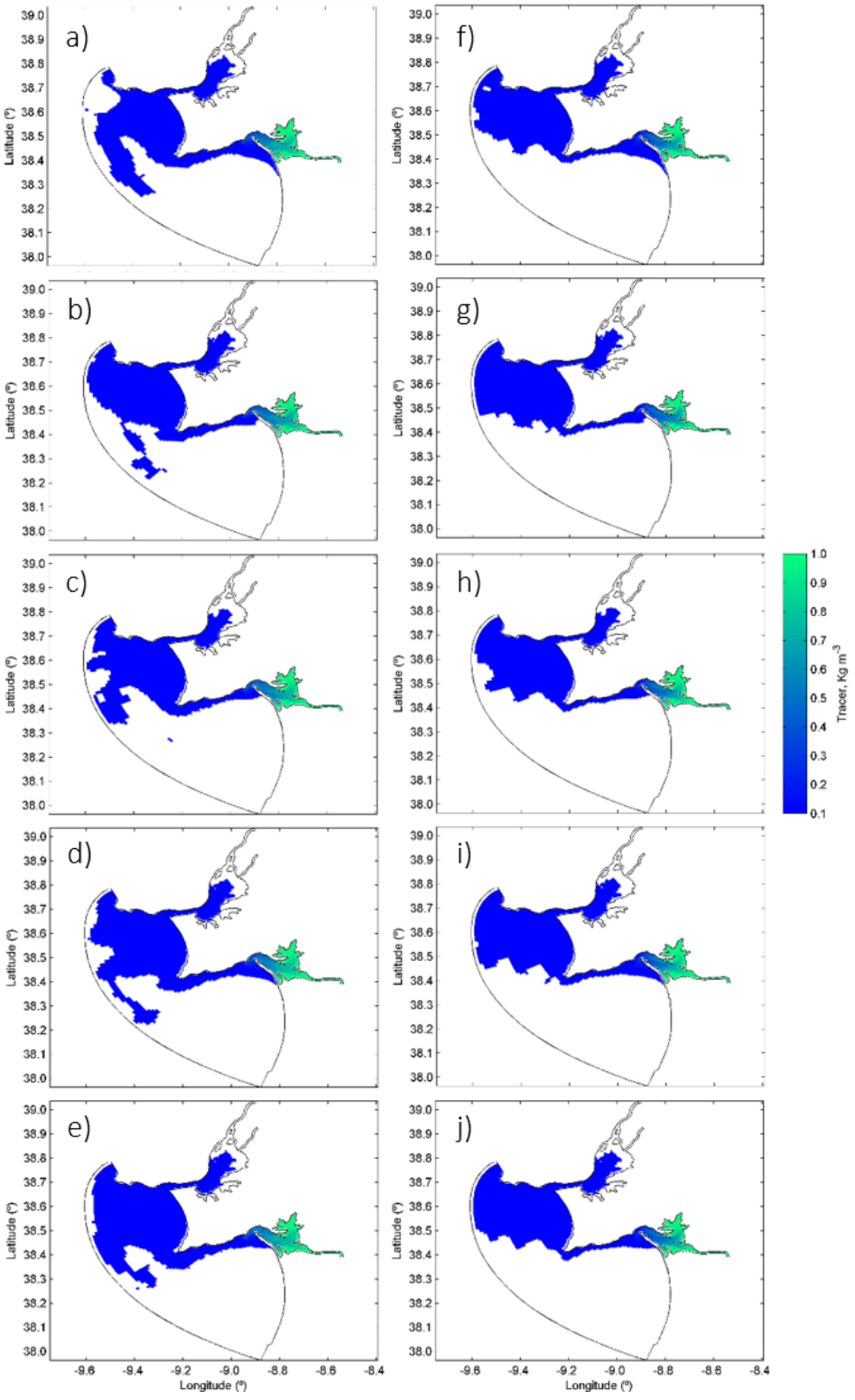

Figure 7.15: Sado scenarios after 10 days for the surface layer (left) and bottom layer (right), under low river discharges of 0.50 non-exceedance probability for southward (a,f), westward (b,g), northward (c,h), eastward (d,i) winds of 6 m s^{-1} and without wind (e,j) for coastal dynamics.

7.1.3. Comparison

Both Riemann and harmonic forcing at open ocean boundaries led to a propagation of the estuarine plumes. In Riemann scenarios, which contain the mesoscale current system of the study area, led to a propagation with a northern pattern direction, confined to coastline for Sado estuary plume. This can be observed in the no wind scenarios, where the absence of the bulge distortion is notorious when compared with the wind scenarios.

In mesoscale current scenarios (Section 7.1.1), it can be observed that the wind direction tend to increase the surface plume size and distort the bulge shape in the wind direction. In scenarios with westward wind, freshwater is exported from the estuaries and favours its accumulation in the recirculating bulge outside the mouth of Tagus and Sado estuary. When the river discharge decreases, the patterns are similar to the previous scenarios, only with differences in the plume influence area, being smaller with lower discharges when compared the high discharge.

For the Harmonic forcing scenarios, which contains the coastal dynamic system (Section 7.1.2), generally it can be observed that the wind direction does not influence much the buoyancy of the estuarine plumes, the plume propagation in all the scenarios show a similar pattern: moving to north and slightly to west, near the coastline.

This result can be explained through the imposed forcing at the open ocean boundaries, the Riemann forcing considers the mesoscale current system, whereas harmonic forcing only consider the coastal dynamics. The analysis of the scenarios with mesoscale currents leads to the conclusion that the predominant currents at the surface and bottom layers in the study area have a northward direction. These results show that the wind stress and the river discharge are important factors determining the plume propagation.

The results for harmonic forcing at the open ocean boundaries, shows that the wind and the river discharge are factors determining the plume propagation, but not the only primary factors, due to the similar propagation pattern at the surface for all the scenarios, leading to the conclusion that the coastal current is also important in the buoyancy of the plume.

These conclusions are reinforced by the analysis of Figure 7.4 and Figure 7.11. In Figure 7.4 can be observed the intrusion of the Sado estuarine water in Tagus estuary in all the scenarios of different wind directions and with no wind, although with different hours of the intrusion and different cumulative advective concentrations during the 10-day scenario. As for Figure 7.11, it can be observed the intrusion of Sado estuarine water in Tagus estuary in all the scenarios of different wind directions and without wind. Figure 7.11a also indicates that Sado tracer arrived at the same moment at the Tagus estuary, around 36 hours after the run start, regardless of wind stress.

Stated this, the most important factor for the buoyancy of the estuarine plume is the current system, associated with the high discharges and wind direction. When the currents were neglected in Harmonic forcing, the Sado plume took less than half of the time to intrude in Tagus estuary, maintaining the same cumulative advected concentration to the interior of Tagus during the 10-day scenarios. As for Riemann forcing, the intrusion took around 120 h to occur, and with different times of intrusion and different cumulative advected concentration to the interior of Tagus during the 10-day scenarios, depending in the wind direction.

7.2. Tracer application

7.2.1. Estuarine intrusion

As observed in Section 7.1.1 and Section 7.1.2, in several scenarios the intrusion of Sado estuarine plume was more evident on the bottom layers than at surface layer. This results occurred in the presence of southward and eastward winds, and for an overview of how the tracer intruded in Tagus estuary a new set of figures were done, with the following characteristics: 1) 240 hours after the simulation start, on the 10^{th} and last day, same as the horizontal profiles observed in Sections 7.1.1 and 7.1.2) the vertical profiles are located on the cross-section, in the cell located in the middle of the mouth; 3) the left panel show the cumulative advected tracer of Tagus, flowing outside the estuary to the ocean; 4) the right panel show the cumulative advected tracer of Sado, flowing inside the Tagus estuary; 5) The top panels (Figure 7.16a,b,e,f) are scenarios for Riemann forcing and the bottom panels (Figure 7.16c,d,g,h) are scenarios for harmonic forcing; 6) Figure 7.16a,c,e,g shows the southward winds, and Figure 7.16b,f,d,h the northward winds.

From Figure 7.16 can be observed that the Sado estuarine tracer flows on the bottom layers towards Tagus estuary, whereas Tagus estuarine tracer flows on the top layers outside the estuary.

This can be explained due to the Tagus tracer, flowing from the Tagus, Sorraia and Vale Michões tributaries. The freshwater is less dense and warmer than the oceanic water, including the Sado estuarine water mass, which at this point, their properties are more alike to those found in ocean.

These results show that the intrusion of Sado estuarine water occurs always in the bottom layers, however with low concentrations of cumulative advected estuarine waters.

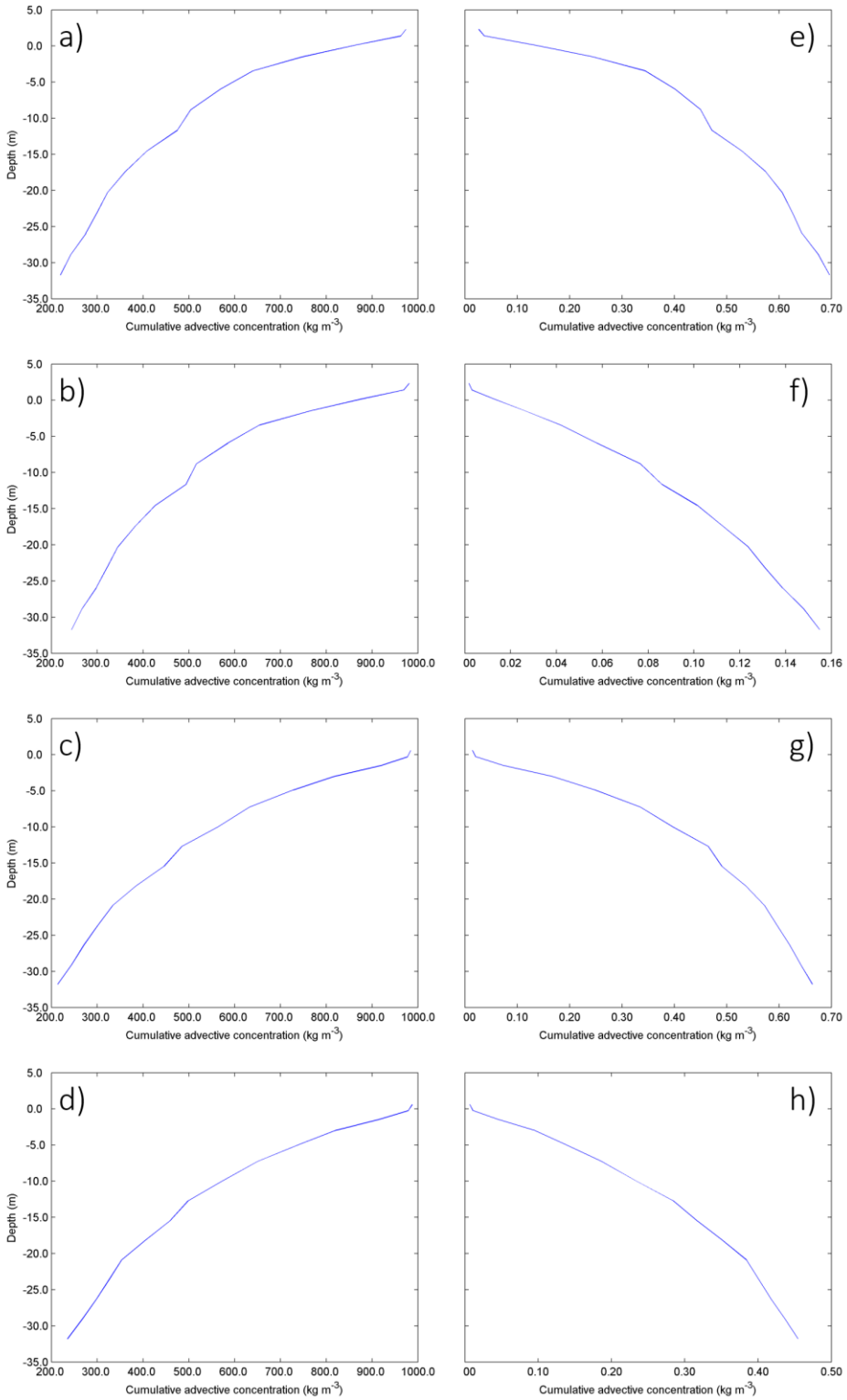

Figure 7.16: Vertical profile of cumulative advective transport of Tagus tracer (left) and Sado tracer (right) in Cross-section II, for 240 h after the simulation start. Under high river discharges of 0.95 non-exceedance probability for the different scenarios of North (a,c,e,g) and West (b,d,f,h) for Riemann forcing (top 4 panels) and harmonic forcing (bottom 4 panels).

7.2.2. Propagation pattern

Surface horizontal profiles at the surface layer were calculated over the study area, for 10-day simulations. Five moments in time were chosen, for which the propagation area is presented:

- The Tagus estuarine water is represented by the Tagus tracer, and the Sado estuarine water is represented by the Sado tracer;
- 24 hours after the simulation start, with intervals of 48 hours until the final moment at 216 hours;
- The figures are displayed with five rows, for each of the wind and no wind scenarios. Also with three columns, one for each discharge of 0.95, 0.80 and 0.50 non-exceedance probability;
- The pattern of the tracer propagation is shown for mesoscale currents (Figure 7.17 and Figure 7.18) and for coastal dynamics (Figure 7.19 and Figure 7.20).

Figure 7.17 shows the Tagus tracer propagation for the different wind directions and no wind scenarios, and for the different discharges. For the high discharge (Figure 7.17a,b,c,d,e), when compared to the other scenarios of moderate and low discharge, its observable that the tracer area is higher, and extends to south. For winds from north and west, after 216 hours, the tracer occupies almost all the study area, except the region near Sado estuary mouth. On the other, scenarios of moderate and low discharge the tracer area tends to decrease as soon as the discharge decreases too. When the wind blows from north (Figure 7.17a), the Tagus tracer propagates to south, and the opposite occur when the wind blow from south (Figure 7.17c). The same pattern can be observed in Figure 7.17b, when the wind blow from east, the Tagus tracer tends to move to west, and with winds blowing from west the Tagus tracer tends to move to coastline (Figure 7.17d). In absence of wind, the Tagus tracer tends to propagate in a north-northwest direction, where, with the increase of freshwater input, the presence of Tagus tracer area increases forming a bulge in front of Tagus estuary mouth.

Figure 7.18 shows the Sado tracer propagation for the different wind and no wind scenarios, under high, moderate and low discharges. A pattern is observed, with high river discharge the tracer area is also bigger, tending to propagate to north, near the coastline with the influence of the different wind directions. In absence of wind (Figure 7.18e,i,m), the tracer maintain the propagation pattern near the coastline, however, tend to create a bulge near the Espichel Cape, with a tendency to propagate to north. As discussed before, with moderate and low discharges, it is more notorious the Sado tracer intrusion in Tagus estuary, when compared with high discharge scenarios (Figure 7.18 for East and South wind).

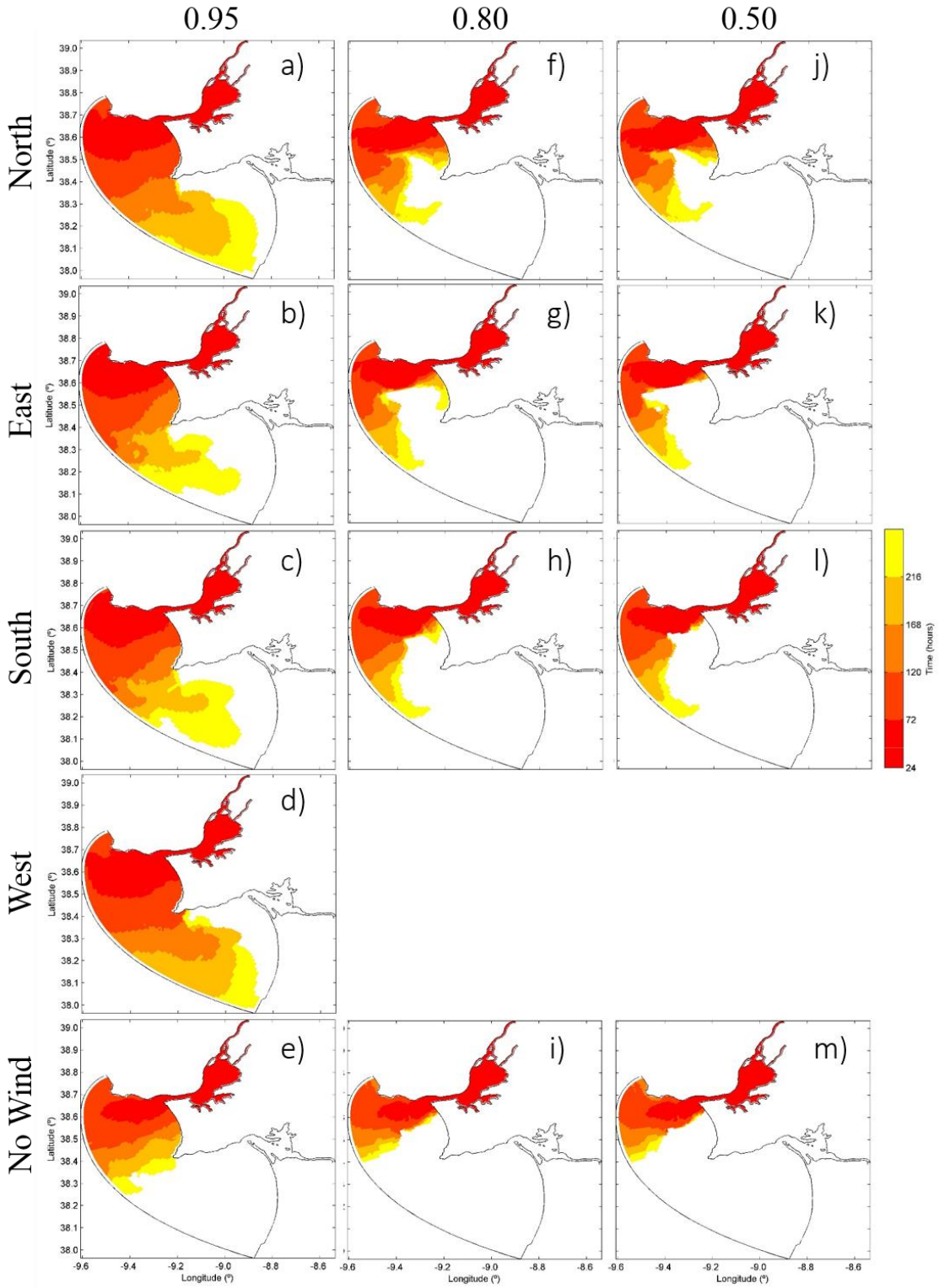

Figure 7.17: Tagus scenarios for the 10-day simulation under discharges of 0.95, 0.80 and 0.50 non-exceedance probability for the surface layer, with Riemann forcing.

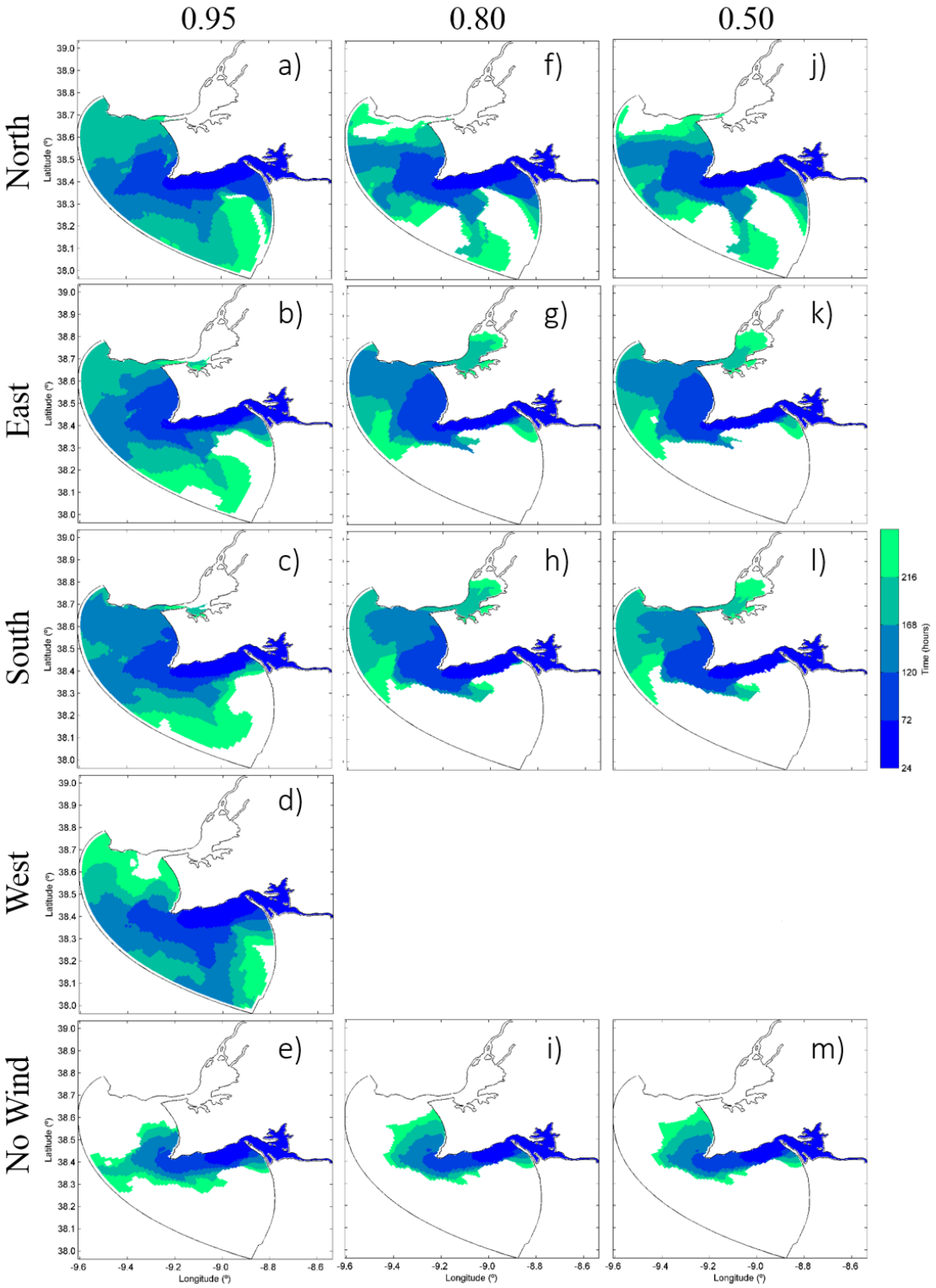

Figure 7.18: Sado scenarios for the 10-day simulation under discharges of 0.95, 0.80 and 0.50 non-exceedance probability for the surface layer, with Riemann forcing.

For the coastal current scenarios, Figure 7.19 shows the Tagus tracer propagation for the different wind and no wind scenarios, and for the different discharges. For the high discharge (Figure 7.19a,b,c,d,e), when compared to the other scenarios of moderate and low discharge, its observable that the tracer area is slightly higher, tending to create filaments that extend to south, forming large scale eddie at south of Espichel Cape, as shown in Figure 7.19 for winds blowing from East and West. The filaments can be an evidence that offshore tidal current is at its highest strength, and force the tracer to travel against the wind, leading to a formation of the filaments and the large scale eddies. Iglesias et al. (2014) observed the same formations under these conditions of wind stress. In summary, for all the wind and no wind scenarios, after 216 hours, the tracer occupies all the north region of the study area, with the exception of the filaments.

Figure 7.20 shows the Sado tracer propagation for the different wind and no wind scenarios, under high, moderate and low discharges. The Sado tracer tends to propagate to north, near the coastline with the influence of the different wind directions, creating a bulge near the Tagus estuary mouth, with a tendency to propagate to north-northwest. A similar pattern can be observed for high, moderate and low river discharge: the tracer occupies the same area for the whole period, and just after 24 hours of the simulation start, the majority of this area is already occupied (Figure 7.20-deep blue). Even with the different wind directions and without wind, the tracer area maintains the same size, with some filaments formed after 168 and 216 hours in south direction, the same pattern observed in Tagus tracer filaments.

All the scenarios show an intrusion of the Sado tracer in Tagus estuary in the next 48 hours, leading to the conclusion that the coastal dynamics are an important factor for the propagation of the Sado estuarine water.

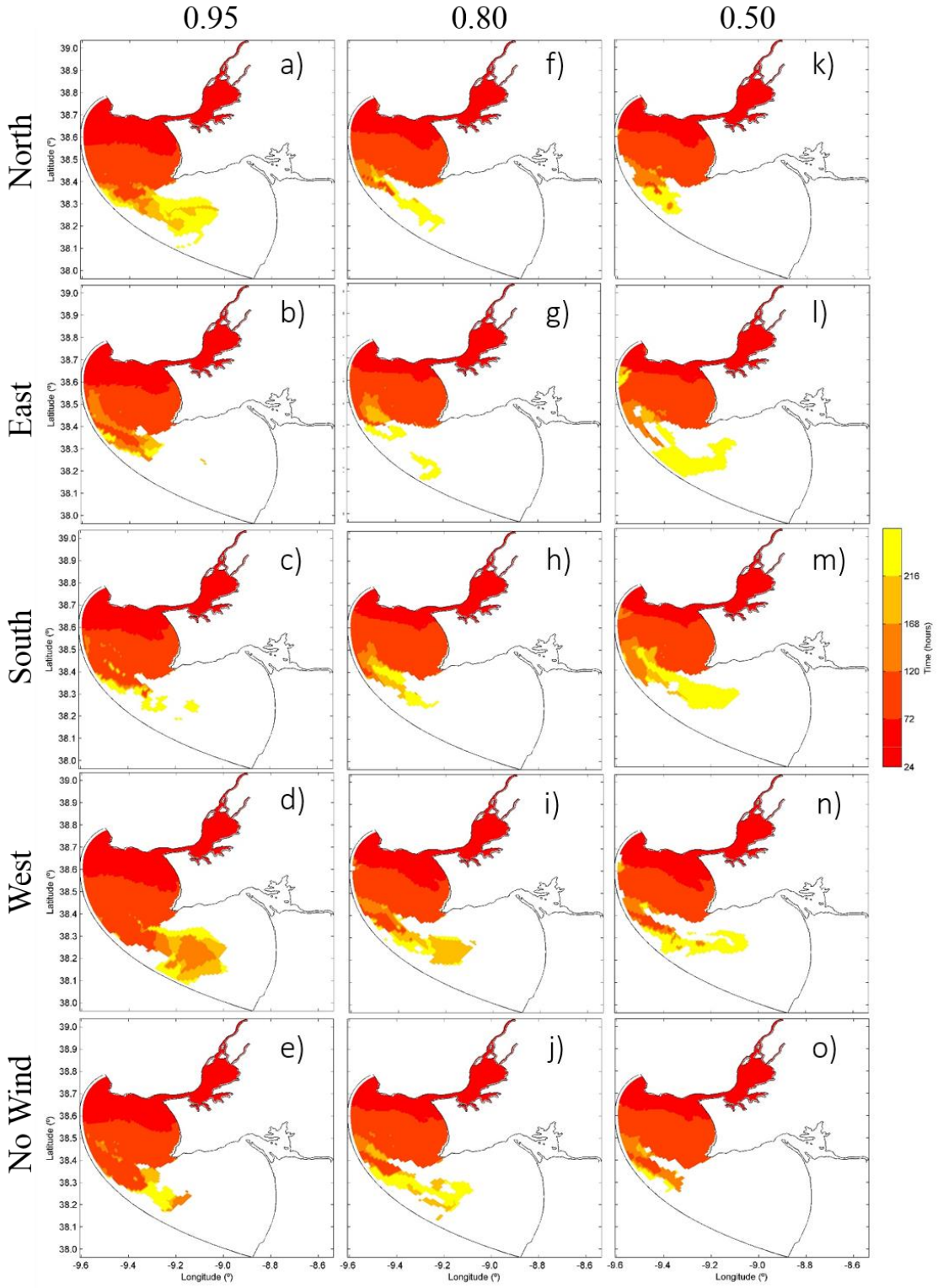

Figure 7.19: Tagus scenarios for the 10-day simulation under discharges of 0.95, 0.80 and 0.50 non-exceedance probability for the surface layer, with Harmonic forcing.

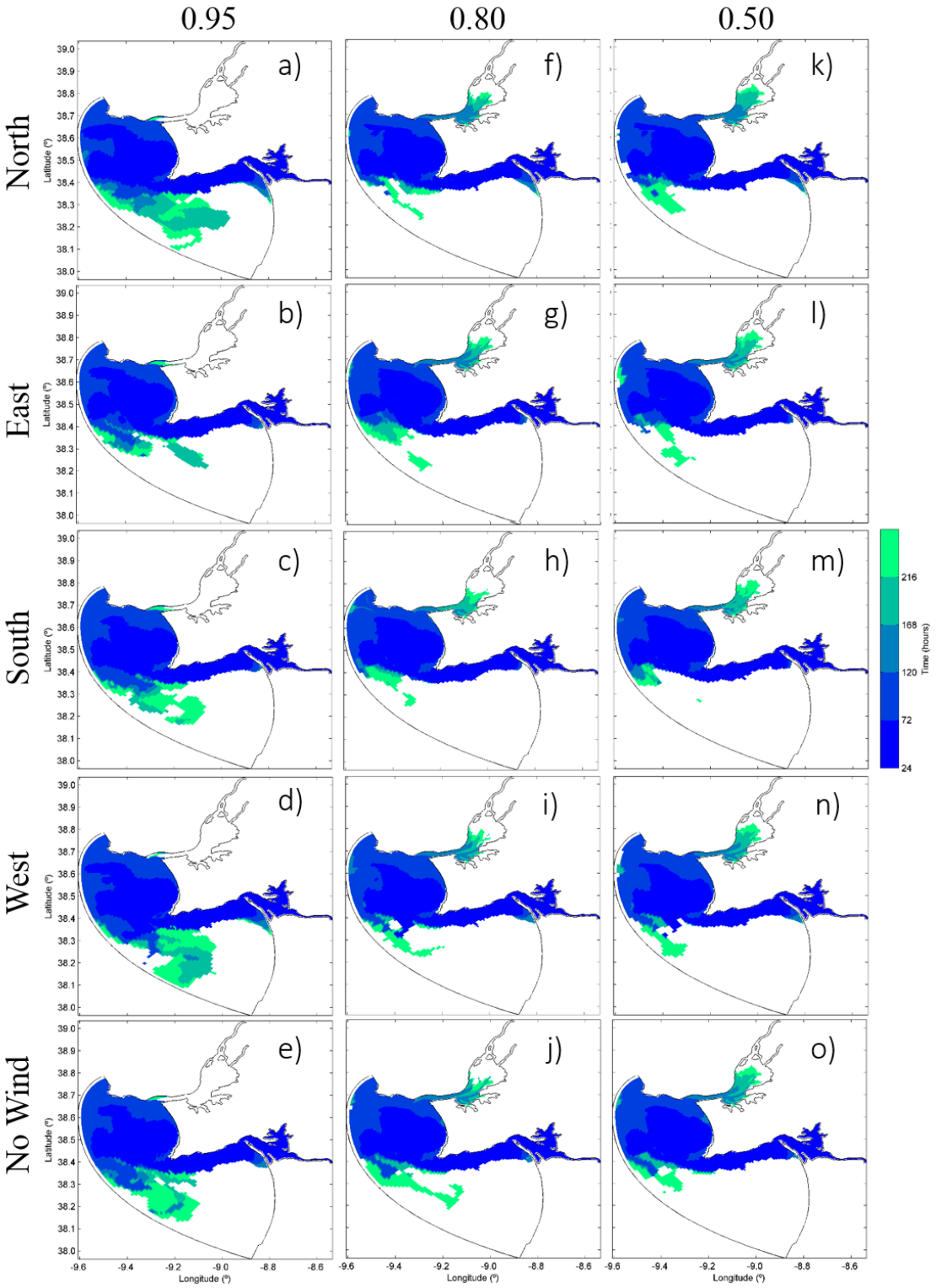

Figure 7.20: Sado scenarios for the 10-day simulation under discharges of 0.95, 0.80 and 0.50 non-exceedance probability for the surface layer, with Harmonic forcing.

8. Conclusions

Tagus and Sado estuaries have different characteristics with various studies using numerical models, focusing on the investigation of the complex circulation of the Tagus or the Sado estuaries, but the interaction between these two systems was never taken into account. Thus, the presented study contemplate both Tagus and Sado estuaries as one system. This model implementation has the ability to show plume interaction patterns over shelf and water intrusions from the neighbor river.

The results of this work as well the methodologies developed are adaptations of other studies with other numerical models, however this study proved that this methodology using Delft3D can be applied in similar studies in other estuaries. The three-dimensional hydrodynamic model Delft3D-Flow was successfully calibrated and applied to Tagus and Sado estuaries and nearby coastal region. Overall all the aims established at the beginning of this work were accomplished.

The Tagus and Sado estuarine water masses structure varies with the different river discharges imposed to the model. It was investigated the effect of different river discharges of 0.95, 0.80 and 0.50 non-exceedance probability on the propagation of the estuarine water masses over the adjacent continental shelf, for two different forcing's at open boundaries: Riemann and harmonic forcing.

The results for the simulations with mesoscale currents with an extreme discharge of 0.95 non-exceedance probability suggest an intrusion of the estuarine water of the Sado in the Tagus estuary in all the scenarios of different wind directions, still was observed the same for the absence of wind. The Sado estuarine water arrived at different moments at the Tagus estuary, taking less time with northward winds, around 120 hours after the run start, following by westward winds, around 126 hours, characterized by high concentrations of advected Sado tracer. At the end of 5^{th} day with southward and no wind scenarios, the Sado estuarine water intruded in Tagus estuary, having a maximum. For the eastward wind scenario, the Sado estuarine water took longer than the other scenarios, only after 144 hours was observable, and kept low concentration of advected tracer. This indicates that eastward winds are not favorable for the Sado estuary water mass propagation with mesoscale currents.

For river discharges of 0.80 and 0.50 non-exceedance probability, the Tagus estuary water kept the same pattern as in scenarios with high river discharge, moving to offshore and north-northwest. However, the tracer area drastically decreases when compared to the high discharge scenarios.

The results with coastal dynamics, for extreme discharge of 0.95 non-exceedance probability suggest an intrusion of the estuarine water of the Sado in the Tagus estuary in all the scenarios of

different wind directions and no wind. The Sado estuarine water arrived at the same moment at the Tagus estuary, around 36 hours after the run start, characterized by high concentrations of advected Sado tracer.

For moderate river discharges of 0.80 and 0.50 non-exceedance probability, the Tagus estuary tracer kept the same pattern as in scenarios with high river discharge, flowing to offshore. However, the tracer area slightly decreases when compared to the high discharge scenarios.

The most important factor for the buoyancy of the estuarine water is the current system, associated with the high discharge and wind direction. Also, can be concluded that Sado estuarine water flows on the bottom layers towards Tagus estuary, whereas Tagus estuarine water flows on the top layers outside the estuary. This can be partly explained by the research of Fujiwara et al.(1997) , which observed that in large estuaries and ROFIs (Simpson, 1997) the fate of the density field is controlled not only by buoyancy and tidal forcing but also by the system's morphology.

It was observable that the estuarine water masses tend to create filaments that extend to south, forming mesoscale eddies at south. The Sado estuarine water tends to propagate to north, near the coastline with the influence of the different wind directions, creating a bulge near the Tagus estuary mouth, with a tendency to propagate to north-northwest.

The distinctive feature of all ROFI systems is the input of significant amounts of buoyancy as freshwater from river sources. If the spatial scale is unrestricted by coastal topography and stirring is weak, this input tends to drive a coast-parallel flow in which the Coriolis force constrains a wedge of low density water against the coastal boundary. Without frictional effects, this flow is subject to baroclinic instability, which induces large meanders and eddies in the flow, as observed in most of the scenarios.

The scenarios were marked with freshwater variability supply and subjected to a wide range of tidal stirring constituted a good observational testing for the theories of buoyancy-stirring interaction and the control of exchange characteristics of estuaries and ROFIs (Simpson, 1997). On global scale it is clear that ROFIs represent an important component of the shelf-sea environment of particular concern in relation to the impact of pollutant discharges, the same methodology applied this study.

Future research should be performed to apply the same methodology used in this present work for summer season. This methodology can also be applied to evaluate and monitoring environmental hazards such as oil spills or other pollutants. The present model setup is ready to incorporate the water quality parameters, such as biological characteristics and perform a deeper investigation with the estuarine water masses in the sense of biogeochemical approach. The model can also be extended offshore and north, covering a larger area that will allow the investigation of

the propagation of Tagus and Sado estuarine water masses in the Portuguese coast. This extension of the model grid can be done considering the data availability, for both bathymetry and open boundaries forcing, and it would be a good increment to the study of the estuarine water masses of Tagus and Sado.

References

Ambar, I., Fiuza, A., 1994. Some features of the Portugual Current System: A poleward slope undercurrent, an upwelling related southward flow and an autumn-winter poleward coastal surface current, 2nd International Conference on Air-Sea Interaction & on Meterologoy & Oceanography of 286–287.

Anderson, D.M., Keafer, B. a., Geyer, W.R., Signell, R.P., Loder, T.C., 2005. Toxic Alexandrium blooms in the western Gulf of Maine: The plume advection hypothesis revisited. Limnol. Oceanogr. 50, 328–345. doi:10.4319/lo.2005.50.1.0328

Andreae, M.O., Byrd, J.T., Froelich Jr, P.N., 1983. Arsenic, antimony, germanium, and tin in the Tejo estuary, Portugal: Modeling a polluted estuary. Environ. Sci. Technol. 17, 731–737. doi:10.1021/es00118a008

Arantes e Oliveira, E., 1941. Esgotos de Lisboa – Estudos de Ante Projecto. Trabalho elaborado para a Câmara Municipal de Lisboa.

Araújo, I.B., Dias, J.M., Pugh, D.T., 2008. Model simulations of tidal changes in a coastal lagoon, the Ria de Aveiro (Portugal). Cont. Shelf Res. 28, 1010–1025. doi:10.1016/j.csr.2008.02.001

Baldaque da Silva, A., 1893. Estudo histórico-hidrográfico sobre a barra e o porto de Lisboa. Imprensa Nacional.

Barton, E.D., Aristegui, J., Tett, P., Canton, M., García-Braun, J., Hernández-León, S., Nykjaer, L., Almeida, C., Almunia, J., Ballesteros, S., Basterretxea, G., Escanez, J., García-Weill, L., Hernández-Guerra, a., López-Laatzen, F., Molina, R., Montero, M.F., Navarro-Peréz, E., Rodríguez, J.M., Van Lenning, K., Vélez, H., Wild, K., 1998. The transition zone of the Canary Current upwelling region. Prog. Oceanogr. 41, 455–504. doi:10.1016/S0079-6611(98)00023-8

Bonamano, S., Madonia, A., Borsellino, C., Stefanì, C., Caruso, G., De Pasquale, F., Piermattei, V., Zappalà, G., Marcelli, M., 2015. Modeling the dispersion of viable and total Escherichia coli cells in the artificial semi-enclosed bathing area of Santa Marinella (Latium, Italy). Mar. Pollut. Bull. doi:10.1016/j.marpolbul.2015.04.030

Bower, A.S., 2002. Structure of the Mediterranean Undercurrent and Mediterranean Water spreading around the southwestern Iberian Peninsula. J. Geophys. Res. doi:10.1029/2001JC001007

Briere, C., Giardino, A., Van der Werf, J., 2011. Morphological Modeling of Bar Dynamics With Delft3D: the Quest for Optimal Free Parameter Settings Using an Automatic Calibration Technique. Coast. Eng. Proc. doi:10.9753/icce.v32.sediment.60

Burke, A., Meignen, L., Bisson, M., Pimentel, N., Henriques, V., Andrade, C., Da Conceição Freitas, M., Kageyama, M., Fletcher, W., Parslow, C., Guiducci, D., 2011. The Palaeolithic occupation of southern Alentejo: the Sado River Drainage Survey. Trab. Prehist. 68, 25–49. doi:10.3989/tp.2011.11057

Caeiro, S., Martins, F., Costa, M.. H., Painho, M., Neves, R., 2001. Metodologia de Gestão Dinâmica do Estuário do sado. I Congr. sobre Planeam. e Gestão das Zo. Costeiras dos Países Expressão Port. 10.

Carballo, R., Iglesias, G., Castro, A., 2009. Residual circulation in the Ría de Muros (NW Spain): A 3D numerical model study. J. Mar. Syst. 75, 116–130. doi:10.1016/j.jmarsys.2008.08.004

Castiglioni, S., Lombardi, L., Toth, E., Castellarin, A., Montanari, A., 2010. Calibration of rainfall-runoff models in ungauged basins: A regional maximum likelihood approach. Adv. Water Resour. 33, 1235–1242. doi:10.1016/j.advwatres.2010.04.009

Chao, S.-Y., 1990. Tidal Modulation of Estuarine Plumes. J. Phys. Oceanogr. 20, 1115–1123. doi:10.1175/1520-0485(1990)020<1115:TMOEP>2.0.CO;2

Cherubin, L., Carton, X., Paillet, J., Morel, Y., Serpette, A., 2000. Instability of the Mediterranean Water undercurrents southwest of Portugal: Effects of baroclinicity and of topography. Oceanol. Acta 23, 551–573. doi:10.1016/S0399-1784(00)01105-1

Choi, B.-J., Wilkin, J.L., 2007. The Effect of Wind on the Dispersal of the Hudson River Plume. J. Phys. Oceanogr. 37, 1878–1897. doi:10.1175/JPO3081.1

Coelho, H.S., 2002. Modelação de Processos Físicos Relacionados com a Circulação Oceânica na Margem Continental Ibérica. Tese de Doutoramento em Engenharia do Ambiente, Universidade Técnica De Lisboa, Instituto Superior Técnico.

De Boer, W.F., Rydberg, L., Saide, V., 2000. Tides, tidal currents and their effects on the intertidal ecosystem of the southern bay, Inhaca Island, Mozambique. Hydrobiologia 428, 187–196. doi:10.1023/A:1004030605474

DeCastro, M., Gómez-Gesteira, M., Álvarez, I., Crespo, a. J.C., 2011. Atmospheric modes influence on Iberian Poleward Current variability. Cont. Shelf Res. 31, 425–432. doi:10.1016/j.csr.2010.03.004

Deltares, 2011a. Delft3D-Flow User Manual Version 3.15. Delft, The Netherlands.

Deltares, 2011b. Delft3D-RGFGRID. Generation and manipulation of curvilinear grids for Delft3D-FLOW and Delft3D-WAVE. User Manual.

Deltares, 2011c. Delft3D-QUICKIN. Generation and manipulation of grid-related param- eters such as bathymetry, initial conditions and rough- ness, User Manual.

Dias, J.M., Lopes, J.F., 2006. Implementation and assessment of hydrodynamic, salt and heat transport models: The case of Ria de Aveiro Lagoon (Portugal). Environ. Model. Softw. 21, 1–15. doi:10.1016/j.envsoft.2004.09.002

Dias, J.M., Lopes, J.F., Dekeyser, I., 2001. Lagrangian transport of particles in Ria de Aveiro lagoon, Portugal. Phys. Chem. Earth, Part B Hydrol. Ocean. Atmos. 26, 721–727. doi:10.1016/S1464-1909(01)00076-4

Dias, J.M., Sousa, M.C., Bertin, X., Fortunato, A.B., Oliveira, A., 2009. Numerical modeling of the impact of the Ancão Inlet relocation (Ria Formosa, Portugal). Environ. Model. Softw. 24, 711–725. doi:10.1016/j.envsoft.2008.10.017

Dias, J.M., Valentim, J.M., Sousa, M.C., 2013a. A numerical study of local variations in tidal regime of Tagus estuary, Portugal. PLoS One 8. doi:10.1371/journal.pone.0080450

Dias, J.M., Valentim, J.M., Sousa, M.C., 2013b. A Numerical Study of Local Variations in Tidal Regime of Tagus Estuary, Portugal. PLoS One 8, e80450. doi:10.1371/journal.pone.0080450

Duarte, B., Silva, G., Costa, J.L., Medeiros, J.P., Azeda, C., Sá, E., Metelo, I., Costa, M.J., Caçador, I., 2014. Heavy metal distribution and partitioning in the vicinity of the discharge

areas of Lisbon drainage basins (Tagus Estuary, Portugal). J. Sea Res. 93, 101–111. doi:10.1016/j.seares.2014.01.003

Egido, A., Egido, M., Seco, J., Garmendia, J., 2007. Quantitative relationships of mean seasonal precipitation in the Tagus river basin (SPain). Int. J. Climatol. 11, 205–212. doi:10.1002/joc.3370110207

Elhakeem, A., Elshorbagy, W., Bleninger, T., 2015. Long-term hydrodynamic modeling of the Arabian Gulf. Mar. Pollut. Bull. 94, 19–36. doi:10.1016/j.marpolbul.2015.03.020

Fiúza, A., DeMacedo, M., Guerreiro, M., 1982. Climatological space and time-variation of the Portuguese coastal upwelling. Oceanol. Acta 5, 31–40.

Flather, R. a, 1976. A tidal model of the northwest European continental shelf. Mem. la Soc. R. Sci. Liege 10, 141–164.

Fortunato, A.B., Baptista, A.M., Luettich, R.A., 1997. A three-dimensional model of tidal currents in the mouth of the Tagus estuary. Cont. Shelf Res. 17, 1689–1714. doi:10.1016/S0278-4343(97)00047-2

Fortunato, A.B., Oliveira, a., 2005. Influence of Intertidal Flats on Tidal Asymmetry. J. Coast. Res. doi:10.2112/03-0089.1

Fortunato, A.B., Oliveira, A., Baptista, A.M., 1999. On the effect of tidal flats on the hydrodynamics of the Tagus estuary. Oceanol. Acta 22, 31–44. doi:10.1016/S0399-1784(99)80030-9

Freire, P., Andrade, C., 2008. Caracterização das praias estuarinas do tejo. Actas do 8º Congr. da água 12.

Freire, P., Andrade, C., 1999. Wind-induced sand transport in Tagus estuarine beaches: First results. Aquat. Ecol. 33, 225–233. doi:10.1023/A:1009911012260

Frouin, R., Fiúza, A.F.G., Ambar, I., Boyd, T.J., 1990. Observations of a poleward surface current off the coasts of Portugal and Spain during winter. J. Geophys. Res. doi:10.1029/JC095iC01p00679

Fry, V. a., Aubrey, D.G., 1990. Tidal velocity asymmetries and bedload transport in shallow embayments. Estuar. Coast. Shelf Sci. 30, 453–473. doi:10.1016/0272-7714(90)90067-2

Fujiwara, T., Sanford, L.P., Nakatsuji, K., Sugiyama, Y., 1997. Anti-cyclonic circulation driven by the estuarine circulation in a gulf type ROFI. J. Mar. Syst. 12, 83–99. doi:10.1016/S0924-7963(96)00090-5

García Berdeal, I., 2002. Influence of wind stress and ambient flow on a high discharge river plume. J. Geophys. Res. 107, 1–24. doi:10.1029/2001JC000932

Garvine, R.W., 1984. Radial spreading of buoyant, surface plumes in coastal waters. J. Geophys. Res. doi:10.1029/JC089iC02p01989

Garvine, R.W., 1982. A steady state model for buoyant surface plume hydrodynamics in coastal waters. Tellus A 34, 293–306. doi:10.3402/tellusa.v34i3.10813

Godin, G., 1972. The Analysis of Tides. Toronto: University of Toronto Press. pp 264.

Govoni, J.J., Stender, B.W., Pashuk, O., 2000. Distribution of larval swordfish, Xiphias gladius, and probable spawning off the southeastern United States. Fish. Bull. 98, 64–74.

Gray, C. a., 1996. Intrusions of surface sewage plumes into continental shelf waters: Interactions with larval and presettlement juvenile fishes. Mar. Ecol. Prog. Ser. 139, 31–45. doi:10.3354/meps139031

Harcourt-Baldwin, J.-L., Diedericks, G.P.J., 2006. Numerical modelling and analysis of temperature controlled density currents in Tomales Bay, California. Estuar. Coast. Shelf Sci. 66, 417–428. doi:10.1016/j.ecss.2005.10.001

Horner-Devine, A.R., Jay, D. a., Orton, P.M., Spahn, E.Y., 2009. A conceptual model of the strongly tidal Columbia River plume. J. Mar. Syst. 78, 460–475. doi:10.1016/j.jmarsys.2008.11.025

Huthnance, J.M., Van Aken, H.M., White, M., Barton, E.D., Le Cann, B., Coelho, E.F., Alvarez Fanjul, E., Miller, P., Vitorino, J., 2002. Ocean margin exchange - Water flux estimates. J. Mar. Syst. 32, 107–137. doi:10.1016/S0924-7963(02)00034-9

Iglesias, I., Couvelard, X., Caldeira, R.M.A., 2014. Geostrophic influence in the River Douro plume : a climatological study, in: V Conferência Nacional de Mecânica Dos Fluidos, Termodinâmica E Energia. Porto, Portugal, pp. 11–12.

INAG/MARETEC/IST, 2002. Water Quality in Portuguese estuaries: Mondego, Tagus and Sado.

Instituto de Meteorologia, 2004. Caracterização Climática da Costa. Características do Clima da Costa de Portugal Continental.

Jouanneau, J.M., Garcia, C., Oliveira, A., Rodrigues, A., Dias, J.A., Weber, O., 1998. Dispersal and deposition of suspended sediment on the shelf off the Tagus and Sado estuaries, S.W. Portugal. Prog. Oceanogr. 42, 233–257. doi:10.1016/S0079-6611(98)00036-6

Kalnay, E., Kanamitsu, M., Kistler, R., Collins, W., Deaven, D., Gandin, L., Iredell, M., Saha, S., White, G., Woollen, J., Zhu, Y., Leetmaa, A., Reynolds, B., Chelliah, M., Ebisuzaki, W., Higgins, W., Janowiak, J., Mo, K.C., Ropelewski, C., Wang, J., Jenne, R., Joseph, D., 1996. The NCEP/NCAR 40-Year Reanalysis Project. Bull. Am. Meteorol. Soc. 77, 437–472.

Kolmogorov, A.N., 1942. Equations of Turbulent Motion of an Incompressible Fluid. Izv. Acad. Sci. USSR; Phys. 6, 56–58. doi:10.1007/978-94-011-3030-1_48

Kourafalou, V.H., 1999. Process studies on the Po River plume, North Adriatic Sea. J. Geophys. Res. doi:10.1029/1999JC900217

Lastras, G., Arzola, R.G., Masson, D.G., Wynn, R.B., Huvenne, V.A.I., Hühnerbach, V., Canals, M., 2009. Geomorphology and sedimentary features in the Central Portuguese submarine canyons, Western Iberian margin. Geomorphology 103, 310–329. doi:10.1016/j.geomorph.2008.06.013

Lencart e Silva, J.D., 2007. Controls on Exchange in a Subtropical Tidal Embayment, Maputo Bay. Ph.D. dissertation, University of Wales, Bangor.

Lencart e Silva, J.D., Simpson, J.H., Hoguane, A.M., Harcourt-Baldwin, J.-L., 2010. Buoyancy-stirring interactions in a subtropical embayment: a synthesis of measurements and model simulations in Maputo Bay, Mozambique. African J. Mar. Sci. 32, 95–107. doi:10.2989/18142321003714609

Lencart, J.D., Azevedo, A., Lillebø, A.I., Dias, J.M., 2013. Turbidity under changing physical forcing over two contrasting locations of seagrass meadows 2023–2028. doi:10.2112/SI65-342.1

Li, S., Meng, X., Ge, Z., Zhang, L., 2015. Evaluation of the threat from sea-level rise to the mangrove ecosystems in Tieshangang Bay, southern China. Ocean Coast. Manag. 109, 1–8. doi:10.1016/j.ocecoaman.2015.02.006

Li, Z., Chen, Q., Xu, Q., 2014. Modeling algae dynamics in Meiliang Bay of Taihu Lake and parameter sensitivity analysis. J. Hydro-environment Res. 9, 216–225. doi:10.1016/j.jher.2014.10.001

Macedo, M.E., 2006. Caracterização de Caudais - Rio Tejo. Technical Report, Direcção de Serviços de Monitorização Ambiental, Lisboa, CCDR-LVT.

MacMillan, D.S., Beckley, B.D., Fang, P., 2004. Monitoring the TOPEX and Jason - 1 microwave radiometers with GPS and VLBI wet zenith path delays. Mar. Geod. 27.

Markull, K., Lencart, J.D., Simpson, J.H., Dias, J.M., 2014. The influence of the Maputo and Incomati rivers on the mixing and outflow of freshwater from Maputo Bay (Mozambique) 580–585. doi:10.2112/SI70-098.1

Martins, C.S., 2002. Surface circulation in the eastern North Atlantic, from drifters and altimetry. J. Geophys. Res. doi:10.1029/2000JC000345

Martins, F., Leitão, P., Silva, A., Neves, R., 2001. 3D modelling in the Sado estuary using a new generic vertical discretization approach. Oceanol. Acta 24, 51–62. doi:10.1016/S0399-1784(01)00092-5

Martins, M., Calvão, T., Figueiredo, H., 1983. Estudo ambiental do estuário do Tagus, Estudo de Qualidade de Água. Resultados Referentes a observações sinópticas em 1982, CAN/Tagus 30-REL 27, Ministério da Qualidade de Vida, Lisboa, Portugal.

Mason, E., Coombs, S., Oliveira, P.B., 2010. An overview of the literature concerning the oceanography of the eastern North Atlantic region 51.

McCabe, R.M., MacCready, P., Hickey, B.M., 2009. Ebb-Tide Dynamics and Spreading of a Large River Plume*. J. Phys. Oceanogr. 39, 2839–2856. doi:10.1175/2009JPO4061.1

Monteiro, M.T., Guerra, M., Cavaco, M.H., Ferronha, H., Nogueira, M., Iniap, 2004. Caranterização Ambiental da Zona Costeira Adjacente aos Estuários do Tejo e Sado.

Neves, F.J., 2010. Dynamics and hydrology of the Tagus estuary: results from in situ observations. PhD Thesis, University of Lisbon, Portugal.

Neves, R. and, 1982. Caracterização hidrográfica do estuário do Sado, Tech. Report. Dep. Engenharia Mecânica, I.S.T.Universidade Técnica de Lisboa, Lisbon (1982).

Neves, R., Martins, F., 2004. Modelação Hidrodinamica e Ecológica no estuário do Sado, Universidade Nova de Lisboa.

Octavia, K.A.H., Jirka, G.H., Harleman, D.R.F., 1977. Vertical Heat Transport Mechanisms in Lakes and Reservoirs. Tech. Rep. 22, Massachusetts Institute of Technology.

Officer, C.B., 1976. Physical Oceanography of estuaries (and associated coastal waters). New York, Wiley.

Oliveira, I.B.M., 1992. Port of Lisbon: Improvement of the access conditions through the Tagus estuary entrance. Coast. Eng. 2745–2757.

Otero, P., Ruiz-Villarreal, M., Peliz, a., 2008. Variability of river plumes off Northwest Iberia in response to wind events. J. Mar. Syst. 72, 238–255. doi:10.1016/j.jmarsys.2007.05.016

Pawlowicz, R., Beardsley, B., Lentz, S., 2002. Classical tidal harmonic analysis including werror estimates in MATLAB using T_TIDE. Comput. Geosci. 28, 929–937. doi:10.1016/S0098-3004(02)00013-4

Peixoto, J.P., Oort, A.H., 1992. Physics of Climate. American Institute of Physics, New York.

Peliz, Á., Dubert, J., Santos, A.M.P., Oliveira, P.B., Le Cann, B., 2005. Winter upper ocean circulation in the Western Iberian Basin - Fronts, Eddies and Poleward Flows: An overview. Deep. Res. Part I Oceanogr. Res. Pap. doi:10.1016/j.dsr.2004.11.005

Peliz, Á., Rosa, T.L., Santos, A.M.P., Pissarra, J.L., 2002. Fronts, jets, and counter-flows in the Western Iberian upwelling system. J. Mar. Syst. 35, 61–77. doi:10.1016/S0924-7963(02)00076-3

Pérez, F.F., Castro, C.G., Álvarez–Salgado, X.A., Ríos, A.F., 2001. Coupling between the Iberian basin — scale circulation and the Portugal boundary current system: a chemical study. Deep Sea Res. Part I Oceanogr. Res. Pap. 48, 1519–1533. doi:10.1016/S0967-0637(00)00101-1

Picado, A., Dias, J.M., Fortunato, A.B., 2010. Tidal changes in estuarine systems induced by local geomorphologic modifications. Cont. Shelf Res. 30, 1854–1864. doi:10.1016/j.csr.2010.08.012

Portela, L.I., Neves, R., 1994. Numerical modelling of suspended sediment transport in tidal estuaries: A comparison between the Tagus (Portugal) and the Scheldt (Belgium-the Netherlands). Netherlands J. Aquat. Ecol. 28, 329–335. doi:10.1007/BF02334201

Prandtl, L., 1945. Über ein neues Formalsystem für die ausgebildete Turbulenz. Nachr. Akad. Wiss. Göttingen, Math.-Phys. Kl. 1945, 6–19. doi:10.1007/978-3-662-11836-8_72

Quintino, V., Elliott, M., Rodrigues, A.M., 2006. The derivation, performance and role of univariate and multivariate indicators of benthic change: Case studies at differing spatial scales. J. Exp. Mar. Bio. Ecol. 330, 368–382. doi:10.1016/j.jembe.2005.12.040

Ramos, A.M., Pires, A.C., Sousa, P.M., Trigo, R.M., 2013. The use of circulation weather types to predict upwelling activity along the western Iberian Peninsula coast. Cont. Shelf Res. 69, 38–51. doi:10.1016/j.csr.2013.08.019

Relvas, P., Barton, E.D., Dubert, J., Oliveira, P.B., Peliz, Á., da Silva, J.C.B., Santos, a. M.P., 2007. Physical oceanography of the western Iberia ecosystem: Latest views and challenges. Prog. Oceanogr. 74, 149–173. doi:10.1016/j.pocean.2007.04.021

Relvas, P., Luís, J., Santos, A.M.P., 2009. Importance of the mesoscale in the decadal changes observed in the northern Canary upwelling system. Geophys. Res. Lett. 36. doi:10.1029/2009GL040504

Robinson, A.R., 1987. Three-Dimensional Models of Marine and Estuarine Dynamics, Elsevier Oceanography Series, Elsevier Oceanography Series. Elsevier. doi:10.1016/S0422-9894(08)70443-4

Rodi, W., 1984. Turbulence models and their application in Hydraulics, State-of-the-art paper article sur l'etat de connaissance. IAHR Paper presented by the IAHR-Section on Fundamentals of Division II: Experimental and Mathematical Fluid Dynamics, The Netherlands.

Rodrigues da Silva, M.C., 2003. Instrumentos de Apoio à Gestão de Estuários. Indicadores Ambientais. Ph.D. thesis, Universidade Nova de Lisboa, Faculdade de Ciências e Tecnologia.

Romano, E., Del Bon, A., Petrangeli, A.B., Preziosi, E., 2013. Generating synthetic time series of springs discharge in relation to standardized precipitation indices. Case study in Central Italy. J. Hydrol. 507, 86–99. doi:10.1016/j.jhydrol.2013.10.020

Salgueiro, A.R., Machado, M.J., Barriendos, M., Pereira, H.G., Benito, G., 2013. Flood magnitudes in the Tagus River (Iberian Peninsula) and its stochastic relationship with daily North Atlantic Oscillation since mid-19th Century. J. Hydrol. 502, 191–201. doi:10.1016/j.jhydrol.2013.08.008

Santos, C., Catarino, J., Marques, E., Figueiredo, Z., Trancoso, A., Marecos, H., Neves, R., 2002. Monitoring sea water around the disposal area of Guia submarine outfall, 2nd International Conference on Marine waste water discharges. MWWD 2002- Istanbul, 1-12.

Serra, P.C., 2008. Densificação do Regime de caudais da Convenção sobre a Cooperação para a Protecção e o Aproveitamento Sustentávl das Águas das Bacias Hidrográficas Luso-Espanholas 17.

Shaw, E.M., 1983. Hydrology in Practice Van Nostrand Reinhold, Berkshire, UK.

Silva, S., Ré, A., Pestana, P., Rodrigues, A., Quintino, V., 2004. Sediment disturbance off the Tagus Estuary, Western Portugal: chronic contamination, sewage outfall operation and runoff events. Mar. Pollut. Bull. 49, 154–62. doi:10.1016/j.marpolbul.2004.02.004

Simpson, J.H., 1997. Physical processes in the ROFI regime. J. Mar. Syst. 12, 3–15. doi:10.1016/S0924-7963(96)00085-1

Skamarock, W.C., Klemp, J.B., Dudhia, J., Gill, D.O., Barker, D.M., Duda, M.G., Huang, X.-Y., Wang, W., Powers, J.G., 2008. A Description of the Advanced Research WRF Version 3. NCAR/TN–475+STR NCAR TECHNICAL NOTE.

Sobral, 1995. Estuário do Sado Observação de correntes de marés, Tech. Report. Instituto Hidrográfico, Lisbon (1977).

Sousa, M.C., Vaz, N., Alvarez, I., Gomez-Gesteira, M., Dias, J.M., 2014a. Influence of the minho river plume on the rias baixas (nw of the iberian peninsula). J. Mar. Syst. 139, 248–260. doi:10.1016/j.jmarsys.2014.06.012

Sousa, M.C., Vaz, N., Alvarez, I., Gomez-Gesteira, M., Dias, J.M., 2014b. Modeling the Minho River plume intrusion into the Rias Baixas (NW Iberian Peninsula). Cont. Shelf Res. 85, 30–41. doi:10.1016/j.csr.2014.06.004

Sousa-Dias, A., Melo, R.A., 2008. Long-term abundance patterns of macroalgae in relation to environmental variables in the Tagus Estuary (Portugal). Estuar. Coast. Shelf Sci. 76, 21–28. doi:10.1016/j.ecss.2007.05.039

Stelling, G.S., 1984. On the construction of computational methods for shallow water flow problems. Tech. Rep. 35, Rijkswaterstaat.

Stow, C.A., Jolliff, J., McGillicuddy, D.J., Doney, S.C., Allen, J.I., Friedrichs, M.A.M., Rose, K.A., Wallhead, P., 2009. Skill assessment for coupled biological/physical models of marine systems. J. Mar. Syst. 76, 4–15. doi:10.1016/j.jmarsys.2008.03.011

Tavares, A.O., Santos, P.P. dos, Freire, P., Fortunato, A.B., Rilo, A., Sá, L., 2015. Flooding hazard in the Tagus estuarine area: The challenge of scale in vulnerability assessments. Environ. Sci. Policy 51, 238–255. doi:10.1016/j.envsci.2015.04.010

UNESCO, 1981. Background papers and supporting data on the international equation of state 1980.

Vale, C., Sundby, B., 1987. Suspended sediment fluctuations in the Tagus estuary on semi-diurnal and fortnightly time scales. Estuar. Coast. Shelf Sci. 25, 495–508. doi:10.1016/0272-7714(87)90110-7

Valente, A.S., da Silva, J.C.B., 2009a. On the observability of the fortnightly cycle of the Tagus estuary turbid plume using MODIS ocean colour images. J. Mar. Syst. 75, 131–137. doi:10.1016/j.jmarsys.2008.08.008

Valente, A.S., da Silva, J.C.B., 2009b. On the observability of the fortnightly cycle of the Tagus estuary turbid plume using MODIS ocean colour images. J. Mar. Syst. 75, 131–137. doi:10.1016/j.jmarsys.2008.08.008

Valentim, J.M., Vaz, N., Silva, H., Duarte, B., Caçador, I., Dias, J.M., 2013. Tagus estuary and Ria de Aveiro salt marsh dynamics and the impact of sea level rise. Estuar. Coast. Shelf Sci. 130, 138–151. doi:10.1016/j.ecss.2013.04.005

Van Rijn, L.C., Walstra, D.-J.R., van Ormondt, M., 2007. Unified View of Sediment Transport by Currents and Waves. IV: Application of Morphodynamic Model. J. Hydraul. Eng. 133, 776–793. doi:10.1061/(ASCE)0733-9429(2007)133:7(776)

Vaz, N., Fernandes, L., Leitão, P.C., Dias, J.M., Neves, R., 2009. The Tagus estuarine plume induced by wind and river runoff: Winter 2007 case study. J. Coast. Res. Special Is, 1090–1094.

Vaz, N., Mateus, M., Plecha, S., Sousa, M.C., Leitão, P.C., Neves, R., Dias, J.M., 2015. Modeling SST and chlorophyll patterns in a coupled estuary-coastal system of Portugal: The Tagus case study. J. Mar. Syst. 147, 123–137. doi:10.1016/j.jmarsys.2014.05.022

Vieira, N., Mateus, M., Coelho, H., 2000. Temperature, Salinity and Geostrophic Currents Distributions in the Iberian Atlantic Margin. In 3rd Symposium on the Iberian Atlantic Continental Margin, Faro, Portugal 151–152.

Vis, G.-J., Kasse, C., Kroon, D., Jung, S., Zuur, H., Prick, A., 2010. Late Holocene sedimentary changes in floodplain and shelf environments of the Tagus River (Portugal). Proc. Geol. Assoc. 121, 203–217. doi:10.1016/j.pgeola.2009.12.003

Walker, N.D., 1996. Satellite assessment of Mississippi River plume variability: Causes and predictability. Remote Sens. Environ. 58, 21–35. doi:10.1016/0034-4257(95)00259-6

Willmott, C.J., 1981. On the validation of models. Phys. Geogr. 2, 184–194.

Wollast, 1979. Rio Sado, campagne de mesures d'avril1979 Tech. Report. Secretaria de estado do ambiente, Lisbon (1979).

Wollast, 1978. Rio Sado, campagne de mesures de juillet1978 Tech. Report. Secretaria de estado do ambiente, Lisbon (1978).

Wooster, W. S., Bakun, A., McLain, D.R., 1976. Seasonal upwelling cycle along eastern boundary of North Atlantic. J. Mar. Syst. 34, 131–141.

Yankovsky, A.E., Chapman, D.C., 1997. A Simple Theory for the Fate of Buoyant Coastal Discharges*. J. Phys. Oceanogr. 27, 1386–1401. doi:10.1175/1520-0485(1997)027<1386:ASTFTF>2.0.CO;2

Appendix

Appendix A: Tagus River Basin. Annual flow records at the stream gauging stations (http://snirh.pt/snirh/_relacoesint/convencao/dados/cvle_nota_tecnica.pdf)

ANOS	Out	Nov	Dez	Jan	Fev	Mar	Abr	Mai	Jun	Jul	Ago	Set
1940/41	111,0	167,8	174,3	354,2	431,7	502,2	566,9	630,6	658,1	671,6	679,1	687,3
1941/42	1,3	122,0	128,7	162,6	192,6	290,2	370,5	386,1	413,8	414,0	434,8	478,4
1942/43	91,3	133,1	209,1	260,1	297,5	379,9	488,6	500,2	507,5	528,9	535,9	592,8
1943/44	41,8	52,2	96,9	96,9	117,6	127,9	**194,6**	**223,9**	**254,7**	**258,9**	**275,2**	**335,8**
1944/45	**76,3**	**108,9**	**137,1**	**162,4**	**164,3**	**185,7**	**205,0**	**222,6**	**270,8**	**271,2**	**274,3**	**274,8**
1945/46	**21,9**	**110,4**	**205,5**	223,9	242,8	291,5	382,0	472,0	481,5	481,7	482,2	491,3
1946/47	15,4	38,5	54,0	83,7	244,2	392,0	421,8	469,2	489,2	516,6	542,4	577,7
1947/48	53,2	79,3	109,7	195,9	243,6	263,9	327,2	403,6	405,7	406,8	413,8	420,1
1948/49	32,9	33,7	82,6	96,7	99,7	146,7	**168,1**	**209,9**	**236,2**	**264,3**	**279,9**	**370,8**
1949/50	**12,1**	**77,0**	**120,6**	**133,5**	**171,3**	**200,5**	**204,1**	**250,1**	**274,3**	**283,5**	**289,0**	**304,9**
1950/51	**43,3**	**63,5**	**140,1**	**203,4**	**275,7**	352,3	411,9	436,6	469,9	472,7	478,3	526,7
1951/52	30,2	187,5	208,9	250,0	264,4	348,0	393,0	471,6	480,7	499,7	518,3	540,4
1952/53	31,8	63,6	98,4	108,8	127,0	153,6	**223,6**	**236,9**	**253,7**	**260,4**	**260,9**	**291,5**
1953/54	**70,5**	**87,7**	**149,3**	**157,0**	**165,8**	**228,1**	**250,6**	**292,4**	**305,5**	**306,1**	**307,2**	**307,2**
1954/55	**0,9**	**82,6**	**100,6**	**210,5**	305,0	320,7	342,1	385,4	396,9	402,0	443,2	446,6
1955/56	63,8	129,9	243,6	318,5	371,4	460,0	515,8	557,8	577,7	584,6	594,0	623,9
1956/57	46,6	60,2	86,0	95,7	141,6	177,4	**213,4**	**255,5**	**290,6**	**290,6**	**290,7**	**315,0**
1957/58	**69,5**	**94,8**	**123,0**	**167,8**	**190,7**	**259,9**	**285,2**	**310,5**	**348,3**	**350,1**	**356,0**	**367,7**
1958/59	**19,4**	**23,1**	**205,3**	252,3	275,7	336,3	369,5	446,8	463,0	478,7	516,9	600,0
1959/60	63,8	114,7	172,2	255,9	333,0	389,9	405,7	468,6	503,2	506,2	513,9	527,7
1960/61	155,5	212,4	271,6	294,9	296,6	311,0	372,9	444,1	459,7	467,6	474,5	522,9
1961/62	32,5	150,8	210,7	252,8	288,6	380,8	436,6	474,2	505,9	505,9	505,9	545,4
1962/63	57,5	89,4	141,2	258,0	341,0	371,8	455,6	466,0	521,0	536,8	536,8	579,0
1963/64	24,8	201,8	318,4	329,2	462,9	514,8	529,4	544,0	595,7	603,9	603,9	625,4
1964/65	5,1	28,5	72,1	118,4	167,9	246,3	252,9	263,2	274,5	276,0	278,7	337,3
1965/66	121,5	197,7	252,6	338,4	438,3	441,6	546,6	565,7	614,9	618,3	621,4	641,8
1966/67	107,5	172,3	179,1	218,1	282,7	304,4	347,7	387,9	415,2	415,2	422,4	429,9
1967/68	50,9	143,1	146,6	147,1	255,7	304,8	352,1	369,6	378,3	378,9	395,7	412,0
1968/69	21,0	86,4	122,9	174,5	263,6	380,6	428,6	472,3	503,3	514,4	519,0	578,1
1969/70	60,8	136,1	160,0	336,6	349,2	363,1	365,2	407,2	446,3	453,4	458,5	459,1
1970/71	2,7	41,2	54,6	129,1	136,5	192,7	266,5	360,6	408,4	415,4	430,2	436,2
1971/72	13,5	20,7	71,6	153,0	253,6	313,0	320,8	339,0	352,4	365,3	366,2	464,4
1972/73	157,8	213,2	286,3	327,6	330,0	352,4	361,9	445,8	492,8	503,6	504,9	506,0
1973/74	27,1	73,1	139,3	173,1	204,7	251,7	288,0	304,6	357,3	366,1	366,7	366,7
1974/75	5,6	54,7	70,6	100,8	142,8	221,7	282,0	339,3	352,8	352,8	360,5	392,8
1975/76	12,4	57,1	116,9	126,8	176,1	192,9	271,7	297,9	325,3	347,6	384,4	454,2
1976/77	68,0	121,2	246,0	319,0	385,4	396,0	411,4	452,3	486,5	500,0	521,5	534,8
1977/78	65,1	150,9	278,2	303,6	399,6	452,6	515,4	572,9	618,5	618,5	618,5	625,1
1978/79	34,4	83,0	240,4	349,7	447,0	492,8	558,9	567,6	589,7	611,2	611,7	627,5
1979/80	139,7	150,7	169,7	194,3	228,1	293,1	329,6	385,9	401,2	401,8	413,2	417,7
1980/81	35,2	78,9	79,7	80,9	109,6	152,9	**246,3**	**279,5**	**285,4**	**294,7**	**305,2**	**329,7**
1981/82	**9,6**	**10,7**	**179,6**	214,2	251,7	271,8	289,1	331,9	347,8	364,4	373,4	414,3
1982/83	19,3	106,6	120,1	120,3	152,7	152,8	**225,6**	**256,0**	**259,3**	**261,3**	**281,9**	**294,2**
1983/84	**42,3**	**204,9**	**263,1**	290,2	315,4	388,3	436,7	515,8	570,8	573,9	579,0	583,1
1984/85	50,9	199,9	221,8	355,8	418,9	423,6	463,4	521,4	547,3	551,3	551,3	554,5
1985/86	0,3	70,6	150,9	175,2	246,3	263,3	309,0	319,0	319,5	338,0	346,2	413,9
1986/87	68,5	93,5	116,3	212,5	260,7	275,9	353,9	387,6	398,9	433,2	446,4	488,7
1987/88	51,1	132,5	251,3	330,6	350,6	354,2	437,1	492,7	569,6	588,7	588,7	588,7
1988/89	67,0	124,6	124,8	139,1	160,1	182,3	**230,5**	**310,2**	**317,9**	**328,8**	**331,5**	**359,4**
1989/90	**18,3**	**187,7**	**399,4**	440,7	444,8	463,5	536,1	552,4	553,9	559,9	564,1	594,7
1990/91	89,3	150,3	170,4	205,1	278,6	343,4	367,7	370,3	381,9	391,5	392,0	413,4
1991/92	67,1	82,0	137,6	152,0	175,3	191,4	239,7	292,2	336,0	345,2	375,7	387,9
1992/93	76,3	84,7	125,0	129,6	155,1	178,1	**227,4**	**299,5**	**337,8**	**344,2**	**347,1**	**366,8**
Média	48,2	106,2	161,1	210,2	260,9	309,5	356,6	398,1	424,1	432,2	441,7	470,1
60% Méd.	28,9	63,7	96,6	126,1	156,5	**185,7**	213,9	238,9	254,5	259,3	265,0	282,1
70% Méd.	33,7	69,0	104,7	136,6	169,6	**201,2**	231,8	258,8	275,7	281,0	287,1	329,1

Appendix B: Sado River Basin. Annual flow records at the stream gauging stations (http://www.peer.eu/about_peer/euraqua_collaboration/network_of_hydrological_observatories/)

	Name (code)	Fllor de Rosa (23I/01H)	Herdade de Pancas (22G/02H)	**Moinho da Gamitinha (25G/03H)**	Moinho do Bravo (25G/02H)	**Monte da Rocha (Rio) (27H/02H)**	Odivelas (Rio) (24I/01H)	Ponte Alvalade Campilhas (26G/04H)	**Ponte Alvalade Sado (26G/05H)**	Ponte Pomar (22G/01H)	Ponte São Domingos (26F/02H)	Ponte Vale Joana (25G/04H)	São Domingos (Algalé) (24H/01H)	Torrão do Alentejo (24H/03H)	Vale da Ursa (24H/02H)
General features	Latitude (º N)	38.361	38.532	**38.063**	38.061	**37.736**	38.173	37.932	**37.941**	38.579	37.933	38.122	38.296	38.299	38.306
	Longitude (º N)	-8.068	-8.458	**-8.404**	-8.411	**-8.296**	-8.138	-8.404	**-8.383**	-8.492	-8.542	-8.434	-8.316	-8.229	-8.291
	M (m)	205704	171697.4	**176260.78**	175616.5	**185627.929**	199547.8	176185.3	**178027.985**	168740.1	164023.6	173627.5	184026.2	191592	186197.2
	P (m)	154828.3	173872.2	**121790.779**	121607.4	**85468.541**	134031.3	107291	**108272.31**	179150.9	107465.5	128434.7	147720.4	148030.8	148834.2
	River	Rib. Xarrama	Rib. S. Martinho	**Rio Sado**	Rib. Corona	**Rio Sado**	Rib. Odivelas	Rib. Campilhas	**Rio Sado**	Rib. Marateca	Rib. S. Domingos	Rib. Gândola	Rib. Algalé	Rib. Xarrama	Rib. Ursa
	Drainage area	328.04	59.03	**2713.16**	219.83	**246.84**	440.56	698.32	**669.75**	134.87	144.44	197.12	61.79	468.35	76.35
Annual flow (dm^3)	1934 / 35	8872	-	**17547**	7286	-	8602	-	-	-	-	-	1288	-	5065
	1935 / 36	163991	-	**400197**	71763	-	137462	-	-	-	-	-	17234	-	28714
	1936 / 37	83648	-	**321787**	49217	-	73554	-	-	-	-	-	8198	-	15197
	1937 / 38	67567	-	**249212**	43353	-	69920	-	-	-	-	-	8295	-	14607
	1938 / 39	60131	-	**162082**	28766	-	58718	-	-	-	-	-	6019	-	10454
	1939 / 40	125174	-	**511035**	62657	-	139409	-	-	-	-	-	14375	-	21981
	1940 / 41	136333	-	**424458**	51742	-	128559	-	-	-	-	-	11930	-	24644
	1941 / 42	28769	-	**147043**	24209	-	24715	-	-	-	-	-	5395	-	11362
	1942 / 43	144225	-	**377360**	55053	-	100708	-	-	-	-	-	18218	-	26024
	1943 / 44	1021	-	**16426**	1585	-	1646	-	-	-	-	-	296	-	0
	1944 / 45	12113	-	**9287**	1196	-	8800	-	-	-	-	-	127	-	27
	1945 / 46	51826	-	**298778**	34301	-	44129	-	-	-	-	-	6422	-	12749
	1946 / 47	133566	-	**781708**	72117	-	211785	-	-	-	-	-	15667	-	28502
	1947 / 48	67565	-	**252729**	40451	-	116508	-	-	-	-	-	8117	-	14439
	1948 / 49	1879	-	**79666**	7469	-	7273	-	-	-	-	-	464	-	1042
	1949 / 50	21428	-	**234266**	26126	-	30239	-	-	-	-	-	2895	-	11221
	1950 / 51	59731	-	**219076**	40384	-	69780	-	-	-	-	-	6675	-	17225
	1951 / 52	84527	-	**367062**	55774	-	104210	-	-	-	-	-	12511	-	23218
	1952 / 53	18040	-	**85073**	9948	-	9959	-	-	-	-	-	1720	-	8686
	1953 / 54	17615	-	**181913**	26886	-	27230	-	-	-	-	-	4387	-	11969
	1954 / 55	98045	-	**304936**	26817	-	103352	-	-	-	-	-	13469	-	27403
	1955 / 56	175416	-	**570854**	78583	-	177575	-	-	-	-	-	14831	-	31843
	1956 / 57	8640	-	**39548**	3810	-	8222	-	-	-	-	-	2073	-	6178
	1957 / 58	12469	-	**48302**	17934	-	8105	-	-	-	-	-	3335	-	13720
	1958 / 59	107043	-	**542833**	72295	-	87589	-	-	-	-	-	10080	-	32546
	1959 / 60	123265	-	**468183**	-	-	116462	-	-	-	-	-	-	-	45745
	1960 / 61	58149	-	**184397**	-	**14495**	94851	-	-	-	-	-	-	-	18148
	1961 / 62	76952	-	**299134**	-	**50612**	69244	-	-	-	-	-	-	83772	23262
	1962 / 63	135390	-	**842307**	-	**82452**	167442	-	-	-	-	-	-	189181	39266
	1963 / 64	128280	-	**622587**	-	**71787**	134597	-	-	-	-	-	-	134183	36099
	1964 / 65	13872	-	**66561**	-	**4553**	24883	-	-	-	-	-	-	24738	8770
	1965 / 66	133724	-	-	-	**54844**	147858	-	-	-	-	-	-	151441	37538
	1966 / 67	-	-	**83753**	-	**6515**	21684	-	-	-	-	-	-	24800	4206
	1967 / 68	-	-	**128938**	-	**27110**	46214	-	-	-	-	-	-	48898	8921
	1968 / 69	-	-	**836014**	-	-	149792	-	-	-	-	-	-	164105	-
	1969 / 70	-	-	-	-	-	103984	-	-	-	-	-	-	117247	-
	1970 / 71	-	-	**103195**	-	-	-	-	-	-	-	-	-	24713	-
	1971 / 72	-	-	**144903**	-	-	-	-	-	-	-	-	-	50031	-
	1972 / 73	-	-	-	-	-	-	-	-	-	-	-	-	31296	-
	1973 / 74	-	-	-	-	-	-	-	-	-	-	-	-	12816	-
	1974 / 75	-	-	**55745**	-	-	-	-	-	-	-	-	-	16534	-
	1975 / 76	-	-	**40789**	-	-	-	-	-	-	-	-	-	1863	-
	1976 / 77	-	-	-	85977	-	-	-	-	-	-	-	-	125979	-
	1977 / 78	-	-	**307251**	69244	-	-	-	-	-	-	-	-	119051	-
	1978 / 79	-	-	-	80793	-	-	-	-	-	-	-	-	145484	-
	1979 / 80	-	-	-	8162	-	-	-	-	-	-	-	-	27631	-
	1980 / 81	-	-	**39007**	1835	-	-	10456	**19108**	-	2660	-	-	4924	-
	1981 / 82	-	4897	**95744**	21730	-	-	-	**33737**	12811	67740	-	-	46733	-
	1982 / 83	-	908	**10180**	1496	-	-	6403	**4931**	1587	2359	-	-	1557	-
	1983 / 84	-	9743	**200078**	48081	-	-	59066	**45516**	22625	27963	-	-	52672	-
	1984 / 85	-	21174	**331151**	68468	-	-	113293	**76291**	43956	42482	62022	-	108350	-
	1985 / 86	-	7806	**127312**	25958	-	-	55328	**33017**	19846	14997	29034	-	47126	-
	1986 / 87	-	8415	**122452**	20209	-	-	47990	**31078**	17293	15227	-	-	32241	-
	1987 / 88	-	12391	**307840**	58799	-	-	110225	**66647**	25757	51766	-	-	78567	-
	1988 / 89	-	1243	**117646**	10075	-	-	33163	**41204**	3378	14030	14510	-	5717	-
	1989 / 90	-	22354	-	81902	-	-	-	**175902**	49599	-	72597	-	123806	-
	1990/ 91	-	-	-	-	-	-	101851	-	-	-	-	-	-	-
	1991/ 92	-	-	**33622**	-	-	-	589	**6402**	-	-	-	-	1519	-
	1992/ 93	-	-	-	-	-	-	-	-	-	-	-	-	-	-
	1993/ 94	-	-	-	-	-	-	-	**13301**	-	-	-	-	42520	-
	1994/ 95	-	-	-	-	-	-	-	**3265**	-	-	-	-	-	-
	1995/ 96	-	-	-	-	-	-	-	-	-	-	-	-	-	-
	1996/ 97	-	-	-	-	-	-	-	-	-	-	-	-	69816	-
	1997/ 98	-	-	-	-	-	-	-	-	-	-	-	-	-	-
	1998/ 99	-	-	-	-	-	-	-	**2203**	-	-	-	-	3536	-
	1999 / 0	-	-	-	-	-	-	-	**10251**	-	-	-	-	22118	-
	2000/ 1	-	-	-	-	-	-	-	-	-	-	-	-	-	-
	2001/ 2	-	-	-	-	-	-	-	-	-	-	-	-	-	-
	2002/ 3	-	-	-	-	-	-	-	-	-	-	32021	-	-	-
	2003/ 4	-	-	**128401**	-	-	-	-	-	29600	24325	7156	-	23073	-
	2004/ 5	-	-	-	-	-	-	0	**0**	1752	41	8905	-	3474	-
	2005/ 6	-	-	-	-	-	-	5368	**2**	-	17869	9696	-	30428	-
	2006/ 7	-	-	**298606**	-	-	-	-	-	-	-	-	-	86778	-
	2007/ 8	-	-	-	-	-	-	-	-	-	-	-	-	10471	-
	2008/ 9	-	-	-	-	-	-	-	-	-	-	-	-	21589	-